THE ROLE OF ARCHITECTURE AND TISSUE PROPERTIES IN THE STRUCTURAL INTEGRITY OF HUMAN VERTEBRAL CANCELLOUS BONE

A Dissertation
Presented to the Faculty of the Graduate School
of Cornell University
In Partial Fulfillment of the Requirements for the Degree of
Doctor of Philosophy

by
Jacqueline Heather Cole
May 2007

THE ROLE OF ARCHITECTURE AND TISSUE PROPERTIES IN THE STRUCTURAL INTEGRITY OF HUMAN VERTEBRAL CANCELLOUS BONE

Jacqueline Heather Cole, Ph.D.

Cornell University 2007

Age-related disorders of bone metabolism like osteoporosis may compromise structural integrity of bone and result in fragility fractures, particularly at cancellous bone sites. Several factors contribute to cancellous bone strength, including bone density, architecture, and material properties. Clinical assessment of bone density using dual-energy X-ray absorptiometry (DXA), which is somewhat distorted by the fan-shaped X-ray beam, does not fully account for fracture incidence and only partially correlates with bone strength. Spatial variations in trabecular architecture captured by micro-computed tomography (microCT) have been related to structural behavior using microstructure-based models. However, the impact of material variations is not well understood and should be investigated.

DXA fan-beam magnification was quantified by scanning aluminum rods at several distances above the X-ray source. Projected area and bone mineral content decreased by 1.6-1.8% per centimeter distance above the source, indicating that changes in girth over time would artificially reduce DXA measurements and obscure actual gains associated with growth or interventions.

The ability of DXA to predict bone architecture and material properties was assessed in thoracolumbar specimens from 21 cadavers. T11-L4 was scanned using DXA, and cancellous bone cores drilled from the center of T12 and L2 were scanned at 17 μm using microCT and then compressed uniaxially to failure. DXA and microCT bone mass correlated similarly with cancellous bone stiffness and strength in females but not males. DXA could not account for variations in architecture detected by microCT, particularly in the thoracic spine, for either males or females. MicroCT scans may better assess bone strength in the thoracic spine and could replace DXA scans altogether if measurements could be made non-invasively, accurately, and affordably.

Spatial variations in architecture and material properties were examined with architecture- and material-based finite element (FE) models developed from microCT scans. Homogeneous and heterogeneous material models were examined. FE models were improved by heterogeneity, whether between subjects using specimen-specific uniform properties or within subjects using spatially varying properties. Apparent stiffness was the same for specimen-specific models, regardless of variations in tissue modulus. The mean tissue modulus, rather than its distribution, appears to drive the overall mechanical behavior for vertebral cancellous bone.

BIOGRAPHICAL SKETCH

Jacqueline Cole was born in Sheffield, Alabama, in 1978 and grew up in Muscle Shoals, Alabama. She graduated with honors as valedictorian of Muscle Shoals High School in May 1996. She attended Auburn University on a presidential academic scholarship and graduated *summa cum laude* with a Bachelor of Mechanical Engineering degree in May 2001. While at Auburn University, Jacqueline participated on the Baja SAE and Formula SAE teams, which are student design projects sponsored by the Society of Automotive Engineers (SAE), and it was here that she developed a love for mechanics and engineering design. These experiences, along with a desire to help better the lives of people through scholarly research, led her to pursue graduate study in Mechanical Engineering with an emphasis on Biomechanics and with minors in Biomedical Engineering and Biometry. Jacqueline completed a Master of Science in August 2004 and a Ph.D. in May 2007 at Cornell University.

I dedicate this work
to my family (Daddy, Moma, Jonathan, Uta, Ange, Zach, and Granny),
to my Ithaca family (Sami, Catherine, Jad, Rami, Pépé, and Gammy)
and especially to Naji

ACKNOWLEDGMENTS

As with any project of this magnitude, many people have contributed in a variety of ways. I am grateful for all of the invaluable assistance I received with this work. I will attempt to name everyone, but please forgive any oversights.

First, I would like to thank Marjolein van der Meulen, my Committee Chair, for her support, guidance, and patience throughout my graduate tenure. Her knowledge and expertise in the field are impressive and have given me something for which to strive, but I most admire her enthusiasm for her work and the work of her students. Her vision for my research and for my success have been inspirational.

I would like to thank Elizabeth Myers, my mentor at the Hospital for Special Surgery (HSS). Her ideas for this work and her commitment to my education, whether in biomechanics, statistics, or the ethical conduct of research, have been invaluable. I consider myself lucky to have had the guidance of two successful female scientists.

I thank my other committee members, Donald Bartel and Martin Wells. I am indebted to their time, support, ideas, and technical expertise throughout this work.

I thank Kenneth Mann, Professor and Director of the Musculoskeletal Sciences Research Center in the Department of Orthopedic Surgery at SUNY Upstate Medical University, for providing me with cadaver spines and graciously allowing me to use his laboratory facilities. I also thank Joseph Lane, Chief of Metabolic Bone Disease Service at HSS, and Tamara Scerpella, Associate Professor of Orthopedic Surgery at SUNY Upstate Medical University, for use of their clinical bone density scanners.

Special thanks go to Elizabeth Gillen, who helped with the architecture analysis of this project for her senior honors thesis, and to Tim Morgan, who patiently

answered a lot of questions about architecture analysis and whose MATLAB code I used extensively.

Preparing and testing the cadaver specimens was time and labor intensive, and I depended on the help of many people, including Tunde Babalola, Jayme Burket, Dan Chen, Sean Daugherty, Naji Husseini, Maureen Lynch, and Kate Meyers. Thanks to them all for their time and extra hands!

I would like to thank the administrative staff at Cornell and HSS, Judy Thoroughman and Martha Bacchus, for their help with ordering specimens and equipment and dealing with all of the financial headaches of research. Judy especially was a lifesaver with completing all of the necessary paperwork, and I could not have submitted this work without her efforts. I also thank Rose Mary Fisher and Sylvia Hom at the Osteoporosis Prevention Center for their assistance.

I owe thanks to the biomechanics students and staff for their input and support throughout my time at Cornell, especially Ben Bourne, Eve Donnelly, Chris Fritton, Kirk Gunsallus, Garry Hayeck, Jason Long, Kevin Ong, Jeremy Rawlinson, Veronica Santos, and Madhu Venkadesan. Also, thanks to my officemates in Upson 130 for providing necessary reprieves from the daily stresses of graduate life, especially Todd Humphreys, Isaac Miller, Shan Mohiuddin, Mike Moorehead, Mike Sherback, and Jeff Sullivan.

Throughout my time at Cornell, I competed on the sport taekwondo team, and it helped me to stay in shape, provided a continual outlet for frustrations in the lab and in life, and it kept me sane. Many people helped make this experience a memorable one: Sabumnim Cho, Naji Husseini, Tim Gera, Evan Hopkins, Katie Conlon, Dan Dickens, Brian Block, Jenn Burg, Dave Biermann, Regina Clewlow, and Debbie Mahoney.

I would like to thank the many wonderful people in the Ithaca Church of Christ for giving me a family away from home and providing me with spiritual companionship and guidance. God bless!

Last, but certainly not least, I would like to thank my family for their love and encouragement throughout my life and for always believing in me and challenging me to reach for the stars. I also thank the Husa and Husseini families for taking me in as a part of their family and giving me a place to call home in Ithaca. They have been my biggest fans and supporters, and I am forever grateful for their love, generosity, and tasty home-cooked meals!

My funding sources made all of this work possible. I acknowledge the National Institutes of Health, which provided support through a predoctoral training grant (T32-AR007281), a shared instrumentation grant (S10-RR014801), a core center grant (P30-AR046121), and a research facilities improvement grant (C06-RR12538-01). In addition, I acknowledge the American Association for University Women Educational Foundation for a Selected Professions Fellowship.

TABLE OF CONTENTS

LIST OF FIGURES

LIST OF TABLES

CHAPTER 1

INTRODUCTION

Background and Significance

Throughout life, the human skeleton performs critical biomechanical and metabolic functions. The physiology and structure of bone provides support for the body, facilitates locomotion, protects the internal organs, and serves as a reservoir for essential minerals in the body, especially calcium. Bone also houses red bone marrow, where the cellular components of blood are produced. Bone tissue is organized into two different structures. Cortical bone is comprised of densely-packed osteons and is found primarily in the shafts of long bones and in the outer shell of vertebrae. Cancellous bone consists of a less dense structure of bone struts called trabeculae and is located primarily in the ends of long bones and in vertebral bodies. Bone can be studied on a variety of length scales, ranging from the whole bone level (1 cm – 1 m), down to the trabecular structure (1 mm – 1 cm), the lamellar tissue of individual trabeculae (1 μm – 1 mm), and the composite of collagen fibers and mineral crystals found at the ultrastructure level (1 nm – 1 μm). Bone is a living tissue that adapts to its mechanical environment. However, disruptions in bone metabolism due to disease, trauma, or other pathologies can compromise structural integrity and the ability of bone to bear loads. Skeletal disorders result in fracture when the intrinsic strength of the bone structure drops below the level required to withstand applied loads either during normal activity or higher-energy trauma events, such as falls [88].

Age-related bone loss is complex and multifactorial, influenced by genetic factors (e.g., growth factors and bone morphogenic proteins), systemic regulatory hormones (e.g., parathyroid hormone and calcitonin), and the mechanical environment (e.g., loads and displacements). Bone is metabolically active and can regenerate itself by forming new tissue at sites of older or damaged tissue by a process called remodeling. The normal remodeling process couples periods of bone resorption and bone formation, thereby maintaining adequate bone tissue to support skeletal functions. However, the remodeling process may become unbalanced with aging, and increased resorption may produce irreversible perforation, thinning, and overall loss of bone tissue. The remodeling process occurs at bone surfaces and, therefore, preferentially affects the open structure of cancellous bone more than the denser cortical bone due to the larger surface to volume ratio in the former. In fact, remodeling affects approximately 20% of trabecular bone surfaces at any given time [97].

Age-related bone degradation can seriously compromise bone integrity. For both men and women, bone mass decreases with age [1,3,28,65,70,139], but especially in women due to peri-menopausal bone loss. By age 80, women lose approximately 20% of their bone mineral density (BMD) in the lumbar spine, thereby increasing the likelihood for developing osteoporosis [49,114,115]. Osteoporosis is a skeletal condition marked by reduced bone mass and a deteriorated microarchitecture, which reduces bone strength and increases the likelihood of fracture [90,134]. In 2002, over 10 million Americans had osteoporosis and another 34 million had osteopenia or low bone mass; of these individuals, approximately 80% were women [90]. By 2010, the prevalence of osteoporosis and osteopenia are expected to increase by 20%, making the population more susceptible to fragility fractures [90]. Osteoporosis-related fractures, which threaten a patient’s quality of life, result in increased morbidity and mortality and impart extensive healthcare costs [31,52,75]. As the life expectancy of the general population continues to increase, age-related declines will result in even lower bone mass, and the total incidence of skeletal fractures will rise, unless diagnosis and treatment of skeletal deficiencies can be significantly improved [74,90].

Early assessment of fracture risk is, therefore, crucial to prevent and treat excessive bone loss from conditions such as osteoporosis [109-111]. Osteoporosis is one of the most serious public health concerns today, especially among the aging population. Each year, Americans experience approximately 1.5 million osteoporotic fractures, nearly half of which occur in the spine [16,110,134]. At 50 years of age, white women have a 40% lifetime risk, and white men have a 13% lifetime risk, of sustaining an osteoporotic fracture at the spine, hip, or forearm [25,76]. Osteoporosis is often asymptomatic prior to fracture, thus making it difficult to predict and possibly prevent with anabolic therapies. Therefore, the accurate evaluation of bone strength using surrogate measures from routine assessment tools is essential, as is understanding the determinants of bone mechanical behavior. However, surrogate measures must be validated with experimental mechanical properties assessed in the laboratory.

Laboratory Measurement of Bone Mechanical Properties

Bone structural competence, the target prediction of surrogate imaging techniques and computer modeling, is measured by mechanical testing. The mechanical behavior of cancellous bone can be described by apparent properties measured at the continuum level or by tissue properties measured for a single trabecula. At least five characteristic lengths are generally required to justify the continuum assumption for cancellous bone [42], which equates to a minimum sample size of approximately 5-10 mm. Cancellous bone is highly anisotropic and heterogeneous, and its response to mechanical loads depends on many factors, such as the species, anatomic site, and age of the subject, which are manifested in the volume fraction (or apparent density), architecture, and tissue material properties of the bone sample (Figure 1.1). For example, the mean apparent elastic modulus of human cancellous bone tested in compression varied between 67 MPa in the lumbar spine to 489 MPa in the proximal tibia, and the compressive ultimate stress (strength) varied between 1.4 MPa in the lumbar spine and 7.4 MPa in the femur [61,62,68,71,85,91, 112,113,143]. Similarly, the compressive ultimate strain varied greatly even within a single site, ranging between 1.5% and 7.4% in the human lumbar spine [61,85].

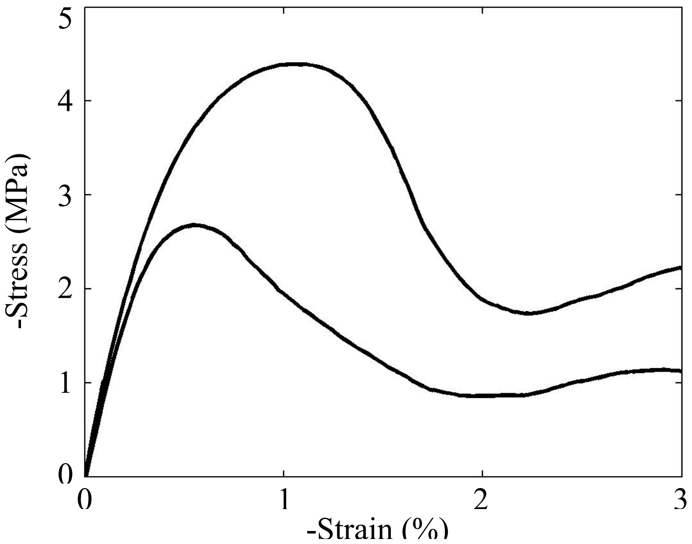

Figure 1.1. Sample stress-strain curves for cylindrical samples of human vertebral cancellous bone of two subjects with different bone volume fractions (top curve = 20%, bottom curve = 14%). The samples were monotonically tested to failure in compression. Both subjects had normal bone mass as assessed by a clinical bone density scan.

The preceding experimental data were all obtained for a loading orientation corresponding to the primary *in vivo* axis at each site (e.g., along the superior-inferior axis for the lumbar spine and proximal tibia and along the femoral neck axis for the proximal femur). Given the anisotropic nature of cancellous bone, the apparent properties would differ for other loading orientations. For the lumbar spine, the compressive strength along the longitudinal bone axis (defined above) was measured as 2.1-3.4 times larger than that along the transverse axis, depending on the age of the subject [87].

Cancellous bone strength has also been described as asymmetric, with different values for compressive and tensile loading, although this supposition has not been conclusively proven. In early studies of bovine cancellous bone, the compressive strength was, on average, 1.6 to 3 times greater than the tensile strength, independent of the apparent density [56,124]. However, studies in human cancellous bone first revealed that compressive and tensile strengths were similar [13,108] and then that the tensile strength was greater [112]. A more recent study of bovine cancellous bone taken from the proximal femur revealed that the asymmetry between compressive and tensile strengths was a function of the apparent modulus [60]. The data from this study indicated that the cancellous bone became proportionally stronger in compression than in tension with increasing modulus, and this variable strength asymmetry has also been demonstrated for human vertebral bone [61].

Traditionally, apparent-level mechanical properties were assessed by applying loads directly to the cancellous bone surface. However, this technique produces experimental artifacts due to friction at the bone-platen interface and damage at the bone surface from machining. Friction at the interface induces an uneven stress distribution near the bone surface [140], which may overestimate the apparent modulus by about 5%, as determined by FE models [11,96]. Excising a bone sample from the surrounding tissue disrupts the trabecular network, which may make the trabeculae near the surface unstable. Trabecular instability at the surface will increase the on-axis strain in this region and will underestimate the apparent modulus by 20-40% [59,96].

Changing the boundary conditions can significantly alter the mechanical behavior of the bone sample. Embedding the ends of the bone sample in a thin layer of bone cement increased the apparent modulus by 20%, while lubricating the platens with a thin film of low viscous oil reduced the modulus by 7% [67]. A new testing technique was devised to minimize the experimental artifacts by gluing the ends of cancellous bone specimens into brass end caps and introducing elastic preconditioning cycles before final loads were applied [58]. This procedure eliminated the initial nonlinear region of the stress-strain curve and is now widely accepted as the standard for mechanical testing of cancellous bone. However, gluing the ends of the trabecular cores into brass caps introduces complex boundary conditions between the bone and end caps that are not well understood and not easily modeled.

Heterogeneity in Bone Tissue Material Properties

Similar to apparent properties, bone tissue properties are evaluated by mechanically testing an individual trabecula or small specimens extracted from within a trabecula. Even in normal individuals, bone tissue mineral content and quality (e.g., degree of mineralization and mineral crystal size and maturity) show substantial variation both spatially [9,72,94] and temporally [40,41] for a given site and species.

Techniques used to examine tissue properties include microbeam testing, nanoindentation, and spectroscopic compositional characterization. From microbeam testing, the trabecular tissue modulus was measured as 18.6 GPa using tension tests, as 20.7 GPa using ultrasonic methods [105], and as 3.8-4.6 GPa using three-point bending tests [15,62]. The mean tissue modulus assessed by nanoindentation ranged

7-26 GPa, depending on location within the tissue and type of lamellar tissue sampled, and individual measurements varied 17-62% [106,107,131,145]. This variation in modulus was true across individuals and for multiple anatomic sites. Even within a single trabecula, indentation modulus ranged 8-16 GPa [107]. In a microspectroscopic analysis of human osteonal bone, the mineral crystal size and perfection and the degree of mineralization as assessed by the mineral:matrix ratio increased from the younger tissue at the osteon center to the older tissue at the osteon periphery [101]. Similarly, in normal trabecular bone, mineral crystallinity and maturity increased with bone age, as measured by distance from the trabecular surface, so that the most recently deposited mineral was less mineralized, less crystalline, and less perfect crystals [100]. In studies of older patients, osteoporosis altered the bone tissue material properties, as generally evidenced by reduced mineral content and larger, more mature mineral crystals in both cortical [38,77,99] and trabecular bone [32,100]. Such changes in tissue properties are expected to compromise the structural performance of bone, although the effect of bone tissue composition and distribution on mechanical properties is not well understood, particularly for cancellous bone.

Tissue properties are difficult to characterize, because the experimental techniques currently available only examine a small volume of bone that likely does not fully capture the spatial variations in mineral content and quality. Therefore, computer models that can mimic the *in vivo* tissue mineral gradients may allow us to analyze a larger volume of bone material and improve the assessment of cancellous tissue properties. Overall, measurements of tissue material properties indicate that the tissue-level modulus of cancellous bone can vary substantially, and this variability may be at least partially explained by differences in mineralization, material disruptions due to bone remodeling, and various ultrastructure alterations (e.g., collagen maturity, orientation, and cross-linking) [73]. The biomechanical effects of gradients in bone tissue modulus, as well as the relative effects of reduced bone mass and altered architecture, need to be examined.

The structural behavior of cancellous bone is governed chiefly by bone mass or bone density, microarchitecture (the geometric and spatial distribution and connectivity of trabeculae), and tissue material properties [12,34,73,104,129]. Alterations in any of these components could compromise the integrity of the bone structure and its ability to bear loads. Although most *in vivo* imaging tools measure bone mass or apparent density (bone mass per total volume), these measures alone do not fully explain variations in mechanical properties observed experimentally. In the following sections, the contribution of bone mass, architecture, and material properties to the structural behavior of cancellous bone will be described, as well as the clinical and laboratory tools used to characterize them.

Clinical Bone Imaging and Osteoporosis Assessment

Bone mass is most commonly assessed *in vivo* using dual-energy X-ray absorptiometry (DXA), which evaluates the inorganic mineral phase of bone with minimal radiation exposure to patients. DXA scans can be performed for large regions, such as the lumbar spine, proximal femur, forearm, or even the whole body, thereby providing a non-invasive global measure of bone mass. However, DXA scans are two-dimensional and can only provide projected areal measurements of bone mineral density. In addition, the resolution with this technique is relatively low (on the order of 1 mm) and cannot capture architectural features of cancellous bone (on the order of 0.1 mm) or mineral distributions within the trabecular tissue. Because unmineralized tissues do not inherently attenuate X rays, DXA scans also cannot evaluate the organic phase of bone or soft tissues surrounding bone.

Direct outcomes from DXA, measured in a particular bone region of interest, include projected bone area and bone mineral content (BMC). Areal bone mineral density (aBMD) is a two-dimensional metric derived from the direct measures and is calculated as the ratio of BMC to projected area. T-score is a statistical measure relating a patient's aBMD to the peak aBMD of a sex- and race-matched population of normal young individuals, and is computed as follows:

$$\text{T-score} = \frac{\text{aBMD(patient)} - \text{aBMD(young normal population)}}{\text{SD(young normal population)}}$$

where SD = standard deviation. The World Health Organization (WHO) divided T-score into three diagnostic categories to characterize bone mass status [55]. Patients with aBMD within one standard deviation below the young population mean (T-score > -1.0) are considered normal. Patients with a T-score between -1.0 and -2.5 are labeled with osteopenia or low bone mass. Patients with a T-score less than or equal to -2.5 are diagnosed with osteoporosis.

Most clinical DXA scanners use a fan-shaped X-ray beam to evaluate bone geometry and mineral measures. This beam geometry produces a wide incidence and thus can scan large bone areas quickly in a single pass, because it eliminates the need to scan in a raster pattern required for column-shaped beams. The fan-beam measurements vary depending on the location of the bone region within the X-ray beam [4,8,18,37,102,119,127,128], making accurate comparisons between subjects of different girths, or within growing subjects over time, difficult. Complications of this sort are compounded during the adolescent years, when growth-related increases in limb and trunk girths artificially decrease DXA measurements of bone area and BMC by amounts similar to increases in these measurements from exercise or drug treatments [18]. In such cases, erroneously magnified fan-beam measurements may obscure true bone accrual and thus the effect of a particular intervention. Quantifying and correcting magnification errors in fan-beam scanners is essential to identify bone mineral accrual with DXA correctly.

Areal BMD from DXA correlates variably with bone mechanical properties, explaining 20-70% of the variability in vertebral failure load *in vitro* and *in situ* [7,14,69,82,89]. For cancellous bone specimens taken from the human proximal femur, aBMD explained only 10-40% of the variation in apparent elastic modulus and 50-70% of the variation in ultimate stress [17]. For the human proximal tibia, BMC measured from photon absorptiometry (a precursor to DXA) explained 50-60% of the variation in apparent modulus and ultimate stress and only 5% of the variation in ultimate strain [66].

In addition, DXA aBMD and its T-score do not fully explain the incidence of osteoporotic fractures. More than half of fragility fractures occur in women with a T-score in the normal range [78,118,122]. Patients with a low T-score who were treated with antiresorptive drugs experienced only modest increases of 0-8% in aBMD that could not account for the accompanied 15-60% drop in vertebral fracture occurrence [21-24,117]. In fact, regression models from these experiments predicted only 4% and 16% of the reduction in fracture risk for raloxifene and alendronate therapy, respectively [24,117]. Therefore, DXA aBMD and T-score alone do not sufficiently evaluate the risk of fracture, at least for changes in bone density associated with antiresorptive drugs. Clinically, our ability to measure additional parameters that may correlate with fracture risk is limited. However, laboratory methods allow us to examine the relative role of bone mass, architecture, and material properties.

Laboratory Characterization of Bone Mass and Microarchitecture

Three-dimensional measurements of cancellous bone mass and structure may provide additional information to improve fracture prediction. Cancellous bone mass is typically measured by either bone volume fraction (BV/TV), which is the volume of bone tissue present within the total volume of interest, or by apparent bone mineral density (appBMD), which is the amount of bone tissue present within the total volume. Additionally, tissue bone mineral density (tisBMD), which is the amount of bone tissue within only the bone volume, can be computed as the product of BV/TV and appBMD. Apparent bone density has been used to predict bone strength and apparent modulus using empirical formulations [12,33,47,105,108]. Regardless of the relationship used, apparent BMD and BV/TV obtained experimentally or from micro-computed tomography (microCT) explained 60-85% of the variability in compressive elastic modulus and ultimate stress for human cancellous bone [59,61,66,68,80]. Because cancellous bone ash fraction impacts bone strength and modulus more than volume fraction [44], appBMD and BV/TV may relate to bone mechanical properties differently.

Cancellous microarchitecture also plays a key role in the structural competence of bone. As early as the mid-19th century, increased fracture incidence was observed in older patients with thinning bone [19]. Therefore, characterizing the cancellous bone structure is important for understanding the relationship between architecture and mechanical properties. Similar to bone mass measures, architecture parameters have also been experimentally correlated with elastic mechanical properties [20,35,36,53, 95,136]. Independent of apparent density, bone regions with different architectures exhibited variable elastic mechanical properties that differed by over 50% [132]. Based on studies using two-dimensional serial sectioning techniques, trabecular orientation and connectivity correlated with cancellous bone strength [36,103,129]. In sheep femoral bone assessed with microCT, architecture indices explained 10-70% of the variation in compressive ultimate strength [79]. A static histomorphometry study indicated that some of the architecture-strength correlations also hold true in human vertebral bone [126].

Early assessments of cancellous bone morphology were based on two-dimensional microscopy sections and modeled the structure as a set of parallel plates, but this approach was based on underlying geometric assumptions [98]. The parallel-plate model had two degrees of freedom, the plate thickness and separation, which were held constant throughout the model. Basic stereological parameters were computed from estimates of the bone volume and surface area. Parameters included trabecular thickness (Tb.Th), defined as the mean plate thickness, trabecular separation (Tb.Sp), defined as the mean plate separation, and trabecular number (Tb.N), defined as the mean plate density. The plate model did not accurately capture the complex structure of cancellous bone, which is composed of both trabecular rods and plates distributed non-uniformly throughout the volume [26,45] Other variations on the plate model were also tried, but the accuracy of all two-dimensional techniques were highly dependent on the validity of the geometric model and its assumptions.

Due to recent improvements in high-resolution tomographic imaging, cancellous bone architecture can now be characterized in three dimensions and with fewer assumptions than with two-dimensional techniques [30,116]. MicroCT provides a quantitative assessment of cancellous bone architecture and tissue mineral density for small *ex vivo* samples (on the order of 40 mm x 40 mm x 40 mm) (Figure 1.2). Because microCT involves a relatively large radiation dose, scans are not suitable for *in vivo* clinical use and require the invasive retrieval of a bone biopsy. The resolution for microCT is much higher than for DXA, allowing measurements down to 0.010 mm for small bone samples and therefore provides a detailed three-dimensional spatial mapping of cancellous bone architecture and mineralization.

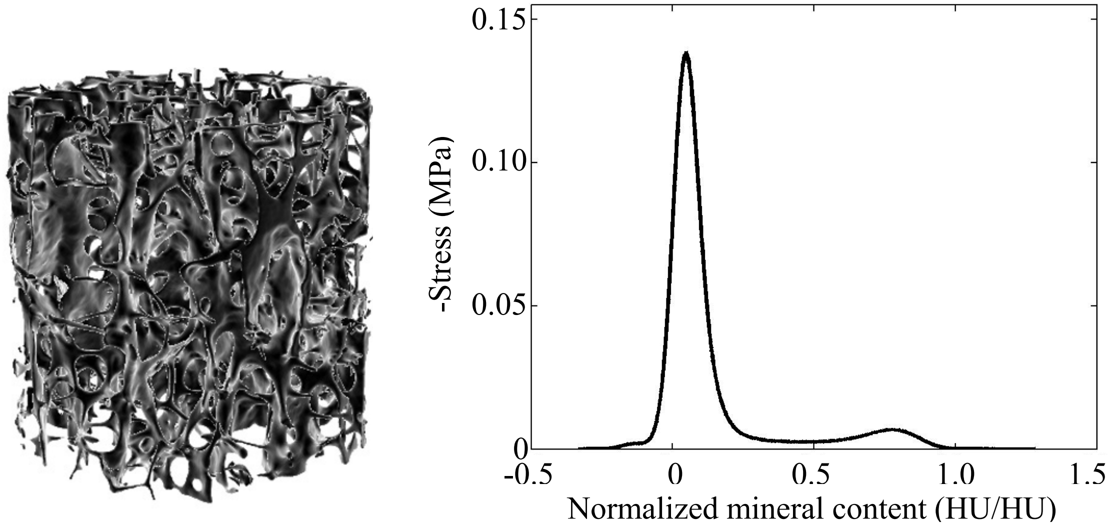

(a) (b)

Figure 1.2. (a) Volume of human vertebral cancellous bone (∅8.25 mm x 8 mm) scanned with micro-computed tomography (microCT) and reconstructed at an isotropic voxel resolution of 17 μm. (b) Frequency histogram of X-ray attenuation (measured in Hounsfield Units = HU) across all voxels of the microCT scan, which can be converted to tissue mineral density.

Three-dimensional methods for characterizing bone morphology eliminate the need for an assumed model structure and directly measure architecture parameters from reconstructed image data [46]. Direct measurement of trabecular thickness (Tb.Th*) is computed by fitting maximum-sized spheres to the bone structure. For each bone voxel, the local Tb.Th* is computed as the Euclidian distance to the nearest non-bone voxel, which is equivalent to finding the radius of a sphere centered on the bone voxel and enlarged to fill the trabecular structure without extending past the structure boundary. Applying this distance transformation to all bone voxels creates a distance map of the distribution of local thicknesses. Similarly, the distribution of direct trabecular separation (Tb.Sp*) is calculated by fitting maximum-sized spheres centered on non-bone voxels to the marrow space.

Cancellous bone is anisotropic, and the overall material behavior is governed by the trabecular geometry and orientation. Specifically, apparent density and trabecular orientations can be analytically related to cancellous bone stiffness [20] and experimentally explain 72-94% of the variability in the elastic constants [130]. Trabecular anisotropy is characterized by the mean intercept length (MIL), which is a measure of the mean distance between adjacent trabecular surfaces computed for various directions [43,133,142]. By counting the number of intersections between bone-marrow interfaces and a superimposed test grid of parallel lines with a particular orientation, the MIL for that orientation of the trabecular structure is calculated from the ratio of the total line length of the grid to the number of intersections. To compute the overall three-dimensional MIL, the test grid is rotated through a number of random orientations in all three dimensions, and the planar MIL is computed for each. These planar MILs are plotted in a three-dimensional polar plot, and the points are fit to an ellipsoid, which can be expressed as a second-rank fabric tensor. The eigenvectors of the fabric tensor represent the principal directions of the trabecular structure, and the eigenvalues represent the principal three-dimensional MILs. In addition, the anisotropy ratio is computed as the ratio of the largest to smallest principal MIL. A minimum of 200 random orientations of a test grid with a maximum spacing of 0.2 mm was deemed necessary to accurately assess the MIL [121].

As mentioned previously, both apparent and tissue properties contribute to the mechanical performance of cancellous bone. Just as the apparent-level material behavior of cancellous bone is governed by the mass and microarchitecture of trabeculae, the tissue material behavior is determined by the mineral content and arrangement of ultrastructure constituents. The collective role of bone mass, architecture, and tissue mineral properties (or variations in any of the three) in cancellous bone structural behavior cannot be fully examined using currently available imaging or testing techniques. In particular, the biomechanical effects of gradients in bone tissue modulus need to be examined.

Simulation of Bone Structure and Material Properties

Computer models can non-invasively and non-destructively simulate variations in material properties and investigate their effect on apparent and tissue-level mechanical behavior, allowing insight into the biomechanical effects of age-related bone degradation and treatments. Early analytical models employed a simple cellular solid analysis to study the relationship between apparent modulus (or strength) and appBMD or BV/TV [33], although the analysis could also be extended to quantitative architecture measures or tissue material properties. The basic premise was that the mechanical behavior of a large group of periodically-spaced unit cells with identical morphology would sufficiently describe the apparent-level behavior of the overall structure. Therefore, the behavior of only one unit cell needed to be analyzed for a given cell geometry, loading direction, and failure mode (e.g., elastic buckling, brittle fracture, or plastic yielding) [57]. However, such simplistic models, which inherently require geometric assumptions, do not capture the true architecture of cancellous bone and thus cannot assess the effect of geometric and material heterogeneity.

Idealized finite element (FE) models also used the cellular solid paradigm and its inherent geometric assumptions but incorporated an irregular lattice-type structure to better mimic the complex *in vivo* geometry of cancellous bone [5,39,51,120,144]. With lattice models, the effect of changes in the cancellous bone architecture is assessed by removing or uniformly thinning trabecular elements and observing the resulting changes in mechanical behavior. Changes in tissue material properties have not been evaluated with these models. Because each trabecula is modeled as a single element, lattice-type FE models cannot capture local gradients in tissue material properties or even minute details in trabecular architecture.

MicroCT scans can accurately capture both architecture [30] and mineral content throughout an entire cancellous bone sample. Therefore, microCT-based FE models, which are generated by converting each voxel into a cubic finite element, can be used to couple the geometry of the bone structure and the material properties of the bone tissue. Voxel-based models more closely mimic the true bone structure and reduce the need for geometric and material assumptions (Figure 1.3). To date, they have primarily been used to examine the contribution of microarchitecture to the structural behavior of cancellous bone, and most have assumed isotropic and homogeneous material properties [48,53,132,136,137].

Voxel-based FE models also provide an opportunity to probe the effects of bone tissue heterogeneity on cancellous bone structural behavior. Initial modeling studies did not incorporate measured tissue modulus distributions but either used the mean tissue modulus value [48,54,63,92,93,132,138] or assumed a particular spatial distribution [50,135]. Modeling non-uniform mineral distributions that varied as a function of depth from the trabecular surface altered apparent modulus by as much as 20% [135]. In addition, independent of trabecular architecture, increasing the coefficient of variation in tissue modulus from 0 to 50% and also varying the spatial distributions of modulus resulted in a 2.5-24% lower structure apparent modulus [50]. For a given architecture and bone volume fraction, architecture-based FE models with heterogeneous tissue properties predicted lower apparent moduli than models with homogeneous properties. One limitation to incorporating bone tissue heterogeneity in models is the lack of data available to simulate the material gradients accurately.

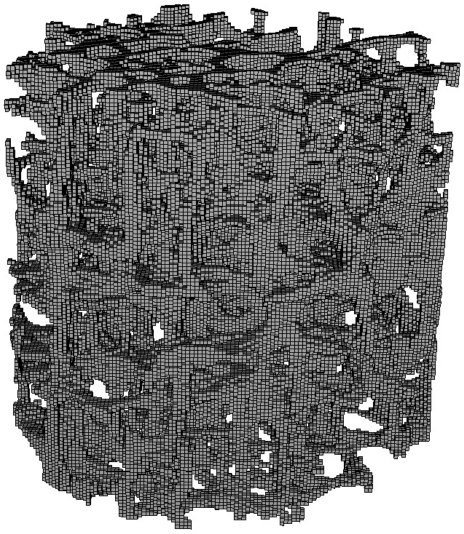

Figure 1.3. Finite-element mesh of human vertebral cancellous bone, generated by converting each voxel from a micro-computed tomography scan to an 8-noded linear brick element.

Understanding the effect of bone tissue heterogeneity is necessary for accurate prediction of the mechanical performance of cancellous bone, but more representative property variations are needed. Recently, systematic variations in tissue mineral density were observed from quantitative microCT scans of rabbit cancellous bone cubes, where tissue at the trabecular surface was less mineralized than tissue in the center of trabeculae [81]. Expressed as a percentage of the CT attenuation for cortical bone, the CT attenuation (and, consequently, mineral content) of the cancellous cubes decreased from 83% at the center of trabeculae to 68% at the trabecular surfaces. Interestingly, the mean CT attenuation was about 80% of the cortical bone attenuation. Architecture-based FE models using CT-derived tissue modulus distributions more accurately predicted mechanical behavior than models using a homogeneous modulus [10]. Specifically, FE models with a homogeneous tissue modulus only explained 75% of the variation in experimental apparent modulus, while adding material heterogeneity increased this explanatory power up to 88%. Therefore, models that do not capture this marked reduction in tissue mineral content with proximity to the trabecular surface may not capture the actual extent of heterogeneity present in cancellous bone tissue.

Age and Sex Effects

Given the relatively higher incidence of fragility fractures in women, understanding the sex-related differences in bone mass, architecture, and material properties with aging is critical for improved diagnosis and treatment of osteoporosis. For both sexes, volume fraction in human cancellous bone declined steadily throughout life [2,27,84,125], as did ash density [86,87]. However, histomorphometry studies hinted that sex had minimal or no impact on this relationship [2,6,29,84,125, 141]. Although ash density and volume fraction may change similarly with age for both sexes, the mechanisms of bone loss seem to be different and are at least partially related to the sex-specific changes in the cancellous architecture. Regardless of sex, mean trabecular thickness as measured with traditional histomorphometry techniques decreased with age for vertebral bone [27,45,84,125]. For men, decreased bone volume resulted more from progressive thinning of trabeculae while maintaining the trabecular network, but for women, it resulted mainly from a loss of trabeculae (and consequently an increase in trabecular separation) while maintaining the thickness of the remaining trabeculae [2]. Nevertheless, trabecular separation appears to increase with age for both sexes, primarily through the loss of trabeculae [6,83,84,123,125].

Sex-specificity in the changes of cancellous bone mechanical properties with age has not been clearly established. In one study, the compressive ultimate strength of cancellous bone samples from human spines decreased with age, although the confounding contributions of sex and varying ash density were not assessed [141]. Another study showed a clear degradation in bone mechanical properties with age independent of ash density. Even after normalizing by ash density, apparent modulus, ultimate stress, and energy absorption to failure decreased significantly with age in human vertebrae [87].

Understanding the capacity of bone imaging techniques to predict fragility fracture depends vitally on understanding how the various bone metrics correlate with each other and especially with mechanical properties. In addition, given that sex differences exist between age-related changes in bone mass, disparately resulting in more fractures in women, similar trends should also be found in bone architecture, tissue mineral composition and distribution, and/or apparent material properties. Normal spatial variability in the tissue properties of cancellous bone has been observed using various experimental techniques. Although bone tissue composition and distribution are altered with osteoporosis [64,99], the effect of such variations on structural behavior is not well understood, particularly with respect to sex and degree of osteoporotic bone degradation.

Study Objectives and Approaches

Successful diagnosis and treatment of osteoporosis depends critically on understanding the mechanics of cancellous bone and the determinants of fragility fracture. The load-bearing function of cancellous bone depends on several factors, including bone mass or density, microarchitecture, and tissue material quality. While bone mass and density are routinely assessed using a clinical DXA scan, these measures only account for 10-70% of the variability in stiffness and strength and are somewhat distorted from the fan-beam shape of the X-ray beam. In addition, more than half of fragility fractures occur in women with a normal DXA T-score.

Because DXA scans do not directly assess trabecular architecture or tissue material properties, other diagnostic tools may be needed. High-resolution microCT scans precisely characterize both trabecular architecture and tissue mineral distribution, which is related to spatial material variations. The impact of architectural variations on cancellous bone structural behavior has been examined using microstructure-based models developed from high-resolution imaging. However, the contribution of spatial variations in material properties is not well understood and needs to be investigated. Therefore, the objectives of this study were 1) to quantify bone mineral measurement errors associated with DXA fan-beam magnification; 2) to examine the ability of DXA to predict bone mineral and microarchitecture measures from microCT and bone material properties from structural testing; and 3) to investigate the effect of bone tissue heterogeneity on the mechanical performance of cancellous bone using finite element models.

For the first objective, DXA fan-beam magnification was examined by scanning aluminum rods of different shapes (square, rectangular, solid round, and hollow round) at four distances above the X-ray source in two orientations, with rods aligned parallel and perpendicular to the longitudinal axis of the scanning table [18]. Projected area, BMC, and areal BMD were assessed for each scan, and the variation of each of these parameters with distance from the X-ray source was computed. Our published results showed that for round rods, which most closely mimic the geometry of long bones, projected area and BMC decreased 1.6-1.8% per centimeter increase in distance from the X-ray source. The resulting 7% variation in projected area and BMC and 2% variation in areal BMD could be problematic in clinical studies using DXA scans. Any increases in girth over time would increase a bone's distance from the fan-beam source, artificially reduce area and BMC measurements, and therefore obscure any legitimate gains associated with the study intervention. Understanding and quantifying the degree of the fan-beam error is the necessary first step to correcting the DXA data.

For the second objective, human cadaver lumber spine segments were scanned using clinical DXA to determine areal BMD and T-score. Cancellous bone cores were machined from the center of the T12 and L2 vertebrae, and architecture and mineral composition and distribution were assessed using microCT. Following microCT, the ends of the cores were glued into brass caps, and the samples were monotonically compressed to failure to compute the apparent material properties. Measures from DXA and microCT were compared to those from mechanical testing to determine the ability of clinical and laboratory bone characterization techniques to predict bone strength and thus the likelihood of fragility fracture. The effect of sex on these comparisons was also examined. DXA and microCT mass measurements were similarly well-correlated with apparent modulus and strength in females but not in males. However, DXA could not account for variations in architecture found by microCT, particularly by tissue BMD in the thoracic spine. Therefore, microCT scans may be a superior alternative for assessing bone strength in the thoracic spine of both males and females and could replace DXA scans altogether if measurements could be made non-invasively, accurately, and affordably.

Finally, for the third objective, architecture- and material-based FE models were developed to investigate the ability of material heterogeneity to improve predictions of the mechanical behavior of human vertebral cancellous bone. Homogeneous and various heterogeneous material models were examined. We showed that FE models were improved by some degree of heterogeneity, whether across subjects to account for interspecimen variability or within subjects to account for intraspecimen variability. Compared to uniform homogeneous models, heterogeneous and specimen-specific homogeneous models increased the explanatory power for apparent modulus by 13% (increased r^2 from 0.29 to 0.42) and improved the predicted values by 217% (increased slope from 0.36 to 0.78). Apparent tissue stiffness was the same for heterogeneous and specimen-specific homogeneous models, which had tissue moduli that were mean-matched for each subject. Therefore, the mean tissue modulus, rather than its distribution, appears to drive the overall mechanical behavior for vertebral cancellous bone. Heterogeneous and specimen-specific homogeneous models both provide conservative estimates of apparent stiffness and may be useful for predicting mechanical behavior in the aging population.

References

1. (None) (1996) Bone density reference data. In: Favus MJ, Ed. Primer on the Metabolic Bone Diseases and Disorders of Mineral Metabolism. Lippincott Williams & Wilkins: Philadelphia. pp. 483.
2. Aaron JE, Makins NB, and Sagreiya K (1987) The microanatomy of trabecular bone loss in normal aging men and women. *Clin Orthop Relat Res* (215):260-71.
3. Barden H (1997) Bone mineral density of the spine and femur in normal U.S. white females. *J Bone Miner Res* 12(Suppl. 1):S248.
4. Barden HS, Settergren D, McClintock C, and Turner CH (2001) Measurement of Femur Geometry (HAL) with PRODIGY Is Accurate and Unaffected by Magnification. *J Bone Miner Res* 16(Suppl 1):S345.
5. Beaupré GS and Hayes WC (1985) Finite element analysis of a three-dimensional open-celled model for trabecular bone. *J Biomech Eng* 107(3):249-56.
6. Bergot C, Laval-Jeantet AM, Preteux F, and Meunier A (1988) Measurement of anisotropic vertebral trabecular bone loss during aging by quantitative image analysis. *Calcif Tissue Int* 43(3):143-9.
7. Bjarnason K, Hassager C, Svendsen OL, Stang H, and Christiansen C (1996) Anteroposterior and lateral spinal DXA for the assessment of vertebral body strength: comparison with hip and forearm measurement. *Osteoporos Int* 6(1):37-42.
8. Blake GM, Parker JC, Buxton FM, and Fogelman I (1993) Dual X-ray absorptiometry: a comparison between fan beam and pencil beam scans. *Br J Radiol* 66(790):902-6.

9. Bonucci E, Ballanti P, Della Rocca C, Milani S, Lo Cascio V, and Imbimbo B (1990) Technical variability of bone histomorphometric measurements. *Bone Miner* 11(2):177-86.
10. Bourne BC and van der Meulen MC (2004) Finite element models predict cancellous apparent modulus when tissue modulus is scaled from specimen CT-attenuation. *J Biomech* 37(5):613-21.
11. Brown TD and Ferguson AB, Jr. (1980) Mechanical property distributions in the cancellous bone of the human proximal femur. *Acta Orthop Scand* 51(3):429-37.
12. Carter DR and Hayes WC (1977) The compressive behavior of bone as a two-phase porous structure. *J Bone Joint Surg Am* 59-A:954-962.
13. Carter DR, Schwab GH, and Spengler DM (1980) Tensile fracture of cancellous bone. *Acta Orthop Scand* 51(5):733-41.
14. Cheng XG, Nicholson PH, Boonen S, Lowet G, Brys P, Aerssens J, van der Perre G, and Dequeker J (1997) Prediction of vertebral strength in vitro by spinal bone densitometry and calcaneal ultrasound. *J Bone Miner Res* 12(10):1721-8.
15. Choi K, Kuhn JL, Ciarelli MJ, and Goldstein SA (1990) The elastic moduli of human subchondral, trabecular, and cortical bone tissue and the size-dependency of cortical bone modulus. *J Biomech* 23(11):1103-13.
16. Chrischilles EA, Butler CD, Davis CS, and Wallace RB (1991) A model of lifetime osteoporosis impact. *Arch Intern Med* 151(10):2026-32.
17. Cody DD, McCubbrey DA, Divine GW, Gross GJ, and Goldstein SA (1996) Predictive value of proximal femoral bone densitometry in determining local orthogonal material properties. *J Biomech* 29(6):753-61.
18. Cole JH, Scerpella TA, and van der Meulen MC (2005) Fan-beam densitometry of the growing skeleton: are we measuring what we think we are? *J Clin Densitom* 8(1):57-64.

19. Cooper A. A treatise on dislocations and fractures of the joints. London: Longman, Hurst, Rees, Orme, and Brown, 1842.

20. Cowin SC (1985) The relationship between the elasticity tensor and the fabric tensor. *Mechanics of Materials* 4:137-147.

21. Cranney A, Tugwell P, Adachi J, Weaver B, Zytaruk N, Papaioannou A, Robinson V, Shea B, Wells G, and Guyatt G (2002) Meta-analyses of therapies for postmenopausal osteoporosis. III. Meta-analysis of risedronate for the treatment of postmenopausal osteoporosis. *Endocr Rev* 23(4):517-23.

22. Cranney A, Tugwell P, Zytaruk N, Robinson V, Weaver B, Adachi J, Wells G, Shea B, and Guyatt G (2002) Meta-analyses of therapies for postmenopausal osteoporosis. IV. Meta-analysis of raloxifene for the prevention and treatment of postmenopausal osteoporosis. *Endocr Rev* 23(4):524-8.

23. Cranney A, Wells G, Willan A, Griffith L, Zytaruk N, Robinson V, Black D, Adachi J, Shea B, Tugwell P, and Guyatt G (2002) Meta-analyses of therapies for postmenopausal osteoporosis. II. Meta-analysis of alendronate for the treatment of postmenopausal women. *Endocr Rev* 23(4):508-16.

24. Cummings SR, Karpf DB, Harris F, Genant HK, Ensrud K, LaCroix AZ, and Black DM (2002) Improvement in spine bone density and reduction in risk of vertebral fractures during treatment with antiresorptive drugs. *Am J Med* 112(4):281-9.

25. Cummings SR and Melton LJ (2002) Epidemiology and outcomes of osteoporotic fractures. *Lancet* 359(9319):1761-7.

26. Day JS, Murdoch DJ, and Dumas GA (2000) Calibration of position and angular data from a magnetic tracking device. *J Biomech* 33(8):1039-45.

27. Dempster DW, Ferguson-Pell MW, Mellish RW, Cochran GV, Xie F, Fey C, Horbert W, Parisien M, and Lindsay R (1993) Relationships between bone

structure in the iliac crest and bone structure and strength in the lumbar spine. *Osteoporos Int* 3(2):90-6.

28. Diaz Curiel M, Carrasco de la Peña JL, Honorato Perez J, Perez Cano R, Rapado A, and Ruiz Martinez I (1997) Study of bone mineral density in lumbar spine and femoral neck in a Spanish population. Multicentre Research Project on Osteoporosis. *Osteoporos Int* 7(1):59-64.
29. Dunnill MS, Anderson JA, and Whitehead R (1967) Quantitative histological studies on age changes in bone. *J Pathol Bacteriol* 94(2):275-91.
30. Feldkamp LA, Goldstein SA, Parfitt AM, Jesion G, and Kleerekoper M (1989) The direct examination of three-dimensional bone architecture in vitro by computed tomography. *J Bone Miner Res* 4(1):3-11.
31. Gabriel SE, Tosteson AN, Leibson CL, Crowson CS, Pond GR, Hammond CS, and Melton LJ, 3rd (2002) Direct medical costs attributable to osteoporotic fractures. *Osteoporos Int* 13(4):323-30.
32. Gadeleta SJ, Boskey AL, Paschalis E, Carlson C, Menschik F, Baldini T, Peterson M, and Rimnac CM (2000) A physical, chemical, and mechanical study of lumbar vertebrae from normal, ovariectomized, and nandrolone decanoate-treated cynomolgus monkeys (Macaca fascicularis). *Bone* 27(4):541-50.
33. Gibson LJ (1985) The mechanical behavior of cancellous bone. *J Biomech* 18:317-328.
34. Goldstein SA (1987) The mechanical properties of trabecular bone: dependence on anatomic location and function. *J Biomech* 20(11-12):1055-61.
35. Goldstein SA, Goulet R, and McCubbrey D (1993) Measurement and significance of three-dimensional architecture to the mechanical integrity of trabecular bone. *Calcif Tissue Int* 53:S127-32; discussion S132-3.

36. Goulet RW, Goldstein SA, Ciarelli MJ, Kuhn JL, Brown MB, and Feldkamp LA (1994) The relationship between the structural and orthogonal compressive properties of trabecular bone. *J Biomech* 27(4):375-89.
37. Griffiths MR, Noakes KA, and Pocock NA (1997) Correcting the magnification error of fan beam densitometers. *J Bone Miner Res* 12(1):119-23.
38. Grynpas M (1993) Age and disease-related changes in the mineral of bone. *Calcif Tissue Int* 53 Suppl 1:S57-64.
39. Guo XE, McMahon TA, Keaveny TM, Hayes WC, and Gibson LJ (1994) Finite element modeling of damage accumulation in trabecular bone under cyclic loading. *J Biomech* 27(2):145-55.
40. Handschin RG and Stern WB (1994) Crystallographic and chemical analysis of human bone apatite (Crista Iliaca). *Clin Rheumatol* 13 Suppl 1:75-90.
41. Handschin RG and Stern WB (1995) X-ray diffraction studies on the lattice perfection of human bone apatite (Crista iliaca). *Bone* 16(4 Suppl):355S-363S.
42. Harrigan TP, Jasty M, Mann RW, and Harris WH (1988) Limitations of the continuum assumption in cancellous bone. *J Biomech* 21(4):269-75.
43. Harrigan TP and Mann RW (1984) Characterization of microstructural anisotropy in orthotropic materials using a second rank tensor. *J Mater Sci* 19:761-767.
44. Hernandez CJ, Beaupré GS, Keller TS, and Carter DR (2001) The influence of bone volume fraction and ash fraction on bone strength and modulus. *Bone* 29(1):74-8.
45. Hildebrand T, Laib A, Müller R, Dequeker J, and Rüegsegger P (1999) Direct three-dimensional morphometric analysis of human cancellous bone: microstructural data from spine, femur, iliac crest, and calcaneus. *J Bone Miner Res* 14(7):1167-74.

46. Hildebrand T and Rüegsegger P (1997) A new method for the model-independent assessment of thickness in three-dimensional images. *J Microsc* 185:67-75.

47. Hodgskinson R and Currey JD (1992) Young's modulus, density and material properties in cancellous bone over a large density range. *J Mater Sci Mater Med* 3(377-381)

48. Hou FJ, Lang SM, Hoshaw SJ, Reimann DA, and Fyhrie DP (1998) Human vertebral body apparent and hard tissue stiffness. *J Biomech* 31(11):1009-15.

49. Hui SL, Slemenda CW, and Johnston CC, Jr. (1988) Age and bone mass as predictors of fracture in a prospective study. *J Clin Invest* 81(6):1804-9.

50. Jaasma MJ, Bayraktar HH, Niebur GL, and Keaveny TM (2002) Biomechanical effects of intraspecimen variations in tissue modulus for trabecular bone. *J Biomech* 35(2):237-46.

51. Jensen KS, Mosekilde L, and Mosekilde L (1990) A model of vertebral trabecular bone architecture and its mechanical properties. *Bone* 11(6):417-23.

52. Johnell O (1997) The socioeconomic burden of fractures: today and in the 21st century. *Am J Med* 103(2A):20S-25S; discussion 25S-26S.

53. Kabel J, Odgaard A, van Rietbergen B, and Huiskes R (1999) Connectivity and the elastic properties of cancellous bone. *Bone* 24(2):115-120.

54. Kabel J, van Rietbergen B, Dalstra M, Odgaard A, and Huiskes R (1999) The role of an effective isotropic tissue modulus in the elastic properties of cancellous bone. *J Biomech* 32(7):673-80.

55. Kanis JA, Melton LJ, 3rd, Christiansen C, Johnston CC, and Khaltaev N (1994) The diagnosis of osteoporosis. *J Bone Miner Res* 9(8):1137-41.

56. Kaplan SJ, Hayes WC, Stone JL, and Beaupre GS (1985) Tensile strength of bovine trabecular bone. *J Biomech* 18(9):723-7.

57. Keaveny TM (2001) Strength of trabecular bone. In: Cowin SC, Ed. Bone Mechanics Handbook. CRC Press: Boca Raton. pp. 16-1-16-42.

58. Keaveny TM, Guo XE, Wachtel EF, McMahon TA, and Hayes WC (1994) Trabecular bone exhibits fully linear elastic behavior and yields at low strains. *J Biomech* 27:1127-1136.

59. Keaveny TM, Pinilla TP, Crawford RP, Kopperdahl DL, and Lou A (1997) Systematic and random errors in compression testing of trabecular bone. *J Orthop Res* 15(1):101-10.

60. Keaveny TM, Wachtel EF, Ford CM, and Hayes WC (1994) Differences between the tensile and compressive strengths of bovine tibial trabecular bone depend on modulus. *J Biomech* 27(9):1137-46.

61. Kopperdahl DL and Keaveny TM (1998) Yield strain behavior of trabecular bone. *J Biomech* 31(7):601-8.

62. Kuhn JL, Goldstein SA, Choi K, London M, Feldkamp LA, and Matthews LS (1989) Comparison of the trabecular and cortical tissue moduli from human iliac crests. *J Orthop Res* 7(6):876-884.

63. Ladd AJ, Kinney JH, Haupt DL, and Goldstein SA (1998) Finite-element modeling of trabecular bone: comparison with mechanical testing and determination of tissue modulus. *J Orthop Res* 16(5):622-628.

64. Laib A, Kumer JL, Majumdar S, and Lane NE (2001) The temporal changes of trabecular architecture in ovariectomized rats assessed by MicroCT. *Osteoporos Int* 12(11):936-41.

65. Lehmann R, Wapniarz M, Randerath O, Kvasnicka HM, John W, Reincke M, Kutnar S, Klein K, and Allolio B (1995) Dual-energy X-ray absorptiometry at the lumbar spine in German men and women: a cross-sectional study. *Calcif Tissue Int* 56(5):350-4.

66. Linde F, Gøthgen CB, Hvid I, and Pongsoipetch B (1988) Mechanical properties of trabecular bone by a non-destructive compression testing approach. *Eng Med* 17(1):23-9.
67. Linde F and Hvid I (1989) The effect of constraint on the mechanical behaviour of trabecular bone specimens. *J Biomech* 22(5):485-90.
68. Linde F, Hvid I, and Pongsoipetch B (1989) Energy absorptive properties of human trabecular bone specimens during axial compression. *J Orthop Res* 7(3):432-9.
69. Lochmüller EM, Eckstein F, Kaiser D, Zeller JB, Landgraf J, Putz R, and Steldinger R (1998) Prediction of vertebral failure loads from spinal and femoral dual-energy X-ray absorptiometry, and calcaneal ultrasound: an in situ analysis with intact soft tissues. *Bone* 23(5):417-24.
70. Löfman O, Larsson L, Ross I, Toss G, and Berglund K (1997) Bone mineral density in normal Swedish women. *Bone* 20(2):167-74.
71. Lotz JC, Gerhart TN, and Hayes WC (1990) Mechanical properties of trabecular bone from the proximal femur: a quantitative CT study. *J Comput Assist Tomogr* 14(1):107-14.
72. Malluche HH, Meyer W, Sherman D, and Massry SG (1982) Quantitative bone histology in 84 normal American subjects. Micromorphometric analysis and evaluation of variance in iliac bone. *Calcif Tissue Int* 34(5):449-55.
73. Martin RB, Burr DB, and Sharkey NA. Skeletal Tissue Mechanics. New York: Springer, 1998.
74. Melton LJ, 3rd (1993) Hip fractures: a worldwide problem today and tomorrow. *Bone* 14:S1-8.
75. Melton LJ, 3rd (2000) Who has osteoporosis? A conflict between clinical and public health perspectives. *J Bone Miner Res* 15(12):2309-14.

76. Melton LJ, 3rd, Chrischilles EA, Cooper C, Lane AW, and Riggs BL (1992) Perspective. How many women have osteoporosis? *J Bone Miner Res* 7(9):1005-10.

77. Miller LM, Tibrewala J, and Carlson CS (2000) Examination of bone chemical composition in osteoporosis using fluorescence-assisted synchrotron infrared microspectroscopy. *Cell Mol Biol (Noisy-le-grand)* 46(6):1035-44.

78. Miller PD, Siris ES, Barrett-Connor E, Faulkner KG, Wehren LE, Abbott TA, Chen YT, Berger ML, Santora AC, and Sherwood LM (2002) Prediction of fracture risk in postmenopausal white women with peripheral bone densitometry: evidence from the National Osteoporosis Risk Assessment. *J Bone Miner Res* 17(12):2222-30.

79. Mittra E, Rubin C, and Qin YX (2005) Interrelationship of trabecular mechanical and microstructural properties in sheep trabecular bone. *J Biomech* 38(6):1229-37.

80. Morgan EF, Bayraktar HH, and Keaveny TM (2003) Trabecular bone modulus-density relationships depend on anatomic site. *J Biomech* 36(7):897-904.

81. Morgan TG, van der Meulen MCH, and Bourne BC (2002) Density versus depth from trabecular surface measured by quantitative microCT. *Trans Orthop Res Soc* 27:110.

82. Moro M, Hecker AT, Bouxsein ML, and Myers ER (1995) Failure load of thoracic vertebrae correlates with lumbar bone mineral density measured by DXA. *Calcif Tissue Int* 56(3):206-9.

83. Mosekilde L (1988) Age-related changes in vertebral trabecular bone architecture--assessed by a new method. *Bone* 9(4):247-50.

84. Mosekilde L (1989) Sex differences in age-related loss of vertebral trabecular bone mass and structure -- biomechanical consequences. *Bone* 10:425-432.

85. Mosekilde L and Mosekilde L (1986) Normal vertebral body size and compressive strength: relations to age and to vertebral and iliac trabecular bone compressive strength. *Bone* 7:207-12.

86. Mosekilde L and Mosekilde L (1990) Sex differences in age-related changes in vertebral body size, density and biomechanical competence in normal individuals. *Bone* 11:67-73.

87. Mosekilde L, Mosekilde L, and Danielsen CC (1987) Biomechanical competence of vertebral trabecular bone in relation to ash density and age in normal individuals. *Bone* 8(2):79-85.

88. Myers ER and Wilson SE (1997) Biomechanics of osteoporosis and vertebral fracture. *Spine* 22(24):25S-31S.

89. Myers ER, Yano KA, Moro M, Silva MJ, and Hayes WC (1996) Lumbar bone mineral density predicts thoracolumbar failure load in compression and flexion. *Trans Orthop Res Soc* 21:645.

90. National Osteoporosis Foundation (2002) America's Bone Health: The State of Osteoporosis and Low Bone Mass in Our Nation. Washington D.C.

91. Neil JL, Demos TC, Stone JL, and Hayes WC (1983) Tensile and compressive properties of vertebral trabecular bone. *Trans Orthop Res Soc* 8:344.

92. Niebur GL, Feldstein MJ, Yuen JC, Chen TJ, and Keaveny TM (2000) High-resolution finite element models with tissue strength asymmetry accurately predict failure of trabecular bone. *J Biomech* 33(12):1575-83.

93. Niebur GL, Yuen JC, Burghardt AJ, and Keaveny TM (2001) Sensitivity of damage predictions to tissue level yield properties and apparent loading conditions. *J Biomech* 34(5):699-706.

94. Ninomiya JT, Tracy RP, Calore JD, Gendreau MA, Kelm RJ, and Mann KG (1990) Heterogeneity of human bone. *J Bone Miner Res* 5(9):933-8.

95. Odgaard A, Kabel J, van Rietbergen B, Dalstra M, and Huiskes R (1997) Fabric and elastic principal directions of cancellous bone are closely related. *J Biomech* 30(5):487-495.

96. Odgaard A and Linde F (1991) The underestimation of Young's modulus in compressive testing of cancellous bone specimens. *J Biomech* 24(8):691-8.

97. Ott SM (1996) Theoretical and methodological approach. In: Bilezikian J, Raisz LG, and Rodan GR, Ed. Principles of Bone Biology. Academic Press: San Diego, CA. pp. 231-241.

98. Parfitt AM, Mathews CH, Villanueva AR, Kleerekoper M, Frame B, and Rao DS (1983) Relationships between surface, volume, and thickness of iliac trabecular bone in aging and in osteoporosis. Implications for the microanatomic and cellular mechanisms of bone loss. *J Clin Invest* 72(4):1396-409.

99. Paschalis EP, Betts F, DiCarlo E, Mendelsohn R, and Boskey AL (1997) FTIR microspectroscopic analysis of human iliac crest biopsies from untreated osteoporotic bone. *Calcif Tissue Int* 61(6):487-92.

100. Paschalis EP, Betts F, DiCarlo E, Mendelsohn R, and Boskey AL (1997) FTIR microspectroscopic analysis of normal human cortical and trabecular bone. *Calcif Tissue Int* 61(6):480-6.

101. Paschalis EP, DiCarlo E, Betts F, Sherman P, Mendelsohn R, and Boskey AL (1996) FTIR microspectroscopic analysis of human osteonal bone. *Calcif Tissue Int* 59(6):480-7.

102. Pocock NA, Noakes KA, Majerovic Y, and Griffiths MR (1997) Magnification error of femoral geometry using fan beam densitometers. *Calcif Tissue Int* 60(1):8-10.

103. Pugh JW, Rose RM, and Radin EL (1973) A structural model for the mechanical behavior of trabecular bone. *J Biomech* 6(6):657-70.

104. Raux P, Townsend PR, Miegel R, Rose RM, and Radin EL (1975) Trabecular architecture of the human patella. *J Biomech* 8(1):1-7.

105. Rho JY, Ashman RB, and Turner CH (1993) Young's modulus of trabecular and cortical bone material: ultrasonic and microtensile measurements. *J Biomech* 26(2):111-119.

106. Rho JY, Roy ME, 2nd, Tsui TY, and Pharr GM (1999) Elastic properties of microstructural components of human bone tissue as measured by nanoindentation. *J Biomed Mater Res* 45(1):48-54.

107. Rho JY, Tsui TY, and Pharr GM (1997) Elastic properties of human cortical and trabecular lamellar bone measured by nanoindentation. *Biomaterials* 18(20):1325-1330.

108. Rice JC, Cowin SC, and Bowman JA (1988) On the dependence of the elasticity and strength of cancellous bone on apparent density. *J Biomech* 21(2):155-68.

109. Riggs BL and Melton LJ, 3rd (1986) Involutional osteoporosis. *N Engl J Med* 314(26):1676-86.

110. Riggs BL and Melton LJ, 3rd (1995) The worldwide problem of osteoporosis: insights afforded by epidemiology. *Bone* 17(5):505S-511S.

111. Riggs BL, Wahner HW, Seeman E, Offord KP, Dunn WL, Mazess RB, Johnson KA, and Melton LJ, 3rd (1982) Changes in bone mineral density of the proximal femur and spine with aging. Differences between the postmenopausal and senile osteoporosis syndromes. *J Clin Invest* 70(4):716-23.

112. Rohl L, Larsen E, Linde F, Odgaard A, and Jorgensen J (1991) Tensile and compressive properties of cancellous bone. *J Biomech* 24(12):1143-9.

113. Rohlmann A, Zilch H, Bergmann G, and Kolbel R (1980) Material properties of femoral cancellous bone in axial loading. Part I: Time independent properties. *Arch Orthop Trauma Surg* 97(2):95-102.

114. Ross PD, Davis JW, Epstein RS, and Wasnich RD (1991) Pre-existing fractures and bone mass predict vertebral fracture incidence in women. *Ann Intern Med* 114(11):919-23.

115. Ross PD, Davis JW, Vogel JM, and Wasnich RD (1990) A critical review of bone mass and the risk of fractures in osteoporosis. *Calcif Tissue Int* 46(3):149-61.

116. Rüegsegger P, Koller B, and Müller R (1996) A microtomographic system for the nondestructive evaluation of bone architecture. *Calcif Tissue Int* 58(1):24-9.

117. Sarkar S, Mitlak BH, Wong M, Stock JL, Black DM, and Harper KD (2002) Relationships between bone mineral density and incident vertebral fracture risk with raloxifene therapy. *J Bone Miner Res* 17(1):1-10.

118. Schuit SC, van der Klift M, Weel AE, de Laet CE, Burger H, Seeman E, Hofman A, Uitterlinden AG, van Leeuwen JP, and Pols HA (2004) Fracture incidence and association with bone mineral density in elderly men and women: the Rotterdam Study. *Bone* 34(1):195-202.

119. Shypailo RJ, Posada JK, and Ellis KJ (1998) Whole-body phantoms with anthropomorphic-shaped skeletons for evaluation of dual-energy X-ray absorptiometry measurements. *Appl Radiat Isot* 49(5-6):503-5.

120. Silva MJ and Gibson LJ (1997) Modeling the mechanical behavior of vertebral trabecular bone: effects of age-related changes in microstructure. *Bone* 21(2):191-9.

121. Simmons CA and Hipp JA (1997) Method-based differences in the automated analysis of the three-dimensional morphology of trabecular bone. *J Bone Miner Res* 12(6):942-7.

122. Siris ES, Miller PD, Barrett-Connor E, Faulkner KG, Wehren LE, Abbott TA, Berger ML, Santora AC, and Sherwood LM (2001) Identification and fracture

outcomes of undiagnosed low bone mineral density in postmenopausal women: results from the National Osteoporosis Risk Assessment. *JAMA* 286(22):2815-22.

123. Snyder BD, Piazza S, Edwards WT, and Hayes WC (1993) Role of trabecular morphology in the etiology of age-related vertebral fractures. *Calcif Tissue Int* 53 Suppl 1:S14-22.
124. Stone JL, Beaupre GS, and Hayes WC (1983) Multiaxial strength characteristics of trabecular bone. *J Biomech* 16(9):743-52.
125. Thomsen JS, Ebbesen EN, and Mosekilde L (2000) A new method of comprehensive static histomorphometry applied on human lumbar vertebral cancellous bone. *Bone* 27(1):129-38.
126. Thomsen JS, Ebbesen EN, and Mosekilde L (2002) Predicting human vertebral bone strength by vertebral static histomorphometry. *Bone* 30(3):502-8.
127. Tothill P and Hannan WJ (2000) Comparisons between Hologic QDR 1000W, QDR 4500A, and Lunar Expert dual-energy X-ray absorptiometry scanners used for measuring total body bone and soft tissue. *Ann NY Acad Sci* 904:63-71.
128. Tothill P, Hannan WJ, and Wilkinson S (2001) Comparisons between a pencil beam and two fan beam dual energy X-ray absorptiometers used for measuring total body bone and soft tissue. *Br J Radiol* 74(878):166-76.
129. Townsend PR, Raux P, Rose RM, Miegel RE, and Radin EL (1975) The distribution and anisotropy of the stiffness of cancellous bone in the human patella. *J Biomech* 8(6):363-7.
130. Turner CH, Cowin SC, Rho JY, Ashman RB, and Rice JC (1990) The fabric dependence of the orthotropic elastic constants of cancellous bone. *J Biomech* 23(6):549-61.

131. Turner CH, Rho J, Takano Y, Tsui TY, and Pharr GM (1999) The elastic properties of trabecular and cortical bone tissues are similar: results from two microscopic measurement techniques. *J Biomech* 32(4):437-41.

132. Ulrich D, Hildebrand T, van Rietbergen B, Müller R, and Rüegsegger P (1997) The quality of trabecular bone evaluated with micro-computed tomography, FEA and mechanical testing. *Stud Health Technol Inform* 40:97-112.

133. Underwood EE. Quantitative Stereology. Reading, MA: Addison-Wesley, 1970.

134. U.S. Department of Health and Human Services, Office of the Surgeon General (2004) Bone Health and Osteoporosis: A Report of the Surgeon General. Rockville, MD.

135. van der Linden JC, Birkenhager-Frenkel DH, Verhaar JA, and Weinans H (2001) Trabecular bone's mechanical properties are affected by its non-uniform mineral distribution. *J Biomech* 34(12):1573-80.

136. van Rietbergen B, Majumdar S, Pistoia W, Newitt DC, Kothari M, Laib A, and Rüegsegger P (1998) Assessment of cancellous bone mechanical properties from micro-FE models based on micro-CT, pQCT and MR images. *Technol Health Care* 6(5-6):413-20.

137. van Rietbergen B, Weinans H, and Huiskes R (1997) Prospects of computer models for the prediction of osteoporotic bone fracture risk. *Stud Health Technol Inform* 40:25-32.

138. van Rietbergen B, Weinans H, Huiskes R, and Odgaard A (1995) A new method to determine trabecular bone elastic properties and loading using micromechanical finite-element models. *J Biomech* 28(1):69-81.

139. Vega E, Bagur A, and Mautalen CA (1993) Densidad mineral âosea en mujeres osteoporâoticas y normales de Buenos Aires. *Medicina* 53(3):211-6.

140. Vrijhoef MM and Driessens FC (1971) On the interaction between specimen and testing machine in mechanical testing procedures. *J Biomech* 4(4):233-8.

141. Weaver JK and Chalmers J (1966) Cancellous bone: its strength and changes with aging and an evaluation of some methods for measuring its mineral content. *J Bone Joint Surg Am* 48(2):289-98.

142. Whitehouse WJ (1974) The quantitative morphology of anisotropic trabecular bone. *J Microsc* 101:153-268.

143. Yamada H. Strength of Biological Materials. Huntington: Krieger, 1973.

144. Yeh OC and Keaveny TM (1999) Biomechanical effects of intraspecimen variations in trabecular architecture: a three-dimensional finite element study. *Bone* 25(2):223-8.

145. Zysset PK, Guo XE, Hoffler CE, Moore KE, and Goldstein SA (1999) Elastic modulus and hardness of cortical and trabecular bone lamellae measured by nanoindentation in the human femur. *J Biomech* 32(10):1005-1012.

CHAPTER 2

FAN-BEAM DENSITOMETRY OF THE GROWING SKELETON *ARE WE MEASURING WHAT WE THINK WE ARE?*[*]

Introduction

Fan-beam densitometers are frequently used to assess bone mass in children and adults. They are often preferred to pencil-beam densitometers because of shorter scan times and higher spatial resolution. The isocentric acquisition method, which involves a single pass of the fan-shaped X-ray beam longitudinally along the site of interest, is used in wide-angle fan-beam machines and minimizes the amount of data overlap or under-sampling that may occur with a rectilinear acquisition technique used in pencil-beam machines. However, the geometry of the fan beam produces a magnification error in areal bone measures that decreases with distance from the X-ray source [13]. An object lying closer to the source is hit with a broader angle of X-rays, producing a wider incidence of transmitted and deflected X-rays on the detector array (Figure 2.1). Thus, the projected area increases as the distance between the object and the X-ray source decreases.

Prior studies of wide-angle fan-beam densitometers have shown linear variations of mass [27,28], observed width [13], and hip axis length [1,23] with distance from the X-ray source. Projected bone area (A, cm^2), bone mineral content (BMC, g), and areal

---

[*] Reprinted from *J Clin Densitom*, Vol. 8, Cole JH, Scerpella TA, and van der Meulen MCH, Fan-beam densitometry of the growing skeleton: are we measuring what we think we are?, pp. 57-64, Copyright (2005), with permission from the International Society for Clinical Densitometry.

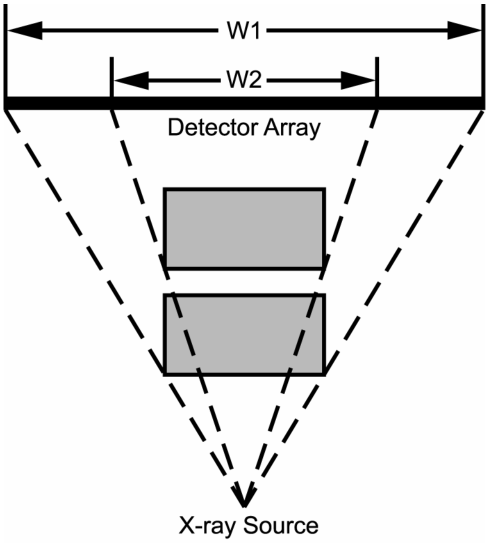

Figure 2.1. The effect of fan-beam magnification increases with proximity to the X-ray source. An object lying closer to the source has a larger detected width (W1) than does an identical object positioned farther away from the source (W2).

bone mineral density (BMD, g/cm^2) decreased by 2.8%, 3.1%, and 0.2% per cm distance above the source, respectively, for an anthropomorphic spine phantom over a distance range of 0-12 cm [4], although the statistical significance or specific nature of these variations were not reported. Increases of 1.0-5.1% in BMC and of 0.8-4.1% in BMD have been observed in anthropomorphic whole body phantoms for a simulated increase in subcutaneous fat of 2 cm [26]. Many dual energy X-ray absorptiometry (DXA) studies have compared fan-beam data either to pencil-beam data for the purpose of cross-calibration [2,4,5,9-11,17,24,27,28] or to reference values for validation [14,15,29,30]. However, the effect of the magnification error on bone accrual measures (i.e., the specific relationship of A, BMC, and BMD with distance from the X-ray source) was not quantified in any of these studies. Understanding which bone mineral measures vary and how they vary with distance from the source is a necessary first step in developing correction techniques for fan-beam magnification error.

Errors in measures of bone mineral due to fan-beam densitometry are of particular concern for longitudinal studies of adolescent subjects, who may experience significant growth between consecutive examinations. Increased body thickness due to normal growth increases the distance between the subject and the X-ray source and produces magnification errors in bone measures. The magnitude of error from the studies noted above (1-5%) is comparable to the magnitude of change in bone measurements reported in clinical bone density studies on growing subjects. For example, longitudinal studies of adolescent female gymnasts observed an average annual increase in total body BMD of 3.4-5.6% [3,8,21]. Pre-pubertal and early pubertal children experienced increases of 2.9-6.9% in A, 7.0-12.0% in BMC, and 1.4-12.0% in BMD at the femoral neck, lumbar spine, and total body over a period of 7 to 8 months following exercise intervention [12,18-20,22]. Therefore, in clinical studies involving growing subjects, the change in bone accrual measures with distance from the X-ray source could obscure increases associated with growth, loading, or other interventions. Quantifying and correcting magnification error is crucial for analyzing and reporting data from bone density studies accurately.

We hypothesized that A, BMC, and BMD would vary linearly with distance from the X-ray source in wide-angle fan-beam densitometers. This study was designed to quantify these specific relationships and to examine the variability of each measurement over a particular distance range using phantoms of known geometry, material properties, and location within the scan. Understanding these relationships may help to correct the magnification error associated with fan-beam densitometry and, therefore, to assess bone accrual accurately over time in growing subjects.

Materials and Methods

Test Phantom

Four sets of 6061-T6 aluminum rods with different cross-sectional geometry were scanned using dual energy X-ray absorptiometry (DXA). The geometries of the rods were chosen to test partial volume sensitivity (by comparing hollow and solid round rods) and edge detection sensitivity (by comparing round rods to both square and rectangular rods) of the densitometry software. Rectangular rods were used to examine edge detection for rods with the same incident shape (i.e., same shape on the bottom surface, as seen by the X rays) but with different volumes. Therefore, the wider side was placed parallel to the table surface.

Hollow round rods (outer diameter 2.49 cm, inner diameter 1.27 cm), solid round rods (diameter 2.49 cm), solid square rods (2.54 cm x 2.54 cm) and solid rectangular rods (2.54 cm x 0.64 cm) were scanned at four distances from the X-ray source, as measured by distance above the scanning table (3.5, 7.0, 10.5, 14.0 cm). Scans were acquired with a fan-beam densitometer (Delphi QDR 4500A, Hologic Inc., Bedford, MA) in lumbar spine array mode. This distance range encompassed more than the expected distance range of femora in growing subjects. All rods had a nominal length of 15.2 cm. To simulate the presence of soft tissue, the rods were submerged in a 16.5-cm water bath using a custom Plexiglas® box with solid sides and bottom and open top, and Plexiglas® inserts were used to hold the rods at the specified distances from the source (Figure 2.2).

Each set of rods was scanned in two orientations, superior-inferior (SI) and medial-lateral (ML). In the SI orientation, the longitudinal axes of the rods were parallel to the long axis of the table (rod cross-sections perpendicular to scanning direction), and in the ML orientation, the longitudinal axes of the rods were

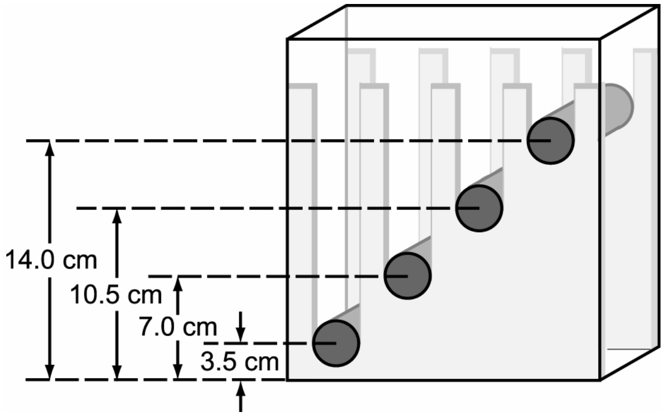

Figure 2.2. Illustration of the Plexiglas® phantom box with inserts for the round rods. Another set of inserts was used for the square and rectangular rods. The box was filled with water to the top edge of the inserts to simulate soft tissue.

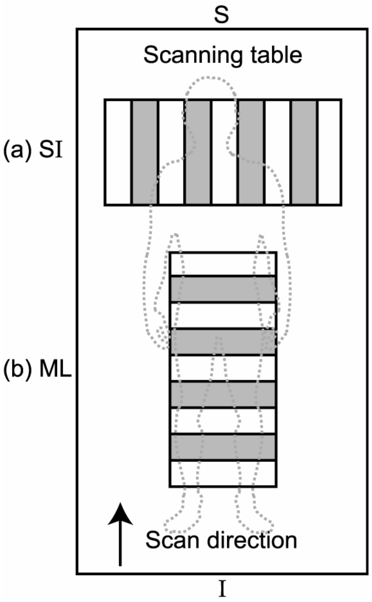

Figure 2.3. Scanning configuration for the aluminum rods in the (a) superior-inferior (SI) orientation and (b) medial-lateral (ML) orientation. The cross-section of the rods in the SI orientation is parallel to the scan direction, and the cross-section of the rods in the ML orientation is perpendicular to the scan direction.

perpendicular to the long axis of the table (rod cross-sections parallel to scan direction) (Figure 2.3). The box was not repositioned between scans of like orientation to minimize errors in the data. For the ML orientation, each set of rods was scanned twice, once with the rods arranged smallest to largest distance from the source and once with them arranged largest to smallest distance from the source. For the SI orientation, the rods were scanned 5 times, once with the scan centerline aligned with the centerline of the phantom box and once with the scan centerline aligned with the centerline of each of the 4 rods.

Table 2.1. Subset of analyses for individual scans in the superior-inferior orientation, including scan center and rods analyzed.

		Rods Analyzed			
Rod Type	Centered About	3.5 cm	7.0 cm	10.5 cm	14.0 cm
Hollow Round	Box		X	X	
	3.5 cm rod	X	X		
	7.0 cm rod	X	X	X	
	10.5 cm rod		X *	X	X
	14.0 cm rod			X	X
Solid Round	Box		X	X	
	3.5 cm rod	X			
	7.0 cm rod	X	X	X	
	10.5 cm rod		X	X	X
	14.0 cm rod			X	X
Square	Box		X	X	
	3.5 cm rod	X			
	7.0 cm rod	X	X	X *	
	10.5 cm rod		X	X	X
	14.0 cm rod			X	X
Rectangular	Box		X	X	
	3.5 cm rod	X			
	7.0 cm rod		X		
	10.5 cm rod		X	X	
	10.5 cm rod		X	X	X
	14.0 cm rod			X	X

* Excluded from statistical analyses

Each scan was analyzed multiple times on different regions of interest to obtain data for each rod within the field of view (Table 2.1). For a given scan, only those rods that fit completely within the field of view were analyzed. Due to the width of the lumbar spine scan and the arrangement of the rods within the phantom box, a maximum of 3 rods fit within the scan field of view for the SI orientation, and all rods were visible in the ML orientation. The rod edges were poorly detected by the analysis software for the solid square rod at a distance of 10.5 cm in the scan centered about the 7.0 cm rod and for the hollow round rod at a distance of 7.0 cm in the scan centered about the 10.5 cm rod. Therefore, these data were excluded from all analyses.

To examine repeatability, the solid round rods and solid square rods were each scanned ten times in the SI orientation with the scan centerline aligned with the centerline of the phantom box. The box was repositioned between scans. Each scan was analyzed twice, once for rods positioned at a distance of 7.0 cm and once for rods positioned 10.5 cm above the scanning table. All scans were acquired and analyzed by a single operator to determine the measured area A, measured mineral content (hereafter referred to as measured BMC), and measured mineral density (hereafter referred to as measured BMD) for each rod in each scan (Hologic software version 11.2).

Statistical Analysis

Linear regressions were performed for A, measured BMC, and measured BMD with distance above the X-ray source, as measured by distance above the scanning table for each rod type and scan orientation (SAS 8, SAS Institute Inc., Cary, NC). Variability of A, measured BMC, and measured BMD was assessed using coefficients of variation (COV). Eleven observations were included in the regressions and COV for each rod type in the SI orientation, except for the solid square rods, which had only ten observations due to the excluded data. Eight observations were included in the analyses for the ML orientation. Repeatability was assessed using COV for A, measured BMC, and measured BMD of each distance (7.0 and 10.5 cm) for both solid round and solid square rods. In addition, paired t-tests were conducted on the repeatability data to analyze the differences between the two distances for each rod type for A, measured BMC, and measured BMD. A significance level of 0.05 was used for all calculations.

Results

Projected area decreased linearly with distance above the X-ray source, as assessed using distance above the table, for all rod types in the SI orientation ($p<0.005$, Figure 2.4). The slopes of the regression lines were similar for all rods and ranged from -0.52 for the solid square rods to -0.64 for the solid rectangle rods, resulting in a rate of change of –1.6% to –1.9% per cm. These relationships were strong, accounting for 94%, 94%, 68%, and 91% of the variability in the data for the hollow round rods, solid round rods, square rods, and rectangular rods, respectively (Table 2.2). When analyzing only those rods centered within the scans, the linear regressions became stronger, accounting for 92-99% of the variability in the data, while those rods not centered within the scans accounted for 67-96%. Measured BMC also decreased linearly with distance above the source for hollow and solid round rods in the SI orientation ($p<0.0001$, $r^2=0.97$, Figure 2.5), although these fits varied little with position of the rods within the scans. The slopes for the measured BMC

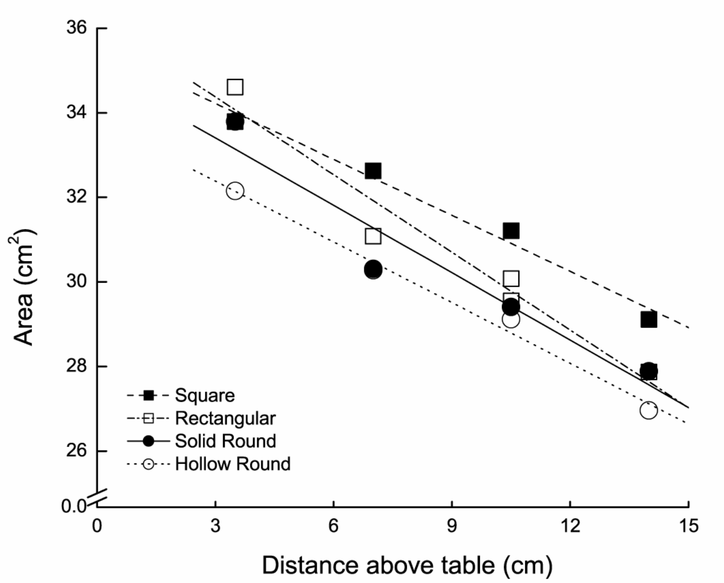

Figure 2.4. Linear regressions of area with distance above the X-ray source (as measured by distance above the scanning table) for a subset of centered rods in the superior-inferior orientation. All regressions had a significant slope, ranging from -0.52 to -0.64 ($p < 0.005$). Interaction between rod type and distance above source was not significant ($p = 0.70$).

Table 2.2. Coefficients of determination (r^2) and p-values for linear regressions of Area (A), measured bone mineral content (BMC), and measured bone mineral density (BMD) with distance above the X-ray source.

		Hollow Round		Solid Round		Square		Rectangular	
Regression	Orientation	r^2	p-value	r^2	p-value	r^2	p-value	r^2	p-value
A vs. Distance	SI	0.938	<0.0001	0.941	<0.0001	0.682	0.0033	0.914	<0.0001
	ML	0.458	0.065	0.070	0.53	----	----	----	----
BMC vs. Distance	SI	0.966	<0.0001	0.966	<0.0001	0.048	0.54	0.013	0.74
	ML	0.838	0.0014	0.032	0.67	----	----	----	----
BMD vs. Distance	SI	0.171	0.21	0.014	0.73	0.273	0.12	0.025	0.64
	ML	0.839	0.0014	0.100	0.44	----	----	----	----

SI = superior-inferior, ML = medial-lateral

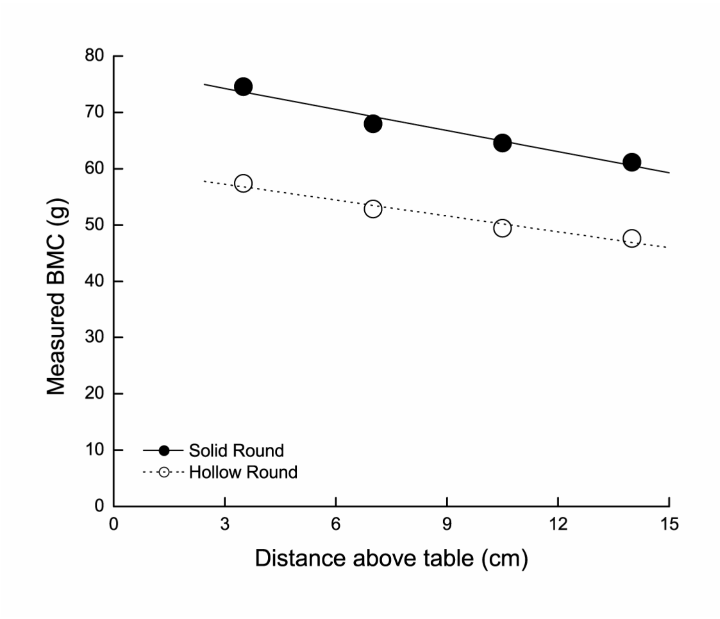

Figure 2.5. Linear regressions of measured mineral content (BMC) with distance above the X-ray source as measured by distance above the scanning table for centered round rods in the SI orientation. Regressions for both hollow and solid round rods had a significant slope of -1.0 and -1.3, respectively ($p < 0.0001$).

regressions were greater than those for A and ranged from –1.3 for solid round rods to –1.0 for hollow round rods, resulting in rates of change of –1.7% to –1.8% per cm. No significant linear relationship was found between measured BMD and distance above the source for any of the rods in the SI orientation. The interaction between rod type and distance above the source was not significant for area (p=0.70), measured BMC (p=0.18), or measured BMD (p=0.055). The only significant linear relationships for the ML orientation were measured BMC and measured BMD versus distance from the source for the hollow round rods (r^2=0.84 for both), with slopes of –0.47 and –0.02, respectively, and rates of change of –0.9% and –0.8% per cm, respectively. No other significant linear relationships were present for A, measured BMC, or measured BMD with distance above the X-ray source.

Table 2.3. Coefficients of variation (standard deviation/mean) for all rod types and both orientations (SI = superior-inferior and ML = medial-lateral) over a height range of 3.5-14 cm.

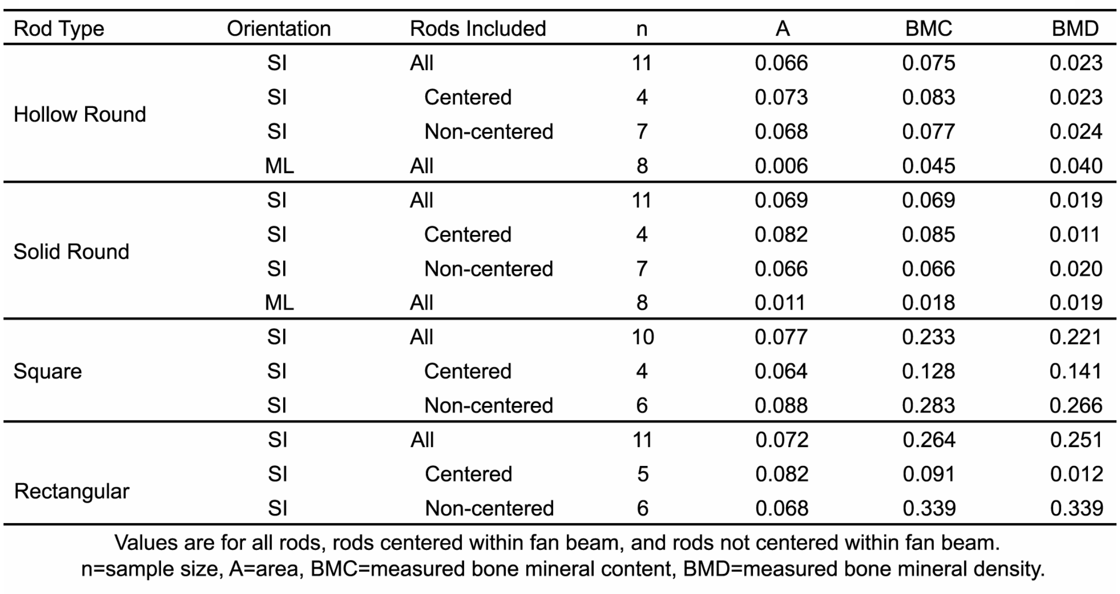

Rod Type	Orientation	Rods Included	n	A	BMC	BMD
Hollow Round	SI	All	11	0.066	0.075	0.023
	SI	Centered	4	0.073	0.083	0.023
	SI	Non-centered	7	0.068	0.077	0.024
	ML	All	8	0.006	0.045	0.040
Solid Round	SI	All	11	0.069	0.069	0.019
	SI	Centered	4	0.082	0.085	0.011
	SI	Non-centered	7	0.066	0.066	0.020
	ML	All	8	0.011	0.018	0.019
Square	SI	All	10	0.077	0.233	0.221
	SI	Centered	4	0.064	0.128	0.141
	SI	Non-centered	6	0.088	0.283	0.266
Rectangular	SI	All	11	0.072	0.264	0.251
	SI	Centered	5	0.082	0.091	0.012
	SI	Non-centered	6	0.068	0.339	0.339

Values are for all rods, rods centered within fan beam, and rods not centered within fan beam.
n=sample size, A=area, BMC=measured bone mineral content, BMD=measured bone mineral density.

The variability of A, measured BMC, and measured BMD was examined using coefficients of variation (Table 2.3). Over a distance range of 3.5 to 14 cm, the variability in area measurements was 6.6% for hollow round rods, 6.9% for solid round rods, 7.7% for square rods, and 7.2% for rectangular rods in the SI orientation. The variability in measured BMC was 7.5% and 6.9% for hollow and solid round rods, respectively, which was similar to the variability in A. However, the variability of measured BMC for the square and rectangular rods was much greater, with values of 23.3% and 26.4%, respectively. The variability of measured BMD was 2.3% for hollow round rods, 1.9% for solid round rods, 22.1% for square rods, and 25.1% for rectangular rods. In general, the coefficient of variation for centered rods was not consistently greater than or less than that of non-centered rods. For the ML orientation, variability for hollow and solid round rods, respectively, was 0.6% and 1.1% for A, 4.5% and 1.8% for measured BMC, and 4.0% and 1.9% for measured

BMD. The ML scans for the square and rectangular rods could not be analyzed by the analysis software.

The repeatability scans revealed COVs ranging from 0.29% to 0.97% (Table 2.4). Since the variability of the measurements was very small (standard deviations were less than 1% of the means), these measurements were highly repeatable. The measurements of A, measured BMC, and measured BMD at a distance of 7.0 cm above the scanning table were significantly greater than those at a distance of 10.5 cm for both solid round and solid square rods ($p<0.0001$). For the solid round rods, the mean difference between the measurements at a distance of 7.0 cm and those at 10.5 cm was 1.62 ± 0.25 cm^2 for A, 5.16 ± 0.50 g for measured BMC, and 0.051 ± 0.012 g/cm^2 for measured BMD. For the solid square rods, the mean difference was 2.43 ± 0.15 cm^2 for A, 8.67 ± 0.68 g for measured BMC, and 0.063 ± 0.025 g/cm^2 for measured BMD.

Table 2.4. Mean, standard deviation (SD), and coefficient of variation (COV) for repeatability measurements of Area (A), measured bone mineral content (BMC), and measured bone mineral density (BMD).

	Distance from Source	A (cm^2)			BMC (g)			BMD (g/cm^2)		
		Mean	SD	COV (%)	Mean	SD	COV (%)	Mean	SD	COV (%)
Solid Round	7.0 cm *	30.87	0.21	0.67	69.80	0.56	0.80	2.261	0.006	0.29
	10.5 cm	29.25	0.13	0.45	64.64	0.19	0.29	2.210	0.012	0.52
Solid Square	7.0 cm *	33.47	0.26	0.76	92.11	0.30	0.33	2.752	0.025	0.92
	10.5 cm	31.04	0.18	0.57	83.44	0.81	0.97	2.689	0.019	0.72

* Mean A, measured BMC, and measured BMD were greater at a distance of 7.0 cm than at 10.5 cm ($p<0.0001$).

Discussion

Area and measured bone mineral content decreased by 1.6-1.9% per cm increase in distance above the X-ray source, and these measurements varied by 6.6-26.4%, for rods in the SI orientation over the 10.5-cm distance range examined. Based on a pilot study with only hollow round rods, we had anticipated that area would vary with distance from the X-ray source at a greater rate than would BMC, thereby causing BMD, which is calculated as BMC per area, to also vary with distance from the source. Although no significant linear relationship was found in the present study, measured BMD varied by 1.9-2.3% over the distance range examined for the round aluminum rods in the SI orientation and over 20% for the square and rectangular rods. This lack of precision is troublesome, especially since BMD acquired from fan-beam densitometers is widely used in clinical studies due to its short scan acquisition time and improved spatial resolution. Exercise intervention studies in growing children have shown BMD changes at multiple sites on the same order as the smallest BMD variations measured here [12,19,22]. Therefore, accurately detecting BMD changes in longitudinal studies of growing children can be problematic when using fan-beam densitometry unless the magnification error is corrected.

Detecting BMD changes in growing subjects is difficult for any study where bone accrual is a measurement of interest. For example, pubertal subjects in studies without exercise or hormonal interventions experienced 15.6% and 5.5% increases in total body BMC and BMD, respectively, over an 18-month period [6]. Similarly, control subjects in the aforementioned exercise-intervention studies experienced increases in BMD of 1.2-3.9% at total body, 1.2-6.8% at the lumbar spine, and 1.7-3.9% at the femoral neck over a period of 7 months to 1 year [3,8,12,18-22]. Increases for the control groups were generally less than those for the intervention groups. However, both groups experienced bone accrual in amounts similar to the false decreases in measurements seen here, which resulted from magnification error over the distance range examined.

The magnitude of the magnification error noted here suggests that growth-related gains in limb and trunk girths may obscure longitudinal changes in bone density or bone geometry resulting from other factors, such as exercise or drug treatment. As body thickness increases, bones move farther away from the X-ray source. The present study suggests this would result in an apparent decrease in projected bone area and BMC due to changes in soft tissue, potentially leading to an underestimation of bone mineral accrual. Based on our preliminary data from a clinical longitudinal study [25], girth changes are often significant between DXA scanning periods and can easily reach 3-5 cm (8-20%) at the thigh, which results in a distance change of approximately 0.5-0.8 cm above the source (and hence above the table). For comparison, an increase in distance above the X-ray source of 0.5-0.8 cm resulted in a decrease of 0.9-1.4% in area and 1.0-1.6% in measured BMC for the hollow round aluminum rods in this study. Skeletal sites with little soft tissue mass, such as the forearm, will have much less distortion than sites with a greater amount of soft tissue mass, such as the femoral neck.

In the densitometer used in this study, the radiation source was located beneath the scanning table, and the detector array was located above the table. Other densitometry devices may have a less common configuration, in which the radiation source is positioned above and the detectors are positioned below the scanning table [13]. Assuming a similar magnification effect on bone measurements as with the scanner used in the present study, bones of growing subjects would become closer to the X-ray source and, therefore, experience an apparent increase in BMC and projected area over time. This would potentially lead to an overestimation of bone mineral accrual.

The difference in the linear relationships between the SI and ML orientations was not surprising. The rods in the SI orientation were not only scanned at different distances from the X-ray source but also at different locations within the fan beam. Therefore, the X-ray beam hit the rods at the edge of the field of view at different angles than rods in the center, which may have contributed to the larger degree of variability (and hence lower precision) seen in the SI measurements. The rods in the ML orientation were all centered within the field of view and therefore were affected only by distance above the X-ray source and not by position within the fan beam. Consequently, the data for the ML rods had less variability. Although the linear relationships for measured BMC and measured BMD in the ML orientation were significant, the slopes were smaller than those for the SI orientation and were possibly below a level of clinical significance.

The variability in area, measured BMC, and measured BMD data was similar for hollow and solid round rods in the SI orientation (COV of 0.023-0.066 and 0.019-0.069, respectively). In the ML orientation, these data were much more variable for the hollow round rods than for the solid round rods (COV of 0.006-0.040 and 0.011-0.019, respectively) and thus were much less precise in measurements of area, BMC, and BMD. Therefore, the fan-beam scanner used in this study appears sensitive to partial volume effects but only in the direction perpendicular to the scan direction. This is inconsequential clinically, given that bones with a thick cortex and central marrow cavity (as simulated by the hollow round rods) in the skeletal regions commonly measured by DXA are aligned longitudinally along the table, which corresponds to the SI orientation in this study. The femoral neck, a region of great interest clinically but not aligned along the SI axis, is composed primarily of cancellous bone. The complex marrow cavities generated by the trabecular structure are on a scale too small to be resolved by DXA and, at the apparent level, will likely behave more like the solid round rods. Therefore, partial volume effects likely will not be seen in the femoral neck as seen here with the hollow round rods.

Measurements for the square and rectangular rods were more variable (COV of 0.077-0.233 and 0.072-0.264, respectively), which indicates possible problems with edge detection. Visual inspection of the scans for the square and rectangular rods revealed that the rod edges identified by the analysis algorithm appeared more variable than those for the round rods. The lack of a significant relationship for measurements with distance above the X-ray source for the square and rectangular rods is not surprising, given that the variability in measurements was much larger than in the round rods. Had the edges been detected more reliably, perhaps the same linear relationships would have also been found in the square and rectangular rods.

Researchers acknowledge that BMD reported by DXA is an areal measure and may reflect changes in the bone geometry, changes in volumetric bone density, or both. The individual contributions of each of these cannot be isolated. Thus, many choose BMC as a more accurate measure of bone accrual, or they compute bone mineral apparent density (BMAD, g/cm^3), which is an estimate of volumetric density based on various geometric assumptions [7,16]. BMAD is calculated using BMC and some exponential form of area specific for each site of interest. However, as seen from this study using a fan-beam densitometer, both BMC and area vary linearly with distance above the X-ray source and, therefore, can also be problematic for the assessment of bone accrual in the growing skeleton.

In conclusion, we have identified significant magnification effects in areal measures using a wide-angle fan-beam densitometer, and we have shown that such magnification reduces the accuracy of DXA measurements. The variation of area and measured bone mineral content with distance from the X-ray source have been quantified for the round rods, which most closely mimic human bone *in vivo*. These relationships are linear and repeatable and theoretically provide an analytical correction for clinical DXA scans, provided the distance of a given bone above the scanning table can be determined. Such corrections are specific to the particular DXA machine used in this study. In spite of variability between specific DXA machines of the same model and between models of different manufacturers, however, we expect these findings to be at least qualitatively true for all wide-angle fan-beam densitometers due to the inherent nature of the X-ray beam profile. The identified magnification effects are important in studies involving growing subjects, as increasing girths move bones farther from the X-ray source and may distort BMC and area over time. The reduced accuracy of areal bone measurements may obscure the effect of a particular intervention. Therefore, the quantification and correction of magnification errors associated with fan-beam densitometry is crucial to studies involving growing subjects and is necessary for accurate determination of bone mineral accrual using DXA.

References

1. Barden HS, Settergren D, McClintock C, and Turner CH (2001) Measurement of Femur Geometry (HAL) with PRODIGY Is Accurate and Unaffected by Magnification. *J Bone Miner Res* 16(Suppl 1):S345.
2. Barthe N, Braillon P, Ducassou D, and Basse-Cathalinat B (1997) Comparison of two Hologic DXA systems (QDR 1000 and QDR 4500/A). *Br J Radiol* 70(835):728-39.
3. Bass S, Pearce G, Bradney M, Hendrich E, Delmas PD, Harding A, and Seeman E (1998) Exercise before puberty may confer residual benefits in bone density in adulthood: studies in active prepubertal and retired female gymnasts. *J Bone Miner Res* 13(3):500-7.
4. Blake GM, Parker JC, Buxton FM, and Fogelman I (1993) Dual X-ray absorptiometry: a comparison between fan beam and pencil beam scans. *Br J Radiol* 66(790):902-6.
5. Bouyoucef SE, Cullum ID, and Ell PJ (1996) Cross-calibration of a fan-beam X-ray densitometer with a pencil-beam system. *Br J Radiol* 69(822):522-31.
6. Cadogan J, Blumsohn A, Barker ME, and Eastell R (1998) A longitudinal study of bone gain in pubertal girls: anthropometric and biochemical correlates. *J Bone Miner Res* 13(10):1602-12.
7. Carter DR, Bouxsein ML, and Marcus R (1992) New approaches for interpreting projected bone densitometry data. *J Bone Miner Res* 7(2):137-45.
8. Courteix D, Lespessailles E, Jaffré C, Obert P, and Benhamou CL (1999) Bone material acquisition and somatic development in highly trained girl gymnasts. *Acta Paediatr* 88(8):803-8.

9. Eiken P, Kolthoff N, Bärenholdt O, Hermansen F, and Pors Nielsen S (1994) Switching from DXA pencil-beam to fan-beam. II: Studies in vivo. *Bone* 15(6):671-6.

10. Ellis KJ and Shypailo RJ (1998) Bone mineral and body composition measurements: cross-calibration of pencil-beam and fan-beam dual-energy X-ray absorptiometers. *J Bone Miner Res* 13(10):1613-8.

11. Franck H and Munz M (2000) Total body and regional bone mineral densitometry (BMD) and soft tissue measurements: correlations of BMD parameter to lumbar spine and hip. *Calcif Tissue Int* 67(2):111-5.

12. Fuchs RK, Bauer JJ, and Snow CM (2001) Jumping improves hip and lumbar spine bone mass in prepubescent children: a randomized controlled trial. *J Bone Miner Res* 16(1):148-56.

13. Griffiths MR, Noakes KA, and Pocock NA (1997) Correcting the magnification error of fan beam densitometers. *J Bone Miner Res* 12(1):119-23.

14. Hammami M, Koo MW, Koo WW, Thomas RT, and Rakhman D (2001) Regional bone mass measurement from whole-body dual energy X-ray absorptiometry scan. *J Clin Densitom* 4(2):131-6.

15. Koo WW, Hammami M, and Hockman EM (2002) Use of fan beam dual energy x-ray absorptiometry to measure body composition of piglets. *J Nutr* 132(6):1380-3.

16. Kröger H, Kotaniemi A, Vainio P, and Alhava E (1992) Bone densitometry of the spine and femur in children by dual-energy x-ray absorptiometry. *Bone Miner* 17(1):75-85.

17. Libouban H, Simon Y, Silve C, Legrand E, Baslé MF, Audran M, and Chappard D (2002) Comparison of pencil-, fan-, and cone-beam dual X-ray

absorptiometers for evaluation of bone mineral content in excised rat bone. *J Clin Densitom* 5(4):355-61.

18. MacKelvie KJ, McKay HA, Khan KM, and Crocker PR (2001) A school-based exercise intervention augments bone mineral accrual in early pubertal girls. *J Pediatr* 139(4):501-8.
19. McKay HA, Petit MA, Schutz RW, Prior JC, Barr SI, and Khan KM (2000) Augmented trochanteric bone mineral density after modified physical education classes: a randomized school-based exercise intervention study in prepubescent and early pubescent children. *J Pediatr* 136(2):156-62.
20. Morris FL, Naughton GA, Gibbs JL, Carlson JS, and Wark JD (1997) Prospective ten-month exercise intervention in premenarcheal girls: positive effects on bone and lean mass. *J Bone Miner Res* 12(9):1453-62.
21. Nickols-Richardson SM, O'Connor PJ, Shapses SA, and Lewis RD (1999) Longitudinal bone mineral density changes in female child artistic gymnasts. *J Bone Miner Res* 14(6):994-1002.
22. Petit MA, McKay HA, MacKelvie KJ, Heinonen A, Khan KM, and Beck TJ (2002) A randomized school-based jumping intervention confers site and maturity-specific benefits on bone structural properties in girls: a hip structural analysis study. *J Bone Miner Res* 17(3):363-72.
23. Pocock NA, Noakes KA, Majerovic Y, and Griffiths MR (1997) Magnification error of femoral geometry using fan beam densitometers. *Calcif Tissue Int* 60(1):8-10.
24. Ruetsche AG, Lippuner K, Jaeger P, and Casez JP (2000) Differences between dual X-ray absorptiometry using pencil beam and fan beam modes and their determinants in vivo and in vitro. *J Clin Densitom* 3(2):157-66.

25. Scerpella TA, Davenport M, Morganti CM, Kanaley JA, and Johnson LM (2003) Dose related association of impact activity and bone mineral density in pre-pubertal girls. *Calcif Tissue Int* 72(1):24-31.

26. Shypailo RJ, Posada JK, and Ellis KJ (1998) Whole-body phantoms with anthropomorphic-shaped skeletons for evaluation of dual-energy X-ray absorptiometry measurements. *Appl Radiat Isot* 49(5-6):503-5.

27. Tothill P and Hannan WJ (2000) Comparisons between Hologic QDR 1000W, QDR 4500A, and Lunar Expert dual-energy X-ray absorptiometry scanners used for measuring total body bone and soft tissue. *Ann NY Acad Sci* 904:63-71.

28. Tothill P, Hannan WJ, and Wilkinson S (2001) Comparisons between a pencil beam and two fan beam dual energy X-ray absorptiometers used for measuring total body bone and soft tissue. *Br J Radiol* 74(878):166-76.

29. Tylavsky F, Lohman T, Blunt BA, Schoeller DA, Fuerst T, Cauley JA, Nevitt MC, Visser M, and Harris TB (2003) QDR 4500A DXA overestimates fat-free mass compared with criterion methods. *J Appl Physiol* 94(3):959-65.

30. Visser M, Fuerst T, Lang T, Salamone L, and Harris TB (1999) Validity of fan-beam dual-energy X-ray absorptiometry for measuring fat-free mass and leg muscle mass. Health, Aging, and Body Composition Study--Dual-Energy X-ray Absorptiometry and Body Composition Working Group. *J Appl Physiol* 87(4):1513-20.

CHAPTER 3

DXA AND MICROCT PREDICT MATERIAL PROPERTIES IN VERTEBRAL CANCELLOUS BONE MORE ACCURATELY IN WOMEN THAN MEN[*]

Introduction

Although dual-energy X-ray absorptiometry (DXA) remains the standard for clinically assessing bone mass and predicting fracture risk, it does not fully explain the incidence of osteoporotic fractures. More than half of fragility fractures occur in women with a normal DXA T-score [38,51,58]. In addition, the vertebral fracture occurrence in patients receiving antiresorptive drugs dropped 15-60%, which was much more than the 4-16% predicted from the 0-8% increases in areal bone mineral density (aBMD) from DXA [8-11,50]. Therefore, DXA aBMD and T-score alone are insufficient to evaluate fracture risk accurately.

The strength of bone, and thus its resistance to fracture, is governed primarily by bone mass or density, architecture, and material properties [3,18,36,47,54]. Bone mass measured by DXA correlates variably with experimentally-measured bone mechanical properties, explaining 20-70% of the vertebral failure load *in vitro* and *in situ* [1,4,35,41,42]. For human cancellous bone, the explanatory power of a clinical bone density scan was 10-70% for apparent elastic modulus and ultimate stress and only 5% for ultimate strain [5,33].

---

[*] Cole JH, Myers ER, Wells MT, and van der Meulen MCH (2007) DXA and microCT predict material properties in vertebral cancellous bone more accurately in women than men. *In preparation.*

Three-dimensional measures of bone mass, such as bone volume fraction (BV/TV) and apparent density, correlate somewhat better with experimentally determined bone mechanical properties than the 2-D aBMD from DXA. Apparent density has been used to predict bone strength and apparent modulus using empirical formulations [3,17,25,48,49]. Regardless of the relationship used, apparent BMD and BV/TV acquired by experiments or micro-computed tomography (microCT) explained 60-85% of the variability in compressive elastic modulus and ultimate stress for human cancellous bone [29,31,33,40]. Similar to bone mass measures, architecture parameters have been experimentally correlated with elastic mechanical properties [7,19,20,27,43,55,57]. In sheep femoral bone assessed with microCT, the commonly assessed architecture indices of trabecular thickness, trabecular separation, and degree of anisotropy explained 20-70% of the variation in compressive ultimate strength [39].

Material properties also contribute to the overall structural behavior of bone and have been shown to vary with aging and disease. However, they have not been examined as fully as mass and architecture due to limitations with current imaging and testing techniques. Bone tissue material properties were altered in older patients with osteoporosis and often resulted in reduced mineral content and larger, more mature mineral crystals [15,21,37,45,46]. Changes in tissue properties with aging and disease, whether at the apparent or ultrastructure level, may compromise integrity of the bone structure, although the effect of such alterations on mechanical properties is not well understood, particularly for cancellous bone.

Because clinical DXA is used almost exclusively to diagnose and treat osteoporosis, understanding the extent that aBMD or T-score predicts bone strength, and particularly which components of strength, is important. Therefore, the principal objective of this study was to examine the ability of DXA T-score to predict bone mineral and microarchitecture measures from microCT and bone material properties from structural testing. Because the incidence of fragility fractures among the elderly is greater in women than in men [6,12,16], we also wanted to investigate possible sex differences in bone mass, architecture, and material properties with age. Therefore, the second objective of this study was to assess potential sex differences in age-related changes of bone architecture and material properties in cancellous bone. We chose to examine the thoracolumbar spine, not only for its abundance of cancellous bone but also for its susceptibility to age-related fractures. Vertebral cancellous bone contributes critically to skeletal load-bearing function [32,52]. For this study, we obtained cancellous bone specimens from the twelfth thoracic vertebra (T12) and the second lumbar vertebra (L2), a site used in clinical DXA scans to assess bone status. The lower thoracic and upper lumbar spine regions are common sites for fracture [2,13,26,60].

Methods

Subjects

Cadaver spine segments were obtained from 24 Caucasian donors (13 female, 11 male) aged 56-92 years. For 23 donors, the spine segment extended from the 11th thoracic vertebra (T11) through the 4th lumbar vertebra (L4), and for one donor, the segment extended from T11 through L2. Spines were excluded if any vertebra in the T11-L4 segment showed evidence of fracture in the DXA scan (1 female) or if the cancellous bone of the T12 or L2 vertebra showed evidence of bone metastasis during dissection (1 female, 1 male). To evaluate the relative value of different parameters in predicting cancellous bone mechanical properties, vertebral bone was characterized in each patient using several assessment tools, including clinical and laboratory methods at both the macroscopic and microscopic level, as outlined below (Figure 3.1).

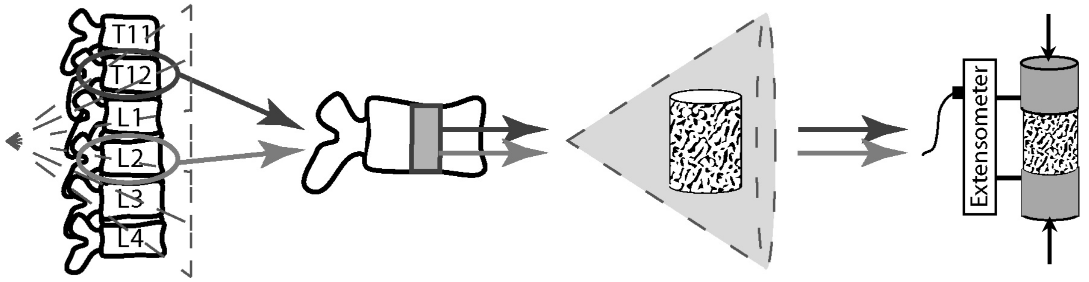

Clinical DXA
Imaged in saline bath

Dissection
T12, L2 vertebrae excised

MicroCT
Reconstructed and resampled to 17μm

Destructive Testing
Compressed at 0.5% ε/s

Figure 3.1. Human vertebral bone was assessed at the whole bone level using clinical dual-energy X-ray absorptiometry (DXA) and at the microstructural level using micro-computed tomography (microCT) and mechanical testing.

Clinical Bone Density Scan

Bone mineral status for all donors was assessed with clinical densitometry. To prepare for the bone density scan, the spine segments were thawed to remove the ribs, additional vertebral levels that were outside T11-L4, and any portions of the pelvis to allow the spine to rest in a flat position for the DXA scan. The spines were then refrozen. The frozen T11-L4 segments were secured in a curved Plexiglas® fixture, immersed in a saline bath within a Plexiglas® box, and scanned with a clinical fan-beam densitometer in lumbar spine array mode (Delphi QDR 4500A or QDR 4500W, Hologic Inc., Bedford, MA). Two scans were acquired for each spine: one for vertebral levels T11-L2 and one for levels L1-L4.

Clinical measurements of bone mineral were obtained from DXA scans. Bone projected area, bone mineral content (BMC), and aBMD were computed using standard manufacturer software for regions T11-L2 and L1-L4. In addition, the osteoporosis diagnostic index, T-score, was computed for L1-L4 of each donor.

Micro-Computed Tomography Scan

To prepare small cancellous specimens for microCT, the T12 and L2 vertebrae were excised from each spine segment, and a full-depth cylindrical specimen (diameter = 8.25 mm) was cut on the superior-inferior axis at low speed under continuous saline stream from the center of each vertebra using a metal bond diamond core drill (Starlight Industries, Rosemont, PA) in a drill press (Enco 105-1300, Fernley, NV, or Clarke BT1000, Perrysburgh, OH). Cored specimens were wrapped in saline-soaked gauze and stored frozen in sealed plastic bags.

To evaluate cancellous bone mass and architecture, cored vertebral specimens were analyzed using quantitative microCT (MS-8, GE Healthcare, London, Ontario, Canada). The specimens were scanned in a saline bath treated with a protease inhibitor cocktail to minimize protein degradation in the bone tissue (P8340, Sigma-Aldrich Inc., St. Louis, MO). Each scan contained a calibration phantom consisting of air, saline, and a bone mineral standard (SB3, Gammex RMI, Middleton, WI). The X-ray attenuations of these reference materials were used to calibrate the Hounsfield Unit (HU) scale by assuming that tissue mineral density was linearly related to grayscale values in HUs. The measured CT attenuation values were scaled to HUs using the air and water portions of the phantom, which have known values of -1000 and 0 HU, respectively. The resulting grayscale values in HUs were converted to tissue densities based on the density of the bone mineral standard (1.15 g/cc).

The specimens were scanned in two batches with different scanning parameters. The first batch (26 cores from 13 donors) was scanned individually at high X-ray energy (voltage = 70 kV_p, current = 90 μA) with 720 views, 8 frames per view, and a 3-second exposure time for a total scan time of approximately 8 hours. Data were reconstructed at an isotropic voxel resolution of 11.6 μm. The second batch (16 cores from 8 donors) was scanned two at a time at the same energy and exposure time with 400 views and 7 frames per view for a total scan time of approximately 4 hours. Data were reconstructed at an isotropic voxel resolution of 17.0 μm. For all cores, only an 8 mm section from the center of the core was reconstructed for analysis. After the microCT scans were completed, cancellous bone cores were wrapped in saline-soaked gauze and stored frozen in sealed plastic bags.

The reconstructed cancellous cores were reoriented to align the superior-inferior axis of the core with the vertical axis in the analysis software, and the ends of the cores were then cropped flat to a length of 7.5 mm (MicroView ABA 2.1.1., GE Healthcare, London, Ontario, Canada). MicroCT data were resampled at 17 μm to equilibrate voxel sizes between the two batch groups. For each core, bone voxels were distinguished from non-bone voxels (e.g., air, marrow, saline) using the Otsu method, which assumes a bimodal distribution of grayscale values and computes the bone threshold in HU by maximizing the between-class variance of two populations [44]. Because the use of a global threshold across specimens with dissimilar averages in mineral density may result in an inaccurate topology [14], a unique threshold was computed for each specimen.

Cancellous bone mass and architecture were assessed for each of the reoriented, cropped cores after thresholding using the following standard metrics: bone volume fraction (BV/TV), tissue bone mineral density (tisBMD), apparent bone mineral density (appBMD), direct trabecular thickness (Tb.Th*) [24], direct trabecular separation (Tb.Sp*) [24], mean intercept length in the principal material directions (MIL_1, MIL_2, MIL_3) [22,56,59], and degree of anisotropy (DA) [20]. MILs were computed using 200 random rotations of a test grid with a spacing of 0.136 mm (8 voxels), which is within the maximum grid spacing (0.2 mm) previously shown to be sufficient for calculating three-dimensional cancellous bone morphology [53]. DA was computed as the ratio of maximum to minimum MIL (MIL_1/MIL_3).

Structural Testing

Following the microCT scans, the cancellous bone cores were prepared for mechanical testing using a previously documented protocol designed to minimize end artifacts [28]. The cortical end plates were removed from each end of the thawed cancellous cores. With the specimens submerged in a water bath, the marrow was removed from the surface of each end using a water jet. Approximately one-fourth of the overall core length was cleaned at each end. The ends were further cleaned by briefly submerging them in ethyl alcohol and then dried using an air jet under low pressure. Snug-fitting brass caps were glued to the cleaned portion of each core end using an ethyl cyanoacrylate adhesive (Loctite® 401, Henkel Corporation, Rocky Hill, CT), such that the bone ends did not extend to the end of the brass caps. The end-caps were aligned with the longitudinal axis of the bone core using a machinist's universal V-block (Fisher Machine Products, Hawthorne, CA). The diameter of each cancellous core was recorded as the mean of six measurements, and the exposed length was defined as the mean of four measurements, using metric dial calipers. The central exposed section was wrapped with saline-soaked gauze and plastic wrap, and the capped cores were refrigerated for 24 hours to allow the adhesive to cure.

The mechanical properties of the cancellous bone cores were assessed through destructive uniaxial compression using a servohydraulic load frame (Mini-Bionix 858, MTS Systems Corporation, Eden Prairie, MN). The brass end-caps were secured in small three-jaw chucks. Displacement was measured with a 25-mm gage length axial extensometer (634.11F-24, MTS Systems Corporation, Eden Prairie, MN) attached to both end-caps. Elastic and failure properties measured with this technique have been validated with an extensometer attached to the bone surface [29]. The effective gage length was computed as the average of the total length and the exposed length of the bone core [28]. Bone specimens were preconditioned for 5 cycles between 0 and 0.10% compressive strain and then loaded monotonically at a rate of 0.50% strain per second to 3% compressive strain, which is well beyond reported failure strains for human cancellous bone [31,34]. Mechanical tests were conducted in displacement control at room temperature, and load and displacement data were sampled at 20 Hz.

Mechanical properties were computed from the destructive testing data. Load and displacement data were converted to apparent stress and strain using standard mechanics formulae [23]. Apparent elastic modulus was defined as the slope of a least-squares linear fit to the stress-strain data over 0.02-0.24% strain [31]. Due to the ambiguous border between elastic and plastic behavior regions, the yield point was defined as the stress corresponding to the intersection of the stress-stress curve with a line parallel to the initial slope of linear region but offset by 0.2% strain. The ultimate point was defined by the point of maximum stress.

Statistical Analysis

Age- and sex-related differences in cancellous bone parameters were assessed using a mixed linear model on age, sex, and the age-sex interaction, accounting for repeated measures over bone site (T12, L2). The correlation of clinical bone density scans with cancellous bone architecture and apparent-level material properties was assessed using Pearson's product-moment coefficients for DXA, microCT, and mechanical testing techniques (SAS 9.1, SAS Institute Inc., Cary, NC). Correlations were first analyzed with sex pooled to examine general trends between the assessment modalities and then separately for men and women to determine sex-related differences in these trends. A significance level of 0.05 was used for all analyses.

Results

Cancellous bone cylinders were taken from the T12 and L2 vertebrae of 10 male donors ages 56-79 (mean = 67.4 ± 6.9 years) and 11 female donors ages 58-92 (mean = 73.2 ± 11.8 years). The mean ages of males and females were not significantly different ($p = 0.192$). DXA T-score, computed over the L1-L4 vertebral levels, spanned the spectrum of diagnosis, from normal values of 0.2 in males and 0.5 in females to osteoporotic values of -2.9 for males and -5.2 for females (Figure 3.2).

Based on T-score, four subjects (2 males, 2 females) were categorized with normal bone mass, nine subjects (7 males, 2 females) had low bone mass, and eight subjects (1 male, 7 females) were osteoporotic. A linear model of age, sex, and their interaction, with repeated measures on bone site (T12, L2), was used to check for overall age-related sex differences in measured parameters. Metrics of bone mass, architecture, and material properties did not vary significantly with age or by sex, and the variation of the bone parameters with age did not differ significantly between males and females (Figure 3.3, Table 3.1).

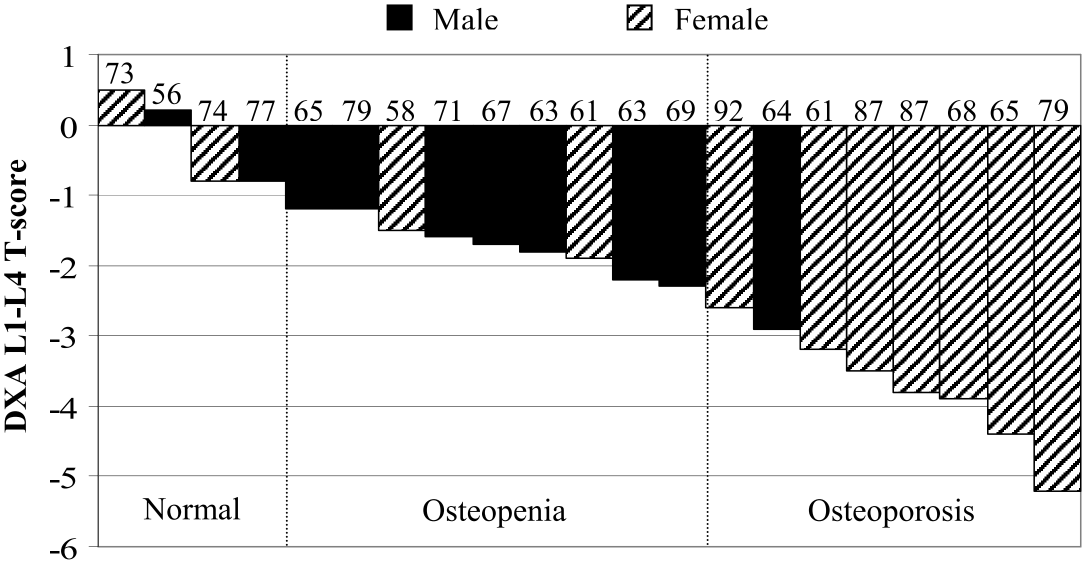

Figure 3.2. Distribution of DXA L1-L4 T-scores for male (n = 10) and female (n = 11) subjects. Age in years and regions of bone diagnosis are depicted on the plot.

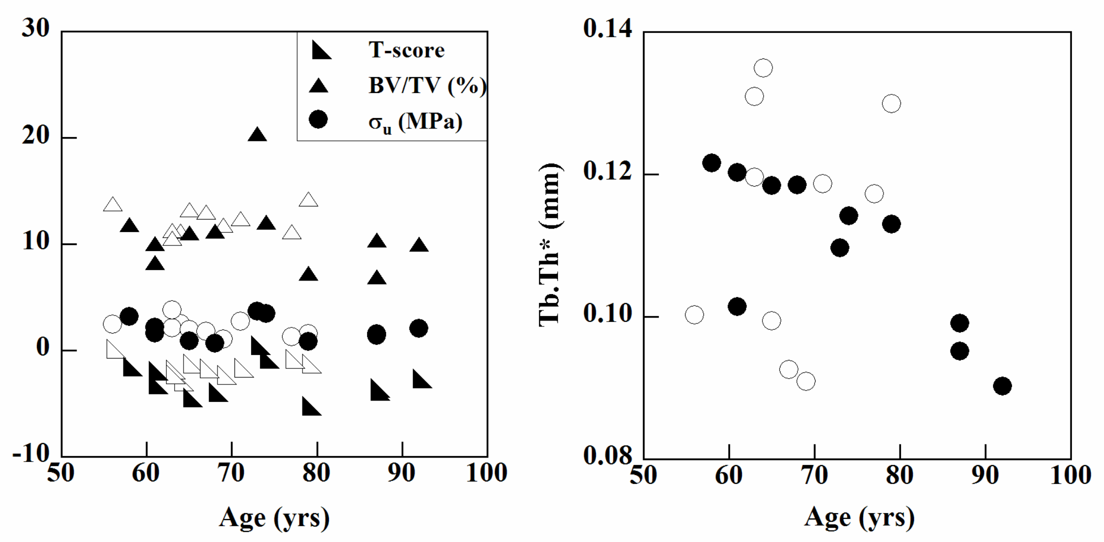

(a) (b)

Figure 3.3. Measures of (a) bone mass (e.g., T-score and bone volume fraction = BV/TV) and apparent material properties (e.g., ultimate stress = σ_u) and (b) bone architecture (e.g., mean direct trabecular thickness = Tb.Th*) did not differ significantly by age, sex, or the age * sex interaction. Males are depicted by open symbols and females by filled symbols.

Table 3.1. Mean measurements of bone mass, architecture, and material properties for the T12 and L2 vertebrae taken from male and female cadavers. Mean values for males and females were not significantly different (sex $p > 0.05$), and the variation with age was not significantly different by sex (interaction $p > 0.05$).

		Males (n = 10)				Females (n = 11)			
		T12		L2		T12		L2	
Parameter	Units	Mean	SD	Mean	SD	Mean	SD	Mean	SD
T-score[†]		---	---	-1.6	0.9	---	---	-2.8	1.7
aBMD	g/cm^2	0.805	0.135	0.912	0.091	0.582	0.143	0.745	0.221
BV/TV	%	11.9	2.5	12.3	1.3	10.5	3.3	10.9	3.6
tisBMD	g/cm^3	0.66	0.08	0.72	0.17	0.65	0.07	0.66	0.07
appBMD	g/cm^3	0.078	0.017	0.088	0.022	0.068	0.020	0.071	0.022
MIL_1	mm	0.21	0.02	0.22	0.03	0.21	0.03	0.21	0.02
MIL_2	mm	0.17	0.02	0.18	0.02	0.16	0.02	0.17	0.01
MIL_3	mm	0.16	0.02	0.15	0.01	0.14	0.02	0.16	0.01
DA		0.23	0.09	0.28	0.05	0.29	0.09	0.25	0.07
Tb.Th*	mm	0.11	0.02	0.11	0.02	0.11	0.01	0.11	0.01
Tb.Sp*	mm	1.33	0.17	1.30	0.18	1.35	0.16	1.36	0.15
Modulus	MPa	562	177	539	131	470	275	488	231
Yield stress	MPa	2.16	0.74	2.02	0.65	1.88	1.04	1.88	1.01
Ultimate stress	MPa	2.25	0.78	2.14	0.80	2.04	1.13	1.97	1.07
Yield strain	%	0.58	0.05	0.57	0.04	0.62	0.10	0.57	0.04
Ultimate strain	%	0.75	0.13	0.77	0.20	0.95	0.36	0.80	0.25

[†] T-score was computed over vertebral levels L1-L4.

Correlations with Sex Pooled

The correlative power of clinical DXA T-score with cancellous bone architecture, apparent material properties, and other measures of bone mass was investigated with Pearson's product-moment coefficients. When sex was pooled, T-score correlated moderately with apparent elastic modulus, yield stress, and ultimate stress at T12 (r = 0.72-0.74) and at L2 (r = 0.63-0.70, Table 3.2). T-score correlated with BV/TV and appBMD at T12 and L2 (r = 0.65-0.76) but not with tisBMD at either site. T-score did not correlate with yield strain, ultimate strain, or any cancellous bone architecture measure at either T12 or L2 when sex was pooled.

Three-dimensional measures of bone mass from microCT had similar relationships with apparent material properties as did T-score. BV/TV, tisBMD, and appBMD correlated somewhat with apparent elastic modulus, yield stress, and ultimate stress at T12 and L2 (r = 0.45-0.67, Table 3.3). None of the three density metrics correlated with yield strain or ultimate strain at either site. MicroCT bone density metrics also did not correlate with most measures of architectural orientation, although tisBMD correlated with MIL_1 and MIL_2 at T12, and appBMD correlated with MIL_2 and MIL_3 at T12 and with MIL_2 at L2. Tissue BMD also tended to correlate with MIL_1 and MIL_2 at L2, although these relationships were not significant (p = 0.052 and 0.064, respectively). In particular, microCT density did not correlate at all with degree of anisotropy, which is the most common parameter used to assess structural orientation. Interestingly, BV/TV correlated negatively with mean direct Tb.Sp* (T12 r = -0.68 and L2 r = -0.60), but tisBMD correlated positively with mean Tb.Sp* (T12 r = 0.70 and L2 r = 0.45). Besides tisBMD at T12, no bone density measure was related to direct Tb.Th* at either vertebral site.

Table 3.2. Pearson's product-moment coefficients (r) and associated p-values for correlations of T-score with measures of bone mass, architecture, and apparent material properties at both vertebral sites (T12, L2) with sex pooled. **p < 0.05 in bold**.

		Bone Mass			*Bone Architecture*						*Apparent Material Properties*				
		BV/TV	tis BMD	app BMD	Tb.Th*	Tb.Sp*	MIL_1	MIL_2	MIL_3	DA	E	σ_Y	σ_u	ε_Y	ε_u
T12	r	**0.65**	0.20	**0.70**	0.09	-0.34	0.23	0.27	0.33	-0.12	**0.74**	**0.74**	**0.72**	-0.06	-0.14
	p	**0.0014**	0.39	**0.0004**	0.71	0.13	0.31	0.23	0.14	0.60	**0.0001**	**0.0001**	**0.0002**	0.79	0.53
L2	r	**0.76**	0.16	**0.68**	0.02	-0.36	0.17	0.28	0.09	0.16	**0.70**	**0.64**	**0.63**	0.30	0.07
	p	**<0.0001**	0.48	**0.0008**	0.93	0.11	0.46	0.22	0.71	0.50	**0.0004**	**0.0016**	**0.0022**	0.19	0.75

Table 3.3. Pearson's product-moment coefficients (r) and associated p-values for correlations of microCT bone mass measures with apparent material properties at both vertebral sites (T12, L2) with sex pooled. **p < 0.05 in bold**.

			Bone Architecture						*Apparent Material Properties*				
			Tb.Th*	Tb.Sp*	MIL_1	MIL_2	MIL_3	DA	E	σ_Y	σ_u	ε_Y	ε_u
BV/TV	T12	r	0.11	**-0.68**	-0.01	0.27	0.35	-0.39	**0.59**	**0.52**	**0.53**	-0.30	-0.21
		p	0.62	**0.0007**	0.95	0.25	0.12	0.08	**0.0046**	**0.016**	**0.013**	0.19	0.37
	L2	r	0.07	**-0.60**	0.07	0.21	0.28	-0.20	**0.50**	**0.45**	**0.45**	0.04	0.22
		p	0.77	**0.0039**	0.77	0.36	0.22	0.39	**0.022**	**0.043**	**0.039**	0.88	0.34
tisBMD	T12	r	**0.52**	**0.70**	**0.80**	**0.57**	0.40	0.38	0.22	0.35	0.34	0.33	0.17
		p	**0.017**	**0.0005**	**<0.0001**	**0.0069**	0.071	0.092	0.34	0.12	0.13	0.14	0.45
	L2	r	0.36	**0.45**	0.43	0.41	0.18	0.37	0.40	0.42	0.39	0.42	-0.11
		p	0.10	**0.040**	0.052	0.064	0.45	0.10	0.074	0.056	0.079	0.057	0.64
appBMD	T12	r	0.34	-0.37	0.33	**0.53**	**0.52**	-0.23	**0.67**	**0.65**	**0.65**	-0.17	-0.14
		p	0.13	0.095	0.14	**0.014**	**0.015**	0.32	**0.0009**	**0.0016**	**0.0014**	0.47	0.54
	L2	r	0.31	-0.16	0.33	**0.44**	0.33	0.08	**0.62**	**0.60**	**0.58**	0.28	0.10
		p	0.17	0.49	0.14	**0.045**	0.14	0.74	**0.0027**	**0.0043**	**0.0055**	0.21	0.68

Correlations by Sex

When the correlations were performed separately by sex, marked differences in the relationship between bone assessment parameters emerged for males and females (Figure 3.4). For apparent material properties, T-score correlated well with elastic modulus, yield stress, and ultimate stress for females at both T12 and L2 (r = 0.74-0.95, Table 3.4) but only with elastic modulus at T12 for males (r = 0.74). T-score also correlated well with BV/TV and appBMD at both T12 and L2 (r = 0.71-0.90) but again only for females. For bone architecture, T-score only correlated with the L2 primary principal MIL (r = 0.66) for females but not for males. For females, T-score did not correlate with tisBMD, most architecture parameters (i.e., mean Tb.Th*, mean Tb.Sp*, MIL_2, MIL_3, DA), yield strain, or ultimate strain at either site. For males, DXA T- score did not correlate with cancellous bone density, bone architecture, or apparent material properties at either site, except for elastic modulus at T12.

Sex-specific trends were also found in the relationship of bone mass from 3-D microCT scans with bone architecture and apparent material properties. For apparent material properties, BV/TV and appBMD correlated with elastic modulus (L2 p = 0.05), yield stress, and ultimate stress in females at both sites (r = 0.60-0.90, Table 3.5) but not for males at either site. TisBMD did not correlate significantly with any apparent material property for males or females, except for T12 ultimate strain and nearly for T12 yield strain (p = 0.053) in males. For trabecular architecture, BV/TV was negatively correlated with mean Tb.Sp* at both sites for females (r = -0.74 to -0.77) and tended to be correlated for males at T12 (r = -0.63, p = 0.050). Tissue BMD at T12 correlated with mean Tb.Th*, mean Tb.Sp*, and two of the principal MILs for males (r = 0.76-0.90) and with MIL_1 and DA for females (r = 0.73-0.75). Apparent BMD was not correlated with any architecture measure for either males or females, although it tended to correlate with Tb.Sp* at L2 for women (r = -0.60, p = 0.051).

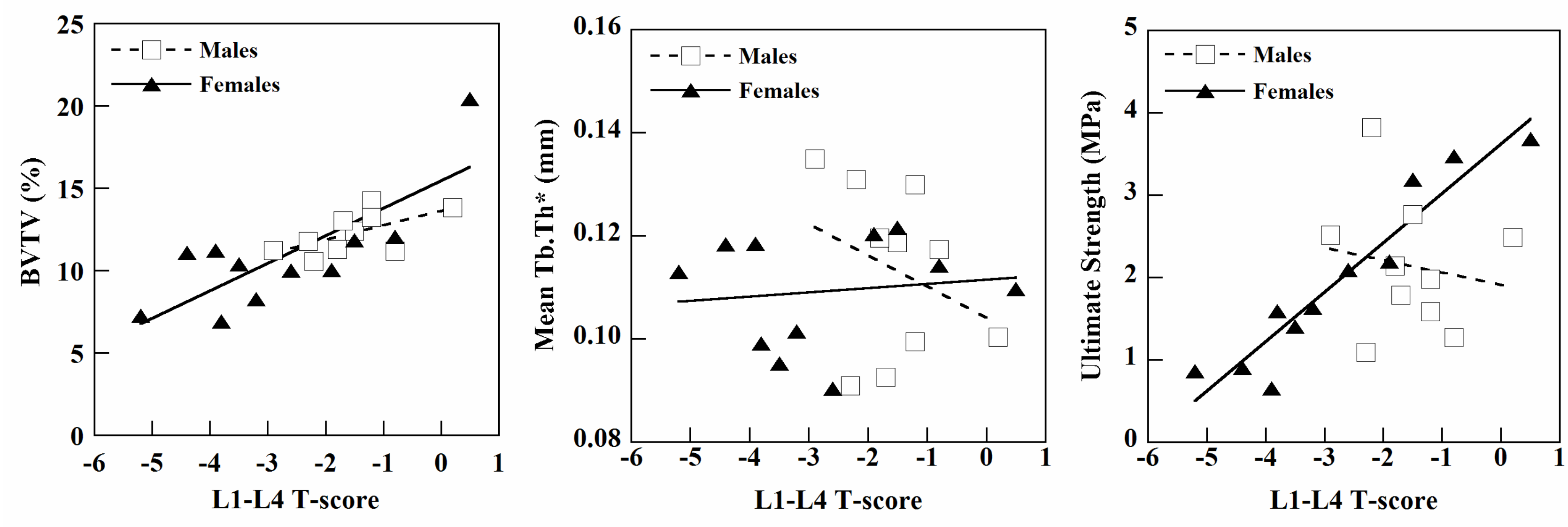

(a) (b) (c)

Figure 3.4. Linear correlations between measures of cancellous bone (a) mass (e.g., bone volume fraction = BV/TV), (b) architecture (e.g., mean direct trabecular thickness = Tb.Th*), and apparent material properties (e.g., ultimate stress = ultimate strength) differed significantly by sex.

Table 3.4. Pearson's product-moment coefficients (r) and associated p-values for correlations of T-score with measures of bone mass, architecture, and apparent material properties at both vertebral sites (T12, L2) by sex. **$p < 0.05$ in bold**.

		Bone Mass			*Bone Architecture*						*Apparent Material Properties*				
MALE		BV/ TV	tis BMD	app BMD	Tb.Th*	Tb.Sp*	MIL_1	MIL_2	MIL_3	DA	E	σ_Y	σ_u	ε_Y	ε_u
T12	r	0.45	-0.18	0.35	0.03	-0.37	-0.04	0.06	0.18	-0.28	**0.74**	0.57	0.51	-0.05	-0.38
	p	0.19	0.61	0.31	0.93	0.29	0.90	0.86	0.63	0.43	**0.014**	0.084	0.13	0.88	0.28
L2	r	0.61	-0.15	0.09	-0.32	-0.54	-0.59	-0.13	-0.38	-0.53	-0.16	-0.21	-0.17	-0.18	0.13
	p	0.062	0.68	0.81	0.36	0.11	0.072	0.72	0.28	0.12	0.66	0.56	0.63	0.61	0.72
FEMALE															
T12	r	**0.71**	0.36	**0.83**	-0.02	-0.36	0.35	0.26	0.25	0.16	**0.74**	**0.81**	**0.83**	0.05	0.07
	p	**0.015**	0.27	**0.0018**	0.94	0.27	0.29	0.44	0.46	0.63	**0.0090**	**0.0024**	**0.0015**	0.88	0.83
L2	r	**0.78**	0.40	**0.90**	0.12	-0.24	**0.66**	0.51	0.36	0.26	**0.94**	**0.94**	**0.95**	0.56	0.12
	p	**0.0048**	0.22	**0.0002**	0.72	0.48	**0.027**	0.11	0.27	0.43	**<.0001**	**<.0001**	**<.0001**	0.071	0.73

Table 3.5. Pearson's product-moment coefficients (r) and associated p-values for correlations of microCT bone mass measures with apparent material properties at both vertebral sites (T12, L2) by sex. **$p < 0.05$ in bold**.

			Bone Architecture						*Apparent Material Properties*				
MALE			Tb.Th*	Tb.Sp*	MIL_1	MIL_2	MIL_3	DA	E	σ_Y	σ_u	ε_Y	ε_u
BV/TV	T12	r	0.01	-0.63	-0.19	0.07	0.15	-0.39	0.17	0.02	-0.00	-0.42	-0.40
		p	0.97	0.050	0.61	0.84	0.68	0.26	0.64	0.96	1.0	0.23	0.25
	L2	r	-0.37	-0.44	-0.44	-0.17	-0.32	-0.30	-0.14	-0.30	-0.30	-0.55	-0.09
		p	0.29	0.21	0.21	0.65	0.36	0.39	0.70	0.40	0.40	0.098	0.81
tisBMD	T12	r	**0.78**	**0.90**	**0.88**	**0.76**	0.60	0.16	0.02	0.26	0.30	0.63	**0.67**
		p	**0.0083**	**0.0004**	**0.0008**	**0.010**	0.069	0.67	0.96	0.48	0.41	0.053	**0.033**
	L2	r	0.51	0.54	0.38	0.42	0.30	0.31	0.44	0.48	0.41	0.49	0.06
		p	0.13	0.11	0.28	0.22	0.40	0.39	0.20	0.16	0.23	0.15	0.88
appBMD	T12	r	0.41	-0.14	0.31	0.50	0.47	-0.28	0.18	0.17	0.18	-0.04	-0.01
		p	0.23	0.70	0.38	0.14	0.17	0.43	0.62	0.63	0.63	0.92	0.99
	L2	r	0.36	0.35	0.19	0.35	0.16	0.17	0.36	0.33	0.27	0.24	-0.01
		p	0.31	0.31	0.59	0.32	0.65	0.64	0.31	0.35	0.46	0.50	0.99
FEMALE													
BV/TV	T12	r	0.14	**-0.74**	0.07	0.34	0.44	-0.31	**0.76**	**0.74**	**0.77**	-0.22	-0.08
		p	0.67	**0.0092**	0.84	0.31	0.18	0.35	**0.0071**	**0.0090**	**0.0052**	0.52	0.82
	L2	r	0.23	**-0.77**	0.27	0.37	0.54	-0.28	0.60	**0.60**	**0.65**	0.21	0.36
		p	0.51	**0.0053**	0.42	0.26	0.083	0.41	0.052	**0.049**	**0.031**	0.54	0.28
tisBMD	T12	r	0.08	0.50	**0.75**	0.33	0.12	**0.73**	0.34	0.41	0.38	0.29	0.11
		p	0.81	0.11	**0.0080**	0.32	0.72	**0.011**	0.31	0.21	0.26	0.39	0.76
	L2	r	-0.23	0.58	0.57	0.36	-0.01	0.57	0.57	0.59	0.53	0.57	-0.44
		p	0.50	0.062	0.068	0.28	0.98	0.070	0.065	0.058	0.095	0.068	0.18
appBMD	T12	r	0.20	-0.57	0.35	0.48	0.48	-0.04	**0.89**	**0.89**	**0.90**	-0.15	-0.06
		p	0.56	0.070	0.29	0.13	0.13	0.91	**0.0002**	**0.0003**	**0.0001**	0.67	0.85
	L2	r	0.18	-0.60	0.46	0.51	0.57	-0.12	**0.78**	**0.79**	**0.82**	0.39	0.24
		p	0.59	0.051	0.15	0.11	0.066	0.73	**0.0045**	**0.0037**	**0.0022**	0.24	0.49

Discussion

Cancellous bone mass, architecture, and material properties did not correlate with age or sex, indicating that bone strength cannot be predicted based on these factors alone. DXA T-score, the primary clinical metric used to characterize bone mass and to predict skeletal fracture, correlated with some apparent material properties and three-dimensional measures of bone mass from microCT, but it did so almost solely for females. For females, decreasing bone mass measured by DXA was moderately to strongly associated with decreasing bone volume fraction and apparent density, and with reduced apparent material properties, in both the thoracic and lumbar spine. Therefore, DXA would more accurately predict both mineral mass and material properties in vertebral cancellous bone for females than for males and may therefore provide a more accurate assessment of fracture risk in that population.

For the most part, DXA failed to predict parameters of bone microarchitecture regardless of sex. Interestingly, microCT volume fraction and apparent density were, in general, also poor predictors of architecture, although these measures did relate well with trabecular separation in females. However, when using tissue density, microCT was strongly associated with most of the architecture parameters studied, at least for females, including measures describing the trabecular structure, orientation, and degree of anisotropy. To date, most studies have used BV/TV and apparent density to assess cancellous bone integrity. Our data suggest that, while these factors may assess apparent material properties well, tissue density may be a better measure for evaluating the tissue architecture in female subjects.

DXA is a large-scale, two-dimensional technique and only provides projected estimates of bone mineral density. MicroCT provides a localized three-dimensional assessment of bone mineral mass and density and thus is assumed to provide a better characterization of cancellous bone tissue. In addition, the same core of cancellous bone for was used for microCT scans and mechanical testing and thus should provide a more direct comparison of measurements obtained from both. However, at least for female subjects, microCT measurements related no better to apparent material properties than did DXA T-score, with correlation coefficients of 0.74-0.95 for DXA and 0.60-0.90 for microCT BV/TV and apparent density. Both techniques were equally unrelated to apparent properties for male subjects. On the other hand, microCT did provide a better assessment of cancellous bone architecture than did DXA. While T-score correlated with almost none of the architecture parameters studied, microCT measures correlated strongly with metrics of cancellous bone structure and orientation in the males and of structure, primary orientation, and degree of anisotropy in females, mostly in the thoracic spine for both.

Mostly, both DXA and microCT measures of bone mass could not predict yield or ultimate strain for males or females at either site. Strain measures are important for characterizing tissue failure [30] and may provide more information not captured by clinical bone density measures, cancellous architecture measures, or even other apparent material properties. Similarly, the degree of anisotropy in the trabecular structure was generally not associated with either DXA or microCT bone mass and thus may also contribute additional information about bone strength. Interestingly, both apparent strains and degree of anisotropy were correlated with tissue density in the thoracic spine, although only for one of the sexes in each case.

Although the mean L1-L4 T-score was lower in females than males for this study (-2.8 and -1.6, respectively), the difference was not significant due to a large variability across subjects for both groups. However, when T-score was divided into the diagnostic categories of normal, low, and osteoporotic bone mass, the distribution of males and females in each group differed (Figure 3.2). Interestingly, males were primarily clustered centrally within the osteopenic group, between T-scores of -1.2 and -2.3. Two male subjects were in the normal range, and only one was in the osteoporotic range, and he was near the top end of the range. Conversely, two females fell within the normal range, only two were in the mid-range of low bone mass, and the remaining 7 were concentrated in the osteoporotic group. The analyses in this study were based on the continuous measure T-score and thus should apply regardless of the diagnostic category or the distribution within each category. Nevertheless, the sex-specific T-score distributions support the hypothesis that the mechanism of age-related bone loss is fundamentally different for men and women.

In conclusion, our data showed that clinical DXA spine measurements correlated with high-resolution microCT volume fraction and apparent density in the vertebral cancellous bone of female subjects but not for male subjects. In addition, DXA and microCT mass measurements were strongly related to most of the apparent material properties in females but not for males. Therefore, both DXA and microCT predicted apparent material properties more accurately for women than for men in cancellous bone of the thoracic and lumbar spine. For female subjects, DXA T-score correlated with apparent modulus and strength as strongly as the microCT mass measures did, but it could not account for the observed variations in trabecular architecture. MicroCT mass measures, on the other hand, correlated well with architecture measures, particularly in the thoracic spine of both males and females. Specifically, microCT tissue density was related to degree of anisotropy in the thoracic bone of females, as well as to apparent tissue strains in the thoracic bone of males, both of which were not explained by any other parameter. Therefore, use of microCT scans would improve the assessment of bone strength in the thoracic spine of both males and females. In fact, they provided an overall better assessment than did DXA for all of the determinants of bone strength and ideally could replace the DXA scan altogether if non-invasive measurements could be made accurately and affordably.

References

1. Bjarnason K, Hassager C, Svendsen OL, Stang H, and Christiansen C (1996) Anteroposterior and lateral spinal DXA for the assessment of vertebral body strength: comparison with hip and forearm measurement. *Osteoporos Int* 6(1):37-42.
2. Black DM, Cummings SR, Stone K, Hudes E, Palermo L, and Steiger P (1991) A new approach to defining normal vertebral dimensions. *J Bone Miner Res* 6(8):883-92.
3. Carter DR and Hayes WC (1977) The compressive behavior of bone as a two-phase porous structure. *J Bone Joint Surg Am* 59-A:954-962.
4. Cheng XG, Nicholson PH, Boonen S, Lowet G, Brys P, Aerssens J, van der Perre G, and Dequeker J (1997) Prediction of vertebral strength in vitro by spinal bone densitometry and calcaneal ultrasound. *J Bone Miner Res* 12(10):1721-8.
5. Cody DD, McCubbrey DA, Divine GW, Gross GJ, and Goldstein SA (1996) Predictive value of proximal femoral bone densitometry in determining local orthogonal material properties. *J Biomech* 29(6):753-61.
6. Cooper C, Campion G, and Melton LJ, 3rd (1992) Hip fractures in the elderly: a world-wide projection. *Osteoporos Int* 2(6):285-9.
7. Cowin SC (1985) The relationship between the elasticity tensor and the fabric tensor. *Mechanics of Materials* 4:137-147.
8. Cranney A, Tugwell P, Adachi J, Weaver B, Zytaruk N, Papaioannou A, Robinson V, Shea B, Wells G, and Guyatt G (2002) Meta-analyses of therapies for postmenopausal osteoporosis. III. Meta-analysis of risedronate for the treatment of postmenopausal osteoporosis. *Endocr Rev* 23(4):517-23.

9. Cranney A, Tugwell P, Zytaruk N, Robinson V, Weaver B, Adachi J, Wells G, Shea B, and Guyatt G (2002) Meta-analyses of therapies for postmenopausal osteoporosis. IV. Meta-analysis of raloxifene for the prevention and treatment of postmenopausal osteoporosis. *Endocr Rev* 23(4):524-8.
10. Cranney A, Wells G, Willan A, Griffith L, Zytaruk N, Robinson V, Black D, Adachi J, Shea B, Tugwell P, and Guyatt G (2002) Meta-analyses of therapies for postmenopausal osteoporosis. II. Meta-analysis of alendronate for the treatment of postmenopausal women. *Endocr Rev* 23(4):508-16.
11. Cummings SR, Karpf DB, Harris F, Genant HK, Ensrud K, LaCroix AZ, and Black DM (2002) Improvement in spine bone density and reduction in risk of vertebral fractures during treatment with antiresorptive drugs. *Am J Med* 112(4):281-9.
12. Cummings SR and Melton LJ (2002) Epidemiology and outcomes of osteoporotic fractures. *Lancet* 359(9319):1761-7.
13. Evans SF and Davie MW (2000) Vertebral fractures and bone mineral density in idiopathic, secondary and corticosteroid associated osteoporosis in men. *Ann Rheum Dis* 59(4):269-75.
14. Feldkamp LA, Goldstein SA, Parfitt AM, Jesion G, and Kleerekoper M (1989) The direct examination of three-dimensional bone architecture in vitro by computed tomography. *J Bone Miner Res* 4(1):3-11.
15. Gadeleta SJ, Boskey AL, Paschalis E, Carlson C, Menschik F, Baldini T, Peterson M, and Rimnac CM (2000) A physical, chemical, and mechanical study of lumbar vertebrae from normal, ovariectomized, and nandrolone decanoate-treated cynomolgus monkeys (Macaca fascicularis). *Bone* 27(4):541-50.

16. Gallagher JC, Melton LJ, Riggs BL, and Bergstrath E (1980) Epidemiology of fractures of the proximal femur in Rochester, Minnesota. *Clin Orthop Relat Res* (150):163-71.

17. Gibson LJ (1985) The mechanical behavior of cancellous bone. *J Biomech* 18:317-328.

18. Goldstein SA (1987) The mechanical properties of trabecular bone: dependence on anatomic location and function. *J Biomech* 20(11-12):1055-61.

19. Goldstein SA, Goulet R, and McCubbrey D (1993) Measurement and significance of three-dimensional architecture to the mechanical integrity of trabecular bone. *Calcif Tissue Int* 53:S127-32; discussion S132-3.

20. Goulet RW, Goldstein SA, Ciarelli MJ, Kuhn JL, Brown MB, and Feldkamp LA (1994) The relationship between the structural and orthogonal compressive properties of trabecular bone. *J Biomech* 27(4):375-89.

21. Grynpas M (1993) Age and disease-related changes in the mineral of bone. *Calcif Tissue Int* 53 Suppl 1:S57-64.

22. Harrigan TP and Mann RW (1984) Characterization of microstructural anisotropy in orthotropic materials using a second rank tensor. *J Mater Sci* 19:761-767.

23. Hibbeler RC. Mechanics of Materials. Upper Saddle River, New Jersey: Prentice Hall, 1997.

24. Hildebrand T and Rüegsegger P (1997) A new method for the model-independent assessment of thickness in three-dimensional images. *J Microsc* 185:67-75.

25. Hodgskinson R and Currey JD (1992) Young's modulus, density and material properties in cancellous bone over a large density range. *J Mater Sci Mater Med* 3(377-381)

26. Johansson C, Mellstrom D, Rosengren K, and Rundgren A (1994) A community-based population study of vertebral fractures in 85-year-old men and women. *Age Ageing* 23(5):388-92.

27. Kabel J, Odgaard A, van Rietbergen B, and Huiskes R (1999) Connectivity and the elastic properties of cancellous bone. *Bone* 24(2):115-120.

28. Keaveny TM, Guo XE, Wachtel EF, McMahon TA, and Hayes WC (1994) Trabecular bone exhibits fully linear elastic behavior and yields at low strains. *J Biomech* 27:1127-1136.

29. Keaveny TM, Pinilla TP, Crawford RP, Kopperdahl DL, and Lou A (1997) Systematic and random errors in compression testing of trabecular bone. *J Orthop Res* 15(1):101-10.

30. Keaveny TM, Wachtel EF, Ford CM, and Hayes WC (1994) Differences between the tensile and compressive strengths of bovine tibial trabecular bone depend on modulus. *J Biomech* 27(9):1137-46.

31. Kopperdahl DL and Keaveny TM (1998) Yield strain behavior of trabecular bone. *J Biomech* 31(7):601-8.

32. Liebschner MA, Kopperdahl DL, Rosenberg WS, and Keaveny TM (2003) Finite element modeling of the human thoracolumbar spine. *Spine* 28(6):559-65.

33. Linde F, Gøthgen CB, Hvid I, and Pongsoipetch B (1988) Mechanical properties of trabecular bone by a non-destructive compression testing approach. *Eng Med* 17(1):23-9.

34. Linde F, Hvid I, and Pongsoipetch B (1989) Energy absorptive properties of human trabecular bone specimens during axial compression. *J Orthop Res* 7(3):432-9.

35. Lochmüller EM, Eckstein F, Kaiser D, Zeller JB, Landgraf J, Putz R, and Steldinger R (1998) Prediction of vertebral failure loads from spinal and femoral

dual-energy X-ray absorptiometry, and calcaneal ultrasound: an in situ analysis with intact soft tissues. *Bone* 23(5):417-24.

36. Martin RB, Burr DB, and Sharkey NA. Skeletal Tissue Mechanics. New York: Springer, 1998.

37. Miller LM, Tibrewala J, and Carlson CS (2000) Examination of bone chemical composition in osteoporosis using fluorescence-assisted synchrotron infrared microspectroscopy. *Cell Mol Biol (Noisy-le-grand)* 46(6):1035-44.

38. Miller PD, Siris ES, Barrett-Connor E, Faulkner KG, Wehren LE, Abbott TA, Chen YT, Berger ML, Santora AC, and Sherwood LM (2002) Prediction of fracture risk in postmenopausal white women with peripheral bone densitometry: evidence from the National Osteoporosis Risk Assessment. *J Bone Miner Res* 17(12):2222-30.

39. Mittra E, Rubin C, and Qin YX (2005) Interrelationship of trabecular mechanical and microstructural properties in sheep trabecular bone. *J Biomech* 38(6):1229-37.

40. Morgan EF, Bayraktar HH, and Keaveny TM (2003) Trabecular bone modulus-density relationships depend on anatomic site. *J Biomech* 36(7):897-904.

41. Moro M, Hecker AT, Bouxsein ML, and Myers ER (1995) Failure load of thoracic vertebrae correlates with lumbar bone mineral density measured by DXA. *Calcif Tissue Int* 56(3):206-9.

42. Myers ER, Yano KA, Moro M, Silva MJ, and Hayes WC (1996) Lumbar bone mineral density predicts thoracolumbar failure load in compression and flexion. *Trans Orthop Res Soc* 21:645.

43. Odgaard A, Kabel J, van Rietbergen B, Dalstra M, and Huiskes R (1997) Fabric and elastic principal directions of cancellous bone are closely related. *J Biomech* 30(5):487-495.

44. Otsu N (1979) Threshold Selection Method from Gray-Level Histograms. *IEEE T Syst Man Cyb* 9(1):62-66.

45. Paschalis EP, Betts F, DiCarlo E, Mendelsohn R, and Boskey AL (1997) FTIR microspectroscopic analysis of human iliac crest biopsies from untreated osteoporotic bone. *Calcif Tissue Int* 61(6):487-92.

46. Paschalis EP, Betts F, DiCarlo E, Mendelsohn R, and Boskey AL (1997) FTIR microspectroscopic analysis of normal human cortical and trabecular bone. *Calcif Tissue Int* 61(6):480-6.

47. Raux P, Townsend PR, Miegel R, Rose RM, and Radin EL (1975) Trabecular architecture of the human patella. *J Biomech* 8(1):1-7.

48. Rho JY, Ashman RB, and Turner CH (1993) Young's modulus of trabecular and cortical bone material: ultrasonic and microtensile measurements. *J Biomech* 26(2):111-119.

49. Rice JC, Cowin SC, and Bowman JA (1988) On the dependence of the elasticity and strength of cancellous bone on apparent density. *J Biomech* 21(2):155-68.

50. Sarkar S, Mitlak BH, Wong M, Stock JL, Black DM, and Harper KD (2002) Relationships between bone mineral density and incident vertebral fracture risk with raloxifene therapy. *J Bone Miner Res* 17(1):1-10.

51. Schuit SC, van der Klift M, Weel AE, de Laet CE, Burger H, Seeman E, Hofman A, Uitterlinden AG, van Leeuwen JP, and Pols HA (2004) Fracture incidence and association with bone mineral density in elderly men and women: the Rotterdam Study. *Bone* 34(1):195-202.

52. Silva MJ and Gibson LJ (1997) Modeling the mechanical behavior of vertebral trabecular bone: effects of age-related changes in microstructure. *Bone* 21(2):191-9.

53. Simmons CA and Hipp JA (1997) Method-based differences in the automated analysis of the three-dimensional morphology of trabecular bone. *J Bone Miner Res* 12(6):942-7.

54. Townsend PR, Raux P, Rose RM, Miegel RE, and Radin EL (1975) The distribution and anisotropy of the stiffness of cancellous bone in the human patella. *J Biomech* 8(6):363-7.

55. Ulrich D, Hildebrand T, van Rietbergen B, Müller R, and Rüegsegger P (1997) The quality of trabecular bone evaluated with micro-computed tomography, FEA and mechanical testing. *Stud Health Technol Inform* 40:97-112.

56. Underwood EE. Quantitative Stereology. Reading, MA: Addison-Wesley, 1970.

57. van Rietbergen B, Majumdar S, Pistoia W, Newitt DC, Kothari M, Laib A, and Rüegsegger P (1998) Assessment of cancellous bone mechanical properties from micro-FE models based on micro-CT, pQCT and MR images. *Technol Health Care* 6(5-6):413-20.

58. Wainwright S, Phipps KR, Stone JV, Cauley JA, Vogt MT, Black DM, and Orwall ES (2001) A large proportion of fractures in postmenopausal women occur with baseline bone mineral density T-score > -2.5. *J Bone Miner Res* 16:S155.

59. Whitehouse WJ (1974) The quantitative morphology of anisotropic trabecular bone. *J Microsc* 101:153-268.

60. Wu CY, Li J, Jergas M, and Genant HK (1995) Comparison of semiquantitative and quantitative techniques for the assessment of prevalent and incident vertebral fractures. *Osteoporos Int* 5(5):354-70.

CHAPTER 4

THE EFFECTS OF TRABECULAR TISSUE HETEROGENEITY ON THE MECHANICAL PERFORMANCE OF HUMAN VERTEBRAL CANCELLOUS BONE[*]

Introduction

The structural integrity of cancellous bone, which is essential to skeletal load-bearing capacity, is governed chiefly by bone mass or apparent density, trabecular architecture, and tissue material properties [4,9,29,38,42]. Although the impact of apparent density and architecture on bone structural behavior has been well-documented, much less is known about the influence of tissue material properties. Bone tissue is innately heterogeneous, exhibiting substantial spatial variation in tissue mineral content and quality [2,31,36,37]. A skeletal disorder characterized by low bone mass, osteoporosis alters bone tissue properties, as generally evidenced by altered mineralization and changes in chemical composition [8,11,30,35]. These changes in tissue properties may compromise the structural performance of bone, although the effect of tissue mineralization and composition on mechanical properties is not well understood, particularly for cancellous bone.

Tissue properties are difficult to characterize experimentally and are only examined over a small bone volume that likely does not fully capture the spatial

---

[*] Cole JH, Myers ER, and van der Meulen MCH (2007) The effects of trabecular tissue heterogeneity on the mechanical performance of human vertebral cancellous bone. *In preparation.*

variability. Computer models that simulate a virtual biopsy of cancellous bone can be used to investigate the mechanical behavior of a much larger region of bone and provide the opportunity to analyze that behavior non-invasively over changes in structural and material parameters. Early finite element (FE) models treated cancellous bone as an irregular lattice-type structure and were used to assess the effect of idealized changes in architecture but not tissue properties [1,12,19,41,50]. Architecture-based models, developed by converting voxels from a high-resolution micro-computed tomography (microCT) scan into cubic finite elements, more closely mimic the bone structure with fewer geometric assumptions than in the lattice models [6]. To date, these voxel-based models have primarily been used to examine the role of architecture in cancellous bone structural behavior, and most have assumed isotropic and homogeneous material properties [15,17,20,21,28,32,33,43,47-49].

Recently, several studies have begun to incorporate tissue heterogeneity into FE models, but most analyses assumed a spatial distribution extrapolated from localized tissue measurements [18,44]. Increasing spatial variability in cancellous bone tissue modulus by 20-50% reduced the apparent stiffness by 7-24% and greatly increased the percentage of failed tissue computed by comparing element strains to tissue yield strain [18]. The mineral distribution implemented in the models had a variable effect on the apparent stiffness, depending substantially on the modulus-density relationship used. Using FE models that mimicked a realistic *in vivo* mineral distribution, apparent stiffness decreased up to 4% with a linear relationship and increased up to 20% with a cubic relationship [44]. However, these studies only examined a small volume of cancellous bone (4-5 mm cubic regions) for a small number of samples (n = 3), and the findings depended on the assumed mineral distribution.

For a given volume of cancellous bone, microCT scans provide an accurate representation of tissue mineral distribution [16] that can be readily converted into a tissue modulus distribution using experimentally derived empirical relationships [4,10,14,40]. In a study using CT-derived tissue modulus distributions, architecture-based FE models more accurately predicted mechanical behavior than models using a homogeneous modulus [3]. Specifically, adding the tissue heterogeneity to models of rabbit cancellous bone increased the ability to predict experimental apparent modulus from 75% to 88%. Understanding the effect of bone tissue heterogeneity appears essential, therefore, to the accurate prediction of cancellous bone mechanical performance, at least for rabbit cancellous bone.

The effect of tissue property variations on structural performance needs to be examined for human cancellous bone, as does the influence of sex and metabolic disorders such as osteoporosis. The objectives of this study were 1) to simulate the structural behavior of cancellous bone in the human spine using specimen-specific architecture- and material-based computer models, 2) to assess the effects of varied material models on the mechanical performance of the bone structure, 3) to compare model-derived parameters to the compressive mechanical properties of the cancellous specimens, and 4) to determine the role of sex and clinical bone status in both the mechanical properties and the choice of material properties for computer modeling. Our approach was to model the architecture and material variations of human vertebral cancellous bone based on microCT scans and to compare the model predictions for different material distributions to experimentally measured mechanical properties of the same specimens.

Methods

Subjects

Cadaver spine segments were obtained from 24 Caucasian donors (13 female, 11 male) aged 56-92 years. For 23 donors, the spine segment extended from the 11th thoracic vertebra (T11) through the 4th lumbar vertebra (L4), and for one donor, the segment extended from T11 through the 2nd lumbar vertebra (L2). Spines were excluded if any vertebra in the L1-L4 segment showed evidence of fracture in a clinical bone density scan (1 female) or if the cancellous bone of the L2 vertebra showed evidence of bone metastasis during dissection (1 female, 1 male). A total of 21 subjects were included in the study.

Clinical Bone Density Scan

Clinical bone mineral status was assessed for all donors with dual-energy X-ray absorptiometry (DXA). T11-L4 spine segments were secured in a curved Plexiglas® fixture, immersed in a saline bath within a Plexiglas® box, and scanned with a clinical fan-beam densitometer in lumbar spine array mode (Delphi QDR 4500A or QDR 4500W, Hologic Inc., Bedford, MA). The osteoporosis diagnostic index, T-score, was computed for the L1-L4 subregion of each spine as the ratio of areal bone mineral density of the subject to the areal density of a sex- and race-matched young population with normal bone. Subjects were classified by T-score according to the World Health Organization guidelines, as follows [22]: Normal = T-score > -1.0; Osteopenia = -2.5 < T-score ≤ -1.0; and Osteoporosis = T-score ≤ -2.5.

Micro-Computed Tomography Scan

To prepare a small cancellous specimen for microCT, the L2 vertebra was excised from each spine segment, and a full-depth cylindrical specimen (diameter =

8.25 mm) was cut on the superior-inferior axis at low speed under continuous saline stream from the center of the vertebra using a metal bond diamond core drill (Starlight Industries, Rosemont, PA) in a drill press (Enco 105-1300, Fernley, NV, or Clarke BT1000, Perrysburgh, OH). Cored specimens were wrapped in saline-soaked gauze and stored frozen in sealed plastic bags.

To obtain a voxel-based characterization of cancellous bone structure and tissue mineral density, cored vertebral specimens were analyzed using quantitative microCT (MS-8, GE Healthcare, London, Ontario, Canada). The specimens were scanned in a saline bath treated with a protease inhibitor cocktail to minimize protein degradation in the bone tissue (P8340, Sigma-Aldrich Inc., St. Louis, MO). Each scan contained a calibration phantom consisting of air, saline, and a bone mineral standard (SB3, Gammex RMI, Middleton, WI). The X-ray attenuations of these reference materials were used to calibrate the Hounsfield Unit (HU) scale by assuming that tissue mineral density was linearly related to grayscale values in HUs. The measured CT attenuation values were scaled to HUs using the air and water portions of the phantom, which have known values of -1000 and 0 HU, respectively. The resulting grayscale values in HUs were converted to tissue densities based on the density of the bone mineral standard (1.15 g/cc).

The specimens were scanned in two batches with different scanning parameters. The first batch (13 cores from 13 donors) was scanned individually at high X-ray energy (voltage = 70 kV_p, current = 90 μA) with 720 views, 8 frames per view, and a 3-second exposure time for a total scan time of approximately 8 hours. Data were reconstructed at an isotropic voxel resolution of 11.6μm. The second batch (8 cores from 8 donors) was scanned two at a time at the same energy and exposure time with 400 views and 7 frames per view for a total scan time of approximately 4 hours. Data were reconstructed at an isotropic voxel resolution of 17.0 μm. For all cores, only an 8 mm section from the center of the core was reconstructed for analysis (Figure 4.1). After the microCT scans were completed, cancellous bone cores were wrapped in saline-soaked gauze and stored frozen in sealed plastic bags.

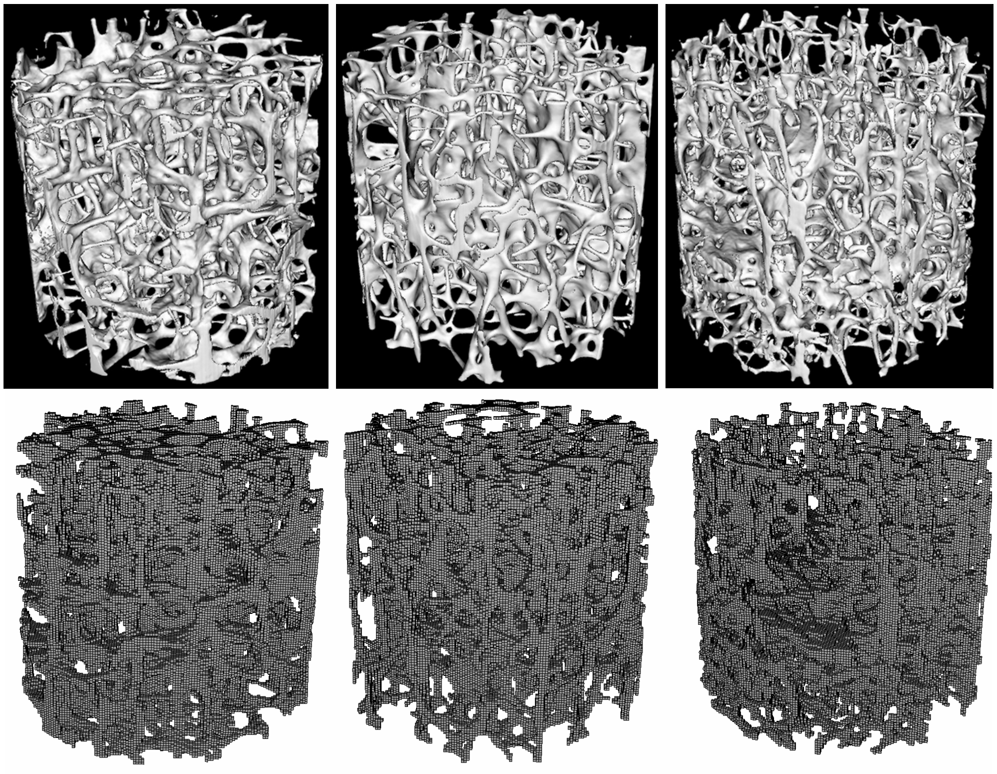
(a) Normal (F68) (b) Osteopenia (F61) (c) Osteoporosis (F65)

Figure 4.1. Examples of reconstructed volumes (top) and finite element meshes (bottom) for (a) normal, (b) osteopenic, and (c) osteoporotic subjects. Age of the female (F) subjects is denoted in years.

The reconstructed cancellous cores were reoriented to align the superior-inferior axis of the core with the vertical axis in the analysis software, and the ends of the cores were then cropped flat to a length of 7.5 mm (MicroView ABA 2.1.1., GE Healthcare, London, Ontario, Canada). MicroCT data were resampled at 17 μm to equilibrate voxel sizes between the two batch groups. For each core, bone voxels were distinguished from non-bone voxels (e.g., air, marrow, saline) using the Otsu method, which assumes a bimodal distribution of grayscale values and computes the bone threshold in HU by maximizing the between-class variance of two populations [34]. Because the use of a global threshold across specimens with dissimilar averages in mineral density may result in an inaccurate topology [6], a unique threshold was computed for each specimen. Cancellous bone volume fraction (BV/TV) was assessed for each of the reoriented, cropped cores after thresholding.

Finite-Element Modeling

Image data from the microCT scans were used to build specimen-specific finite element (FE) models for all 21 subjects [15,49]. Before creating the finite element mesh, the microCT data were coarsened to reduce the number of degrees of freedom and, consequently, the amount of computational memory required for solving the model. CT density values were averaged over blocks of 64 adjacent voxels of length 17.0 μm to form a single, coarsened cubic voxel of length 68.0 μm. Coarsening reduced the number of degrees of freedom for one model from about 24 million to about 1.3 million.

A finite element mesh was created for the gage length region of each cancellous bone core and measured 8.25 mm in diameter and 7.5 mm in length (Figure 4.1). Using the reoriented subvolumes obtained from microCT scans, each coarsened bone voxel, as defined by specimen-specific thresholding, was converted into an 8-noded linear brick element. Elements that were not connected to the primary structure, as a result of either the experimental coring procedure or artifacts of coarsening, were removed using the connectivity criterion of a 6-connected neighborhood. Unless an element shared a face with a portion of the primary bone structure, it was considered unconnected and was removed from the model. For all models, the number of unconnected elements removed was between 0.7% and 3.3% of the total number of elements. On average, the final FE models had 140,000 elements and 275,000 nodes, for a total of 820,000 degrees of freedom.

FE models were assigned isotropic material properties with a constant Poisson's ratio of 0.3 and a model-specific tissue modulus distribution that was either homogenous or heterogeneous. Three sets of models were analyzed, each set simulating a different modulus distribution, as follows:

1. A single homogeneous modulus of E = 20 GPa, chosen based on measurements from nanoindentation studies, was assigned to all elements for all subjects.
2. A specimen-specific homogeneous modulus was computed using the voxel mineral content from microCT scans and a linear modulus-density relationship using the formula [4]:

   $$E = E_c \left(\frac{\rho_{mean}}{\rho_c} \right)^b$$

   where E_c is the compressive tissue modulus for fully mineralized cortical bone (defined here as 20 GPa), ρ_{mean} is the mean apparent density over all mineralized voxels of the bone specimen, ρ_c is the apparent density of the SB3 cortical bone mineral standard, and b is the exponent defining the nature of the E-ρ relationship (i.e., b = 1 for a linear relationship). By assuming a linear relationship between apparent density and CT attenuation values, the ρ_{mean}/ρ_c ratio was computed using the ratio of the mean CT attenuation value to the SB3 mineral standard CT value. The resulting tissue modulus, E, was applied to all voxels within a given model.
3. A specimen-specific heterogeneous modulus was computed using the same linear E-ρ formula, except ρ_{mean} was replaced by the individual voxel apparent density ρ, and E was computed individually for each voxel using the CT value for that voxel.

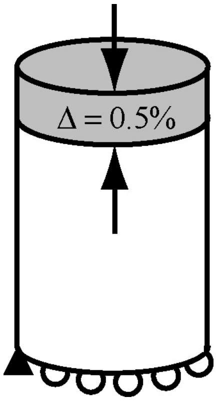

Figure 4.2. Boundary conditions for finite element models. A compressive strain of 0.25% was applied to nodes on the top surface of the mesh. Nodes on the bottom surface were constrained to in-plane motion, and nodes at one corner of the bottom surface were completely constrained to prevent rigid-body motion.

For each FE model, two outcome parameters were examined. First, the model-predicted apparent modulus was computed and compared with the experimental modulus to validate the model. Second, the distribution of minimum principal strains throughout the bone structure was investigated. Boundary conditions were applied to the models to replicate displacement-controlled uniaxial compressive loading in the linear elastic range (Figure 4.2). Pre-yield compression was simulated by displacing the nodes on the top surface of the cancellous core mesh to a strain of -0.25%. The nodes on the bottom surface of the mesh were treated as rollers constrained to in-plane motion only, and the nodes at one corner of the bottom surface were rigidly fixed to prevent rigid-body motion. The apparent modulus was calculated by summing the nodal reaction forces on the bottom surface of the core mesh and dividing by the cross-sectional area of a circle enclosing that surface. Minimum principal strains were analyzed at the element centroids located in a 5-mm central region of the volume of interest (VOI) to avoid elements with artificially high strains due to their proximity to the applied loads and boundary conditions. With the mesh created and refined, the appropriate tissue material properties defined, and the boundary conditions applied, the FE models were solved using a linear elastic static analysis (ABAQUS 6.3, HKS, Pawtucket, RI).

Mechanical Testing

Following microCT scans, the cancellous bone cores were tested destructively in uniaxial compression, and apparent-level properties were assessed to validate the FE models. After the cortical end plates were removed, the bone core ends were glued inside snug-fitting brass caps using a previously documented protocol designed to minimize end artifacts [23]. Approximately one-fourth of the overall core length was capped at each end. The diameter of each cancellous core was measured six times, and the exposed length was measured four times, using metric dial calipers, and the mean values were recorded. After the cyanoacrylate glue was cured for 24 hours, the capped cores were preconditioned for 5 cycles between 0 and 0.10% compressive strain and then loaded monotonically to failure at a rate of -0.50% strain per second (Mini-Bionix 858, MTS Systems Corporation, Eden Prairie, MN). Tests were conducted in displacement control at room temperature, and load and displacement data were sampled at 20 Hz. Displacement was measured with a 25-mm gage length axial extensometer (634.11F-24, MTS Systems Corporation, Eden Prairie, MN) attached to both brass caps.

Apparent mechanical properties were computed from the destructive testing data. Load and displacement data were converted to apparent stress and strain using standard mechanics formulae [13]. The yield point was defined using the 0.2% offset strain, and the ultimate point was defined using the maximum stress. Apparent elastic modulus was defined as the slope of a least-squares linear fit to the stress-strain data over 0.02-0.24% strain [26].

Statistical Analysis

The predictive power of the FE models was assessed by comparing the predicted apparent moduli to the experimentally measured apparent moduli using simple linear regressions for each model type. Because the outcome parameters of apparent modulus and minimum principal strain were computed using four methods for each subject (i.e., mechanical testing and the three sets of models), a repeated measures analysis on repeated factor *measurement method* was examined. The collective effect of measurement method and either sex or clinical bone diagnosis on apparent modulus was assessed with a repeated measures analysis of variance (RM ANOVA) on sex (or clinical diagnosis), measurement method, and their interaction (i.e., a model with full effects). Model-predicted apparent modulus values were compared to each other and to those obtained by mechanical testing using contrasts.

The median, minimum, maximum, and standard deviation (SD) of the minimum principal strain distributions were computed. To further examine these distributions, the minimum principal strain results were separated into the following three categories, and the percentage of elements in each category was computed for each model, as follows:

1. Low strain $\varepsilon_1 < 500$ microstrain
2. Middle strain $500 \leq \varepsilon_1 < 1500$ microstrain
3. High strain $\varepsilon_1 \geq 1500$ microstrain

The collective effect of measurement method and either sex or bone diagnosis on all minimum principal strain metrics was evaluated using a RM ANOVA with full effects. A significance level of 0.05 was used for all analyses (SAS 9.1, SAS Institute Inc., Cary, NC).

Results

CT-based finite element models were developed for lumbar spine cancellous bone of 21 subjects of both sexes, aged 58-92, with a broad range of DXA T-score (Table 4.1). Measured from microCT scans at a resolution of 17 µm, bone volume fraction of the L2 vertebrae varied greatly, ranging from 6.9% to 20.4%, with a coefficient of variation (COV) of 24%. Tissue BMD varied slightly less, ranging 0.6 to 1.2 g/cc, with a COV of 19%. Mean direct trabecular thickness was 0.090-0.135 mm, and mean direct trabecular separation was 1.07-1.63 mm for L2 cancellous bone cores. The distribution of tissue mineral throughout the bone volume, as assessed by normalized CT attenuation, differed somewhat between subjects, although the variation did not appear to be connected with either sex or clinical bone diagnosis (Figure 4.3).

For models with specimen-specific heterogeneous material properties, the distribution of bone tissue modulus was similar in shape for all subjects (Figure 4.4). Males may have a higher dispersion of tissue modulus values in the low modulus range and a higher mean modulus. Similarly, tissue modulus appeared to have distinct distributions by clinical bone diagnosis. Overall, the heterogeneous tissue modulus assigned to each element was 5.2 to 36.6 GPa and averaged 9.9-13.3 GPa over all elements for a given model, resulting in a global mean of 11.5 GPa over all models (Table 4.1). The variability in the heterogeneous tissue modulus was 23-33% across elements within a given model.

A uniform compressive strain was applied to the top surface of the cancellous core models, and the apparent elastic moduli were computed for the structure (Figure 4.5). The mean predicted apparent modulus was 0.13-1.50 GPa for homogeneous models, 0.09-0.79 GPa for heterogeneous models, and 0.10-0.79 GPa for specimen-

Table 4.1. Subject characteristics, cancellous bone tissue modulus, and apparent modulus for each measurement method. Mod = modulus, SD = standard deviation, Homo = homogeneous, Hetero = heterogeneous, SS = specimen-specific, Exp = Experimental, M = male, F = female.

				Tissue Mod (GPa)	Mean Apparent Mod (GPa)			
Sex	Age	L1-L4 T-score	Bone Diagnosis	Mean (SD)[†]	Homo	SS Hetero	SS Homo	Exp
F	73	0.5	Normal	10.5 (3.0)	1.50	0.79	0.79	0.81
M	56	0.2	Normal	10.4 (2.5)	0.87	0.45	0.45	0.60
F	74	-0.8	Normal	12.1 (3.2)	0.79	0.48	0.48	0.84
M	77	-0.8	Normal	12.4 (3.3)	0.38	0.23	0.24	0.34
M	65	-1.2	Osteopenia	10.2 (2.7)	0.81	0.41	0.41	0.55
M	79	-1.2	Osteopenia	13.0 (3.1)	0.65	0.41	0.42	0.48
F	58	-1.5	Osteopenia	13.3 (3.3)	0.58	0.39	0.38	0.73
M	71	-1.6	Osteopenia	11.9 (3.5)	0.13	0.09	0.10	0.66
M	67	-1.7	Osteopenia	10.6 (2.6)	0.82	0.45	0.44	0.48
M	63	-1.8	Osteopenia	12.2 (3.1)	0.63	0.38	0.38	0.55
F	61	-1.9	Osteopenia	12.0 (3.6)	0.62	0.38	0.37	0.59
M	63	-2.2	Osteopenia	13.3 (3.2)	0.74	0.51	0.49	0.77
M	69	-2.3	Osteopenia	9.9 (3.0)	0.55	0.27	0.27	0.35
F	92	-2.6	Osteoporosis	11.9 (3.4)	0.56	0.34	0.33	0.47
M	64	-2.9	Osteoporosis	13.0 (3.0)	0.84	0.55	0.55	0.60
F	61	-3.2	Osteoporosis	11.7 (3.4)	0.45	0.27	0.26	0.45
F	87	-3.5	Osteoporosis	11.5 (3.2)	0.55	0.32	0.31	0.43
F	87	-3.8	Osteoporosis	11.6 (3.1)	0.32	0.19	0.29	0.40
F	68	-3.9	Osteoporosis	10.2 (3.0)	0.61	0.31	0.31	0.17
F	65	-4.4	Osteoporosis	10.1 (2.6)	0.37	0.18	0.19	0.29
F	79	-5.2	Osteoporosis	10.3 (3.3)	0.30	0.16	0.15	0.20

[†] Mean tissue modulus for specimen-specific heterogeneous and homogeneous models. Modulus for universal homogeneous models equals 20 GPa.

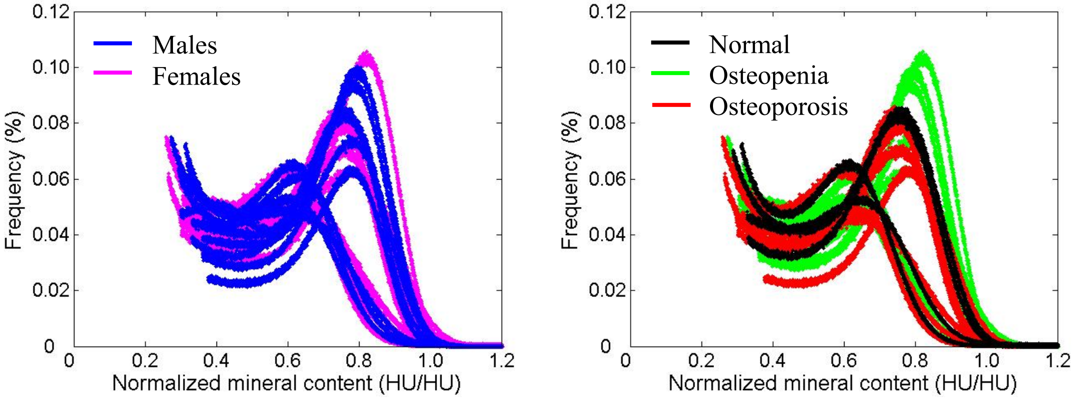

(a) (b)

Figure 4.3: Bone tissue mineral distribution assessed using CT attenuation for all 21 subjects, separated by (a) sex and (b) clinical bone diagnosis. Shown are the percentages of voxels for each CT attenuation value, normalized by the CT value for the cortical bone phantom. The CT attenuations shown here are only those above the bone threshold for each subject.

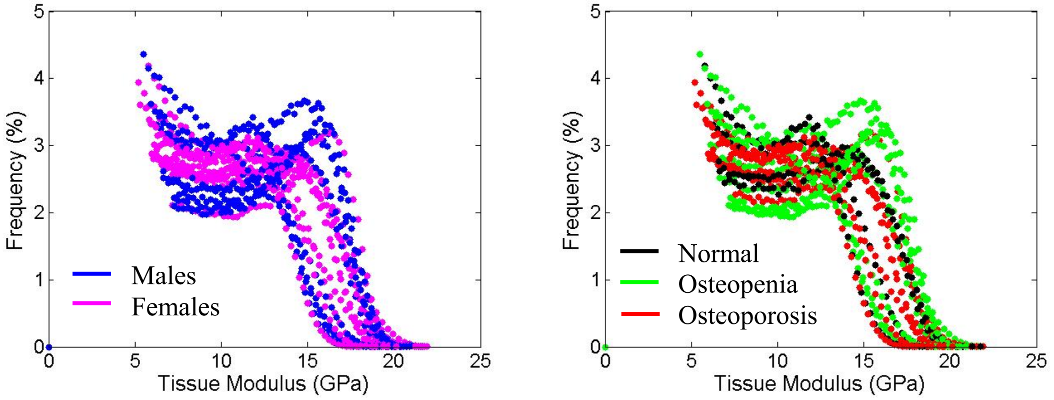

(a) (b)

Figure 4.4: Heterogeneous tissue moduli were assigned to elements based on a linear relationship with apparent density as measured by microCT attenuation for all 21 subjects. Tissue modulus distributions are shown separated by (a) sex and (b) clinical bone diagnosis, expressed as the percentages of voxels for each tissue modulus value.

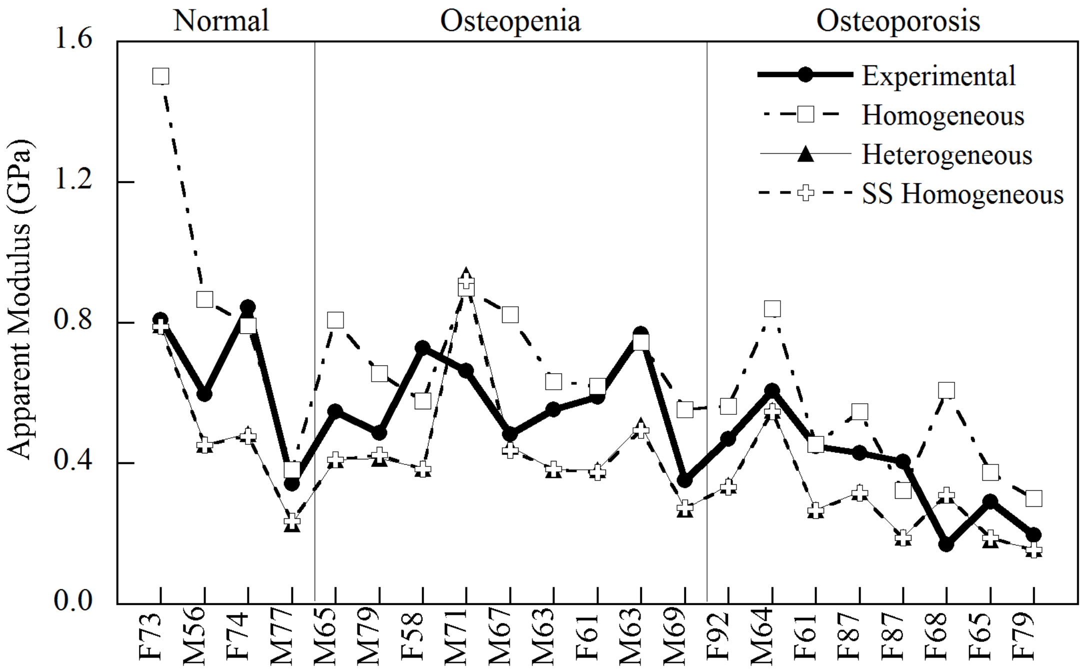

Figure 4.5. Apparent modulus from finite element models moderately predicted experimentally measured values, regardless of tissue moduli assigned (homogeneous, heterogeneous, or specimen-specific (SS) homogenous). Subjects are denoted by sex (M = male, F = female) and age in years.

specific homogeneous models (Table 4.1, Figure 4.6). Predicted values were all relatively similar to the experimentally measured values of 0.17-0.84 GPa. Regardless of the tissue modulus assigned, the FE-predicted modulus was linearly related to the experimental apparent modulus ($p = 0.012$ for homogeneous, $p = 0.0014$ for heterogeneous, and $p = 0.0016$ for specimen-specific homogeneous) (Figure 4.7).

Overall, the specimen-specific heterogeneous and homogeneous models predicted apparent modulus more accurately than universal homogeneous models. The slope for universal models (0.36) was much less than the desired unity slope, but the slopes for specimen-specific models (0.78 for both) came decidedly closer. In fact, the regression slopes had a 95% confidence interval of 0.3-1.2 and thus were not significantly different from the unity slope. Therefore, while universal homogeneous

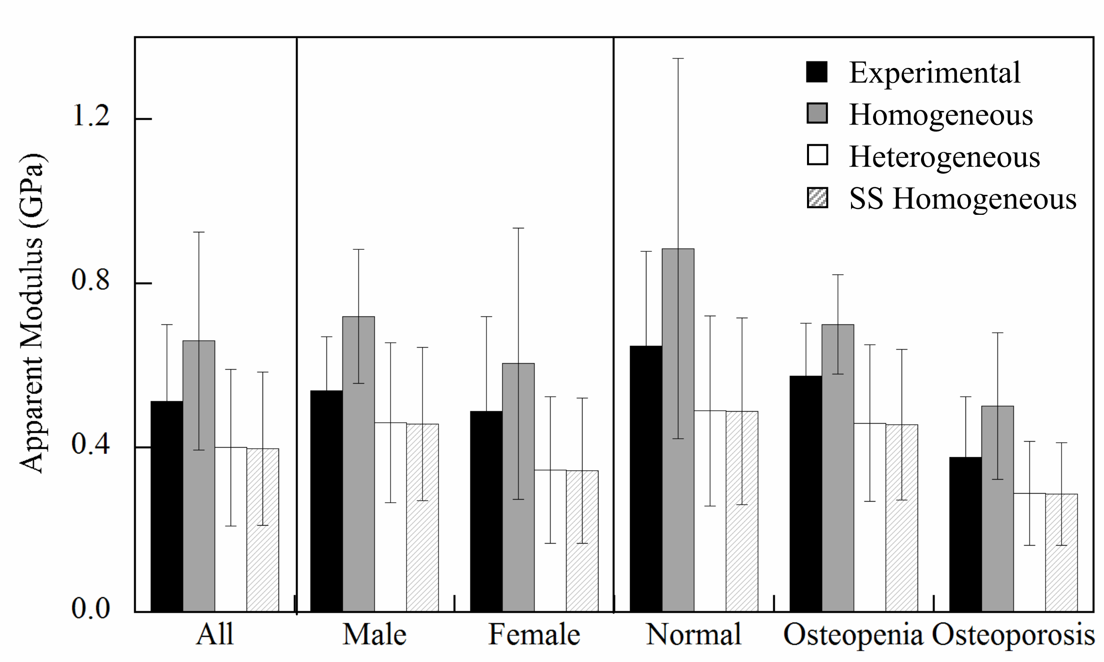

Figure 4.6. Apparent modulus (mean ± standard deviation) for each measurement method, shown for all subjects, separated by sex, and separated by clinical bone diagnosis. SS = specimen-specific.

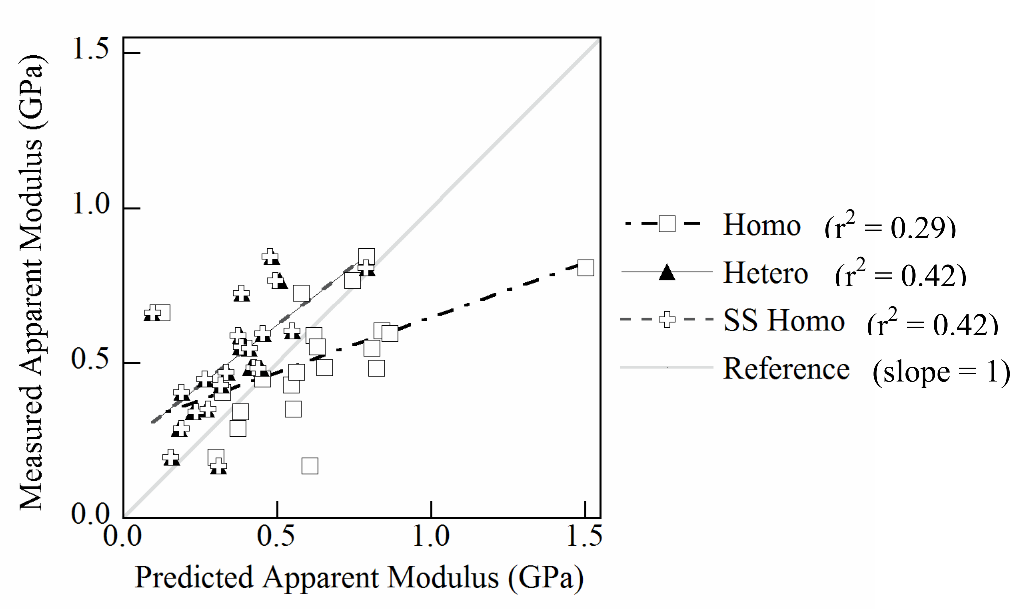

Figure 4.7. Specimen-specific (SS) heterogeneous and homogeneous finite element models improved the prediction of experimentally measured apparent modulus as compared to universal homogeneous models. The reference line represents a unity slope corresponding to an exact fit between predicted and measured values.

models had reasonable predictions only in the central range of apparent modulus values, the specimen-specific models improved the predictions across the entire range. In addition, specimen-specific heterogeneous and homogeneous models predicted measured apparent modulus more consistently than did universal homogeneous models, explaining 42% versus 29% of the variability in the data.

Regardless of sex or clinical bone diagnosis, apparent modulus differed significantly across the methods of measurement, i.e., mechanical testing, homogeneous model, heterogeneous model, and specimen-specific homogeneous model ($p < 0.0001$). The predicted apparent moduli were generally 1.7 times larger for homogeneous models than for heterogeneous models (contrast $p < 0.0001$, Figure 4.6). Apparent moduli predicted by specimen-specific homogeneous and heterogeneous models were not significantly different (contrast $p = 0.93$). Predicted moduli from universal homogeneous models were, on average, 1.3 times larger than experimentally measured moduli (contrast $p = 0.033$), which were 1.7 times larger than moduli predicted from either specimen-specific heterogeneous or homogeneous models (contrast $p = 0.0038$ and 0.0048, respectively).

Regardless of the measurement method, apparent modulus differed by clinical bone diagnosis but not by sex ($p = 0.023$ and 0.27, respectively, Figure 4.6). Specifically, apparent modulus decreased with declining bone mass across all experimental and computational methods, such that the cancellous bone from subjects with normal bone mass was stiffer than bone from either osteopenic ($p = 0.044$) or osteoporotic subjects ($p = 0.0067$) . Although apparent modulus tended to be slightly lower in females than in males across measurement method, this effect was not significant. The interaction between measurement method and sex or between method and bone diagnosis was also not significant ($p = 0.42$ and 0.078, respectively).

Distributions of compressive minimum principal strain (ε_1) were evaluated in the 5-mm central section of cancellous bone cores, away from the site of loading (Figure 4.8). Because the FE analyses were linear and displacements were applied, the results for ε_1 would be the same in both sets of homogeneous models (i.e., universal and specimen-specific). Therefore, only the results for universal homogeneous and specimen-specific heterogeneous models were evaluated. Because the distributions of ε_1 had a distinct negative skew, with the majority of the values concentrated near zero, the median was used as the measure of centrality in lieu of the mean. For clarity, the values of compressive strain will be discussed in terms of the absolute value. Distributions of ε_1 were slightly different for homogeneous and heterogeneous material models. Regardless of sex or clinical bone diagnosis, the median value for ε_1 was slightly lower (i.e., less negative) for heterogeneous material models ($p < 0.0001$, Figure 4.9), although the spread of values was slightly higher ($p < 0.0001$ for SD). Neither the minimum nor maximum value of ε_1 was significantly different between homogeneous and heterogeneous models ($p = 0.17$ and 0.14, respectively). None of the descriptors of minimum principal strain distribution (i.e., median, minimum, maximum, or SD) differed significantly by sex or bone diagnosis. The interaction between measurement method and sex and between method and bone diagnosis were also not significant.

To further examine these distributions, the minimum principal strain results were separated into discrete categories (Figure 4.10). When compared to homogeneous models, heterogeneous models had more elements in the low strain region (43.8% vs. 43.2%, $p = 0.0003$) and fewer elements in both the middle strain region (39.4% vs. 39.8%, $p = 0.014$) and the high strain region (16.4% vs. 16.2%, $p = 0.023$). However, these differences were very small and doubtfully produced any dramatic effects on the mechanical behavior of the cancellous bone samples.

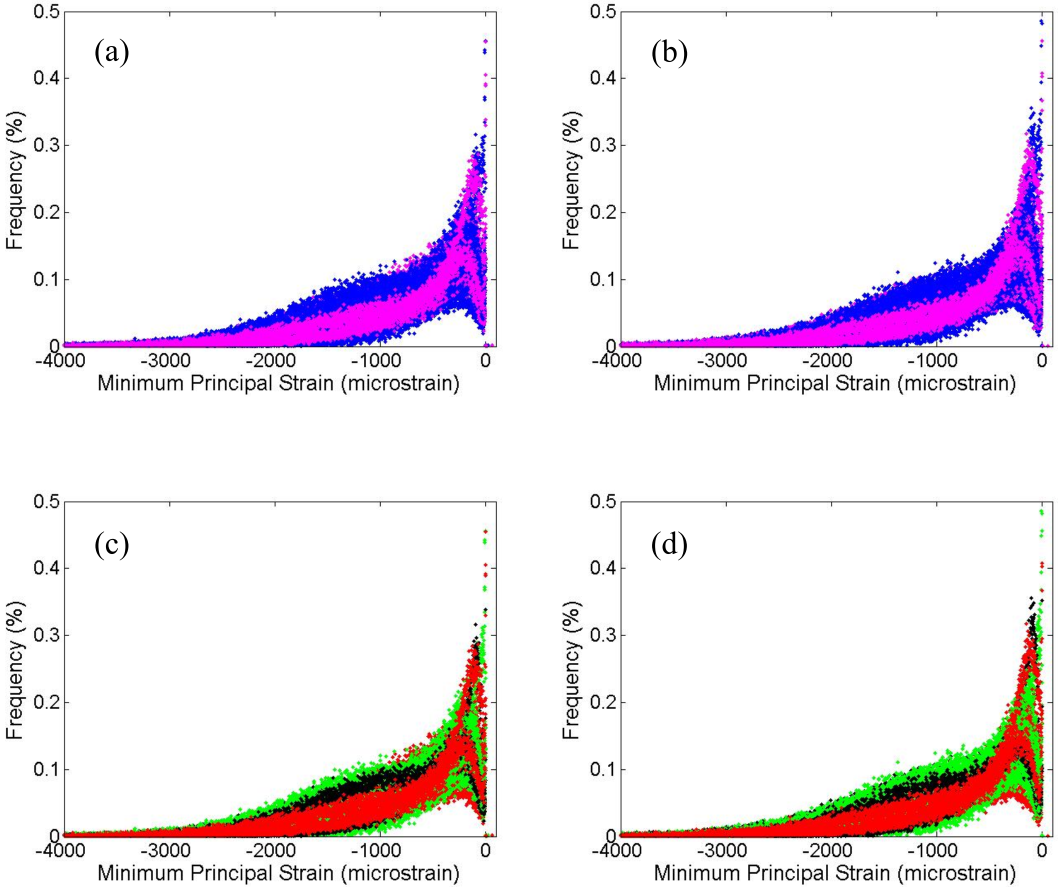

Figure 4.8. Distributions of minimum principal tissue strains within a 5-mm central section away from the site of loading for samples with universal homogeneous (a,c) and specimen-specific heterogeneous (b,d) material properties for all subjects, separated by sex (a,b) and clinical bone diagnosis (c,d).

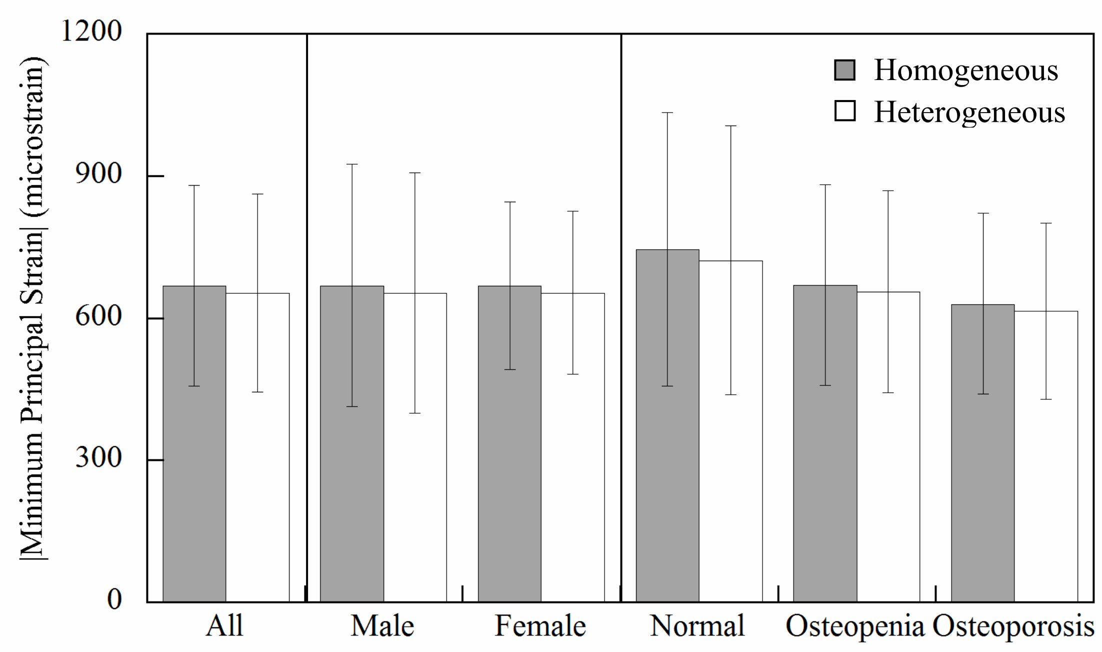

Figure 4.9. Absolute value of the median minimum principal strain averaged over all subjects, by sex, and by clinical bone diagnosis. Values are mean ± standard deviation.

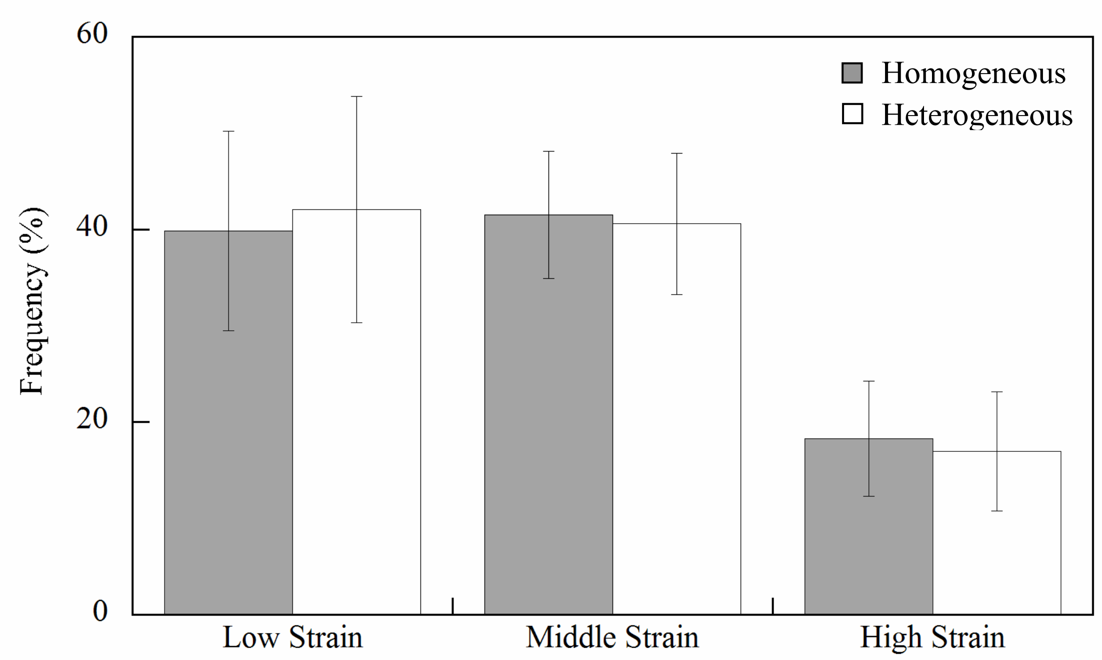

Figure 4.10. Percentage of elements in each minimum principal strain group (low, middle, and high strain). Values are mean ± standard deviation.

Discussion

In architecture-based finite element models of human vertebral cancellous bone, specimen-specific tissue moduli that varied linearly with apparent density substantially improved the overall prediction of apparent stiffness. The regression slope comparing predicted values with measured values was 2.2 times larger for all specimen-specific models, with both heterogeneous and homogeneous tissue moduli, than for universal homogeneous models and was closer to the desired unity slope. In addition, specimen-specific heterogeneous and homogeneous models explained the variability in the data to a greater extent than did universal homogeneous models (42% vs. 29%, respectively). On average, specimen-specific heterogeneous and homogeneous models reduced apparent stiffness by 40% as compared to universal homogeneous models. Therefore, although universal models generally overpredicted apparent modulus measured by mechanical testing, specimen-specific models tended to underpredict. Compared to experimental results, universal homogeneous models predicted a 1-260% (mean = 50%) stiffer material in 16 out of 21 subjects, and specimen-specific heterogeneous and homogeneous models predicted a 2-86% (mean = 31%) more compliant material in 20 out of 21 subjects.

Universal homogeneous models for females that overpredicted apparent modulus did so by an average of 60%, compared to 40% for males. Specimen-specific models that underpredicted apparent modulus did so by 33% for females and 29% for males. These results indicate that while specimen-specific finite element models predicted apparent stiffness similarly for males and females, adding tissue heterogeneity, whether within or between specimens, had a greater mean impact for females, and the variability in this change was also much higher for females. For both males and females, specimen-specific heterogeneous and homogeneous FE models provided conservative estimates of tissue stiffness in all but one subject. The material distributions derived from microCT for the specimen-specific models reflected true *in vivo* distributions over the volume of bone examined. The computed tissue modulus values were consistently lower than the assumed homogeneous value of 20 GPa (Figure 4.4), indicating that the specimen-specific models should more accurately assess the structural competence of cancellous bone.

Apparent tissue stiffness was virtually indistinguishable for specimen-specific heterogeneous and homogeneous models with tissue moduli that were mean-matched for each subject. These results suggest that the mean tissue modulus, rather than the distribution of tissue modulus, drives the overall mechanical behavior for vertebral cancellous bone. Although specimen-specific homogeneous models mostly underpredicted tissue stiffness, they did so predictably with a fairly universal offset from the experimental results across the range of apparent modulus data examined. Because a linear elastic analysis was performed, the tissue moduli used in the specimen-specific homogeneous models could be scaled appropriately to provide a closer prediction of the actual stiffness.

Using a linear relationship to convert apparent density (ρ) to tissue modulus (E) improved the accuracy of FE models in predicting apparent modulus, but an even better prediction is preferable before these types of models can be comfortably used for diagnosis or evaluation. The slope of the regression with measured apparent moduli increased by 2.2 times but was still 1.3 times smaller than the desired unity slope. The regression slope was not significantly different than the unity slope, but apparent moduli predicted by these heterogeneous models were still more accurate at higher values than at lower values.

Based on these observations, we hypothesized that a nonlinear E-ρ relationship would improve the accuracy of the heterogeneous models. The modulus-density relationship has been experimentally examined in several studies of human bone, and some have observed a power relationship of the form $E = a\rho^p$, where *a* is an empirical constant, and *p* ranged from 1.93 to 3 [4,10,14,20,25,40]. To test our theory, we incorporated a nonlinear E-ρ relationship with a power of 1.96 [14] into our heterogeneous models and computed apparent modulus. The slope of the measured versus predicted apparent modulus increased to 1.4, and the regression explained 52% of the variability in the data (Figure 4.11). Therefore, to obtain a slope closer to the unity slope, an exponent between 1 and 1.96 should be used, although the explanatory power of such a model would likely be no greater than 52%.

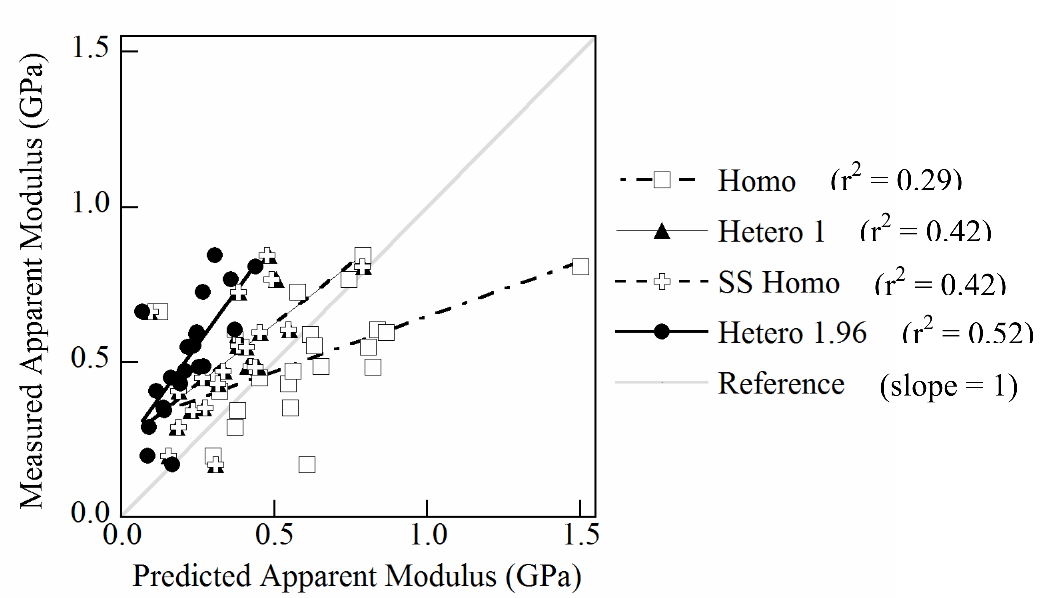

Figure 4.11. Apparent modulus from finite element models moderately predicted experimentally measured values, regardless of tissue moduli assigned: universal homogeneous (homo), linear heterogeneous (hetero 1), specimen-specific (SS) homogeneous, or nonlinear heterogeneous (hetero 1.96). The reference line represents a unity slope corresponding to an exact fit between predicted and measured values.

In the present study of vertebral bone specimens, the mean tissue elastic modulus for heterogeneous models (9.9-13.0 GPa) fell within the range of mean indentation modulus in human bone tissue examined by nanoindentation (7-32 GPa) [5,39,52]. Similarly, the predicted apparent stiffness from our models (0.94-1.5 GPa) correlated well with the results computed in previous finite element studies of human cancellous bone (0.42-1.1 GPa) [15,45,49]. Despite the observed spatial variations in tissue material properties of cancellous bone, few finite element studies to date have investigated the role of heterogeneous tissue properties in overall mechanical behavior, and those that did only examined a small number of samples (n = 3-5) [3,18,44]. Most of these studies used an assumed mineral distribution from localized tissue measurements to estimate tissue modulus and did not compare model-predicted outcomes to experimental data [18,44]. One study reported little change in apparent tissue stiffness with heterogeneous models, as compared to homogeneous models, although the tissue moduli were scaled about a small value of 5 GPa [44]. Another study, which incorporated more realistic heterogeneity using more variable tissue moduli and a higher mean modulus of 11-13 GPa, showed decreases in apparent stiffness of 7-24% [18].

One previous study incorporated tissue heterogeneity derived directly from mineral distributions to examine the ability of these models to predict mechanical behavior of cancellous bone [3]. Similar to our study, this study in rabbit cancellous bone scaled tissue moduli about a much higher reference modulus of 20 GPa and reported decreases of 35-43% in apparent stiffness (comparable to our 40%) for 26-34% variability in tissue modulus (similar to our 23-33%). In addition, their heterogeneous and specimen-specific homogeneous model predictions explained the experimentally measured mechanical behavior better than the homogeneous models ($r^2 = 0.85$ vs. 0.76, respectively). Although our model predictions did not have as high an explanatory power overall, our heterogeneous and specimen-specific homogeneous models also improved the prediction of apparent stiffness as compared to homogeneous models ($r^2 = 0.42$ vs. 0.29, respectively).

For our finite element models with heterogeneous tissue properties, the distributions of minimum principal strain were similar to those in the universal homogeneous models, and neither sex nor bone diagnosis appeared to have a substantial impact. Given that the bone tissue modulus varied up to 33% from 5-37 GPa over all subjects (mean = 10-13 GPa), compared with the 20 GPa homogeneous modulus, a more distinct distribution of tissue strains was expected, with higher strains located in regions of lower apparent density and thus lower modulus. In a study using voxel-based micro-FE models of specimens from two human proximal femora, average tissue-level principal strains were about 70% higher in the osteoporotic femur (520 microstrain) than in the normal femur (304 microstrain) and were more dispersed [46]. This study had a very small sample size, however, and the differences in tissue properties likely reflect normal interspecimen variability as much as true differences from bone degradation.

Our results indicate that, like apparent modulus, tissue strains appear to be driven more by the mean tissue modulus than by its spatial distribution, although the models used had limitations. In a study of rabbit cancellous bone, mineral content as assessed by CT attenuation increased with distance from trabecular surfaces, resulting in tissue that was about 15% more mineralized at the center of trabeculae than at the surface [31]. Intra-trabecular variation in tissue mineral content, and therefore in tissue modulus, could result in a structure that was stiffer and carried more load in the center and was more compliant and deformed more at the surface. The finite element meshes in our study had an element size of 68 μm, which corresponded to 0.5 to 0.8 times the mean direct trabecular thickness (Tb.Th*) for each specimen, resulting in an average of 1.2 to 2.2 elements per Tb.Th* across the bone volume of each specimen. Voxel sizes of this magnitude are increasingly susceptible to partial volume effects. Although adequate apparent modulus predictions have been validated for element sizes up to 1 Tb.Th*, especially for loading in the superior-inferior direction as in our present study, FE models with voxel sizes greater than 0.5*Tb.Th do not adequately capture true deformation modes [16]. To capture bending using a geometrically linear model, the mesh would need to have several elements across any given trabecular cross-section. Rather, our models behaved like a parallel-loaded system of aligned trabeculae. Better comparisons of tissue-level strains may be achieved with a finer mesh that allows for more realistic deformation modes.

The primary strength of our study was the use of a large sample size (n = 21) of both male and female human specimens representing a wide range of ages, bone density, and trabecular architecture at a clinically interesting site. To our knowledge, this study examined tissue heterogeneity using micro-FE models in the largest sample size to date. The direct conversion of CT mineral content to tissue modulus provided an accurate mapping of cancellous tissue properties throughout the bone volume and reflected the true *in vivo* material distributions better than previous studies using tissue moduli based on estimated tissue distributions [18,44]. In our study, mechanical tests were performed on the same specimens simulated by the FE models, thereby allowing a direct comparison between the measured and predicted results.

The primary weakness of our study was the relatively coarse mesh compared to the size of the trabecular structure. As mentioned previously, a finer mesh would more accurately evaluate deformation modes and might better assess tissue-level strains. The use of a larger element size allowed us to study a volume of bone that was 12-25 times larger than that studied in previous heterogeneous FE models, and thus may have more accurately captured variations in tissue properties. Nevertheless, the core of cancellous bone examined was still a relatively small volume from the centrum of a single vertebra and thus may not fully capture the nature or extent of tissue heterogeneity in the whole vertebra or in the spine in general. Strain energy density, which has been used to assess localized tissue damage [27], may be a better index for assessing the effects of tissue heterogeneity in our finite element models and should be examined in the future. In addition, the distribution of minimum principal strains should be investigated for the nonlinear heterogeneous material case to assess the impact of tissue property variations in a more physiologic material model. We chose to evaluate tissue strains, because they are independent of modulus and may provide more information about tissue failure than tissue stresses [24]. However, some studies have suggested that bone tissue failure is related to shear stress in bending trabeculae, and thus von Mises stress may provide a more accurate assessment of cancellous bone behavior [7,51]. Perhaps material variations would have a more pronounced effect on other measures of tissue stresses or strains than did minimum principal strain.

Based on our findings, the ability of linear, voxel-based finite element models to predict the apparent-level behavior of cancellous bone was substantially improved by using specimen-specific tissue material properties, compared with using universal homogeneous properties. Specimen-specific homogeneous models provided indistinguishable results from heterogeneous models and may be more desirable due to reduced model complexity and computational expense. Therefore, finite element models need to include some degree of heterogeneity, whether across subjects to account for interspecimen variability or within subjects to account for intraspecimen variability. However, specimen-specific models still only accounted for 40% of the variability in experimental data. Overall, both of the specimen-specific models provided conservative estimates of apparent stiffness, but the prediction differed somewhat depending on the level of apparent stiffness and may be improved by using a higher-order modulus-density relationship to define tissue properties. Regardless of sex or bone diagnosis, our study showed that specimen-specific FE models predicted the apparent stiffness of human vertebral cancellous bone more accurately than the commonly-used universal models. Our findings suggest that a virtual biopsy technique may be useful for predicting mechanical behavior in the aging population, although the tissue-level strains need to be investigated for a nonlinear material distribution to determine if the voxel-based FE models provide any useful information beyond a simple mechanical test.

References

1. Beaupré GS and Hayes WC (1985) Finite element analysis of a three-dimensional open-celled model for trabecular bone. *J Biomech Eng* 107(3):249-56.
2. Bourne BC, Morgan TG, Paschalis E, and van der Meulen MCH (2002) Cancellous bone anisotropy arises from both architecture and material properties. *Trans Orthop Res Soc* 27:558.
3. Bourne BC and van der Meulen MC (2004) Finite element models predict cancellous apparent modulus when tissue modulus is scaled from specimen CT-attenuation. *J Biomech* 37(5):613-21.
4. Carter DR and Hayes WC (1977) The compressive behavior of bone as a two-phase porous structure. *J Bone Joint Surg Am* 59-A:954-962.
5. Donnelly E, Williams RW, Downs SA, Dickinson ME, and Baker SP (2006) Quasistatic and dynamic nanomechanical properties of cancellous bone tissue relate to collagen content and organization. *Journal of Materials Research* 21:2106-2117.
6. Feldkamp LA, Goldstein SA, Parfitt AM, Jesion G, and Kleerekoper M (1989) The direct examination of three-dimensional bone architecture in vitro by computed tomography. *J Bone Miner Res* 4(1):3-11.
7. Fyhrie DP, Hoshaw SJ, Hamid MS, and Hou FJ (2000) Shear stress distribution in the trabeculae of human vertebral bone. *Ann Biomed Eng* 28(10):1194-9.
8. Gadeleta SJ, Boskey AL, Paschalis E, Carlson C, Menschik F, Baldini T, Peterson M, and Rimnac CM (2000) A physical, chemical, and mechanical study of lumbar vertebrae from normal, ovariectomized, and nandrolone decanoate-treated cynomolgus monkeys (Macaca fascicularis). *Bone* 27(4):541-50.

9. Goldstein SA (1987) The mechanical properties of trabecular bone: dependence on anatomic location and function. *J Biomech* 20(11-12):1055-61.

10. Goulet RW, Goldstein SA, Ciarelli MJ, Kuhn JL, Brown MB, and Feldkamp LA (1994) The relationship between the structural and orthogonal compressive properties of trabecular bone. *J Biomech* 27(4):375-89.

11. Grynpas M (1993) Age and disease-related changes in the mineral of bone. *Calcif Tissue Int* 53 Suppl 1:S57-64.

12. Guo XE, McMahon TA, Keaveny TM, Hayes WC, and Gibson LJ (1994) Finite element modeling of damage accumulation in trabecular bone under cyclic loading. *J Biomech* 27(2):145-55.

13. Hibbeler RC. Mechanics of Materials. Upper Saddle River, New Jersey: Prentice Hall, 1997.

14. Hodgskinson R and Currey JD (1992) Young's modulus, density and material properties in cancellous bone over a large density range. *J Mater Sci Mater Med* 3(377-381)

15. Hollister SJ, Brennan JM, and Kikuchi N (1994) A homogenization sampling procedure for calculating trabecular bone effective stiffness and tissue level stress. *J Biomech* 27(4):433-44.

16. Homminga J, Huiskes R, van Rietbergen B, Rüegsegger P, and Weinans H (2001) Introduction and evaluation of a gray-value voxel conversion technique. *J Biomech* 34(4):513-7.

17. Hou FJ, Lang SM, Hoshaw SJ, Reimann DA, and Fyhrie DP (1998) Human vertebral body apparent and hard tissue stiffness. *J Biomech* 31(11):1009-15.

18. Jaasma MJ, Bayraktar HH, Niebur GL, and Keaveny TM (2002) Biomechanical effects of intraspecimen variations in tissue modulus for trabecular bone. *J Biomech* 35(2):237-46.

19. Jensen KS, Mosekilde L, and Mosekilde L (1990) A model of vertebral trabecular bone architecture and its mechanical properties. *Bone* 11(6):417-23.

20. Kabel J, Odgaard A, van Rietbergen B, and Huiskes R (1999) Connectivity and the elastic properties of cancellous bone. *Bone* 24(2):115-120.

21. Kabel J, van Rietbergen B, Dalstra M, Odgaard A, and Huiskes R (1999) The role of an effective isotropic tissue modulus in the elastic properties of cancellous bone. *J Biomech* 32(7):673-80.

22. Kanis JA, Melton LJ, 3rd, Christiansen C, Johnston CC, and Khaltaev N (1994) The diagnosis of osteoporosis. *J Bone Miner Res* 9(8):1137-41.

23. Keaveny TM, Guo XE, Wachtel EF, McMahon TA, and Hayes WC (1994) Trabecular bone exhibits fully linear elastic behavior and yields at low strains. *J Biomech* 27:1127-1136.

24. Keaveny TM, Wachtel EF, Ford CM, and Hayes WC (1994) Differences between the tensile and compressive strengths of bovine tibial trabecular bone depend on modulus. *J Biomech* 27(9):1137-46.

25. Keller TS (1994) Predicting the compressive mechanical behavior of bone. *J Biomech* 27(9):1159-68.

26. Kopperdahl DL and Keaveny TM (1998) Yield strain behavior of trabecular bone. *J Biomech* 31(7):601-8.

27. Kopperdahl DL, Roberts AD, and Keaveny TM (1999) Localized damage in vertebral bone is most detrimental in regions of high strain energy density. *J Biomech Eng* 121(6):622-8.

28. Ladd AJ, Kinney JH, Haupt DL, and Goldstein SA (1998) Finite-element modeling of trabecular bone: comparison with mechanical testing and determination of tissue modulus. *J Orthop Res* 16(5):622-628.

29. Martin RB, Burr DB, and Sharkey NA. Skeletal Tissue Mechanics. New York: Springer, 1998.

30. Miller LM, Tibrewala J, and Carlson CS (2000) Examination of bone chemical composition in osteoporosis using fluorescence-assisted synchrotron infrared microspectroscopy. *Cell Mol Biol (Noisy-le-grand)* 46(6):1035-44.

31. Morgan TG, van der Meulen MCH, and Bourne BC (2002) Density versus depth from trabecular surface measured by quantitative microCT. *Trans Orthop Res Soc* 27:110.

32. Niebur GL, Feldstein MJ, Yuen JC, Chen TJ, and Keaveny TM (2000) High-resolution finite element models with tissue strength asymmetry accurately predict failure of trabecular bone. *J Biomech* 33(12):1575-83.

33. Niebur GL, Yuen JC, Burghardt AJ, and Keaveny TM (2001) Sensitivity of damage predictions to tissue level yield properties and apparent loading conditions. *J Biomech* 34(5):699-706.

34. Otsu N (1979) Threshold Selection Method from Gray-Level Histograms. *IEEE T Syst Man Cyb* 9(1):62-66.

35. Paschalis EP, Betts F, DiCarlo E, Mendelsohn R, and Boskey AL (1997) FTIR microspectroscopic analysis of human iliac crest biopsies from untreated osteoporotic bone. *Calcif Tissue Int* 61(6):487-92.

36. Paschalis EP, Betts F, DiCarlo E, Mendelsohn R, and Boskey AL (1997) FTIR microspectroscopic analysis of normal human cortical and trabecular bone. *Calcif Tissue Int* 61(6):480-6.

37. Paschalis EP, DiCarlo E, Betts F, Sherman P, Mendelsohn R, and Boskey AL (1996) FTIR microspectroscopic analysis of human osteonal bone. *Calcif Tissue Int* 59(6):480-7.

38. Raux P, Townsend PR, Miegel R, Rose RM, and Radin EL (1975) Trabecular architecture of the human patella. *J Biomech* 8(1):1-7.

39. Rho JY, Roy ME, 2nd, Tsui TY, and Pharr GM (1999) Elastic properties of microstructural components of human bone tissue as measured by nanoindentation. *J Biomed Mater Res* 45(1):48-54.

40. Rice JC, Cowin SC, and Bowman JA (1988) On the dependence of the elasticity and strength of cancellous bone on apparent density. *J Biomech* 21(2):155-68.

41. Silva MJ and Gibson LJ (1997) Modeling the mechanical behavior of vertebral trabecular bone: effects of age-related changes in microstructure. *Bone* 21(2):191-9.

42. Townsend PR, Raux P, Rose RM, Miegel RE, and Radin EL (1975) The distribution and anisotropy of the stiffness of cancellous bone in the human patella. *J Biomech* 8(6):363-7.

43. Ulrich D, Hildebrand T, van Rietbergen B, Müller R, and Rüegsegger P (1997) The quality of trabecular bone evaluated with micro-computed tomography, FEA and mechanical testing. *Stud Health Technol Inform* 40:97-112.

44. van der Linden JC, Birkenhager-Frenkel DH, Verhaar JA, and Weinans H (2001) Trabecular bone's mechanical properties are affected by its non-uniform mineral distribution. *J Biomech* 34(12):1573-80.

45. van Lenthe GH, Stauber M, and Muller R (2006) Specimen-specific beam models for fast and accurate prediction of human trabecular bone mechanical properties. *Bone* 39(6):1182-9.

46. van Rietbergen B, Huiskes R, Eckstein F, and Rüegsegger P (2003) Trabecular bone tissue strains in the healthy and osteoporotic human femur. *J Bone Miner Res* 18(10):1781-8.

47. van Rietbergen B, Majumdar S, Pistoia W, Newitt DC, Kothari M, Laib A, and Rüegsegger P (1998) Assessment of cancellous bone mechanical properties from micro-FE models based on micro-CT, pQCT and MR images. *Technol Health Care* 6(5-6):413-20.
48. van Rietbergen B, Weinans H, and Huiskes R (1997) Prospects of computer models for the prediction of osteoporotic bone fracture risk. *Stud Health Technol Inform* 40:25-32.
49. van Rietbergen B, Weinans H, Huiskes R, and Odgaard A (1995) A new method to determine trabecular bone elastic properties and loading using micromechanical finite-element models. *J Biomech* 28(1):69-81.
50. Yeh OC and Keaveny TM (1999) Biomechanical effects of intraspecimen variations in trabecular architecture: a three-dimensional finite element study. *Bone* 25(2):223-8.
51. Yeni YN, Hou FJ, Vashishth D, and Fyhrie DP (2001) Trabecular shear stress in human vertebral cancellous bone: intra- and inter-individual variations. *J Biomech* 34(10):1341-6.
52. Zysset PK, Guo XE, Hoffler CE, Moore KE, and Goldstein SA (1999) Elastic modulus and hardness of cortical and trabecular bone lamellae measured by nanoindentation in the human femur. *J Biomech* 32(10):1005-1012.

CHAPTER 5

SUMMARY AND DISCUSSION

Summary

The objective of this work was to examine the variation in cancellous bone material properties as a function of age, sex, and clinical bone status and to relate variations in trabecular material properties with cancellous structural behavior. Bone status is a clinical assessment measured most commonly using dual-energy X-ray absorptiometry (DXA). DXA is a non-invasive, two-dimensional technique that often involves a fan-shaped X-ray beam that magnifies images relative to their location within the beam [6,13]. Characterizing the degree of this magnification and its effect on bone mineral measurements is important for evaluating the diagnostic accuracy of this technique. Although DXA is used to predict the risk for developing a skeletal fracture resulting from low bone density, its resolution (~ 1 mm) cannot capture the complex structure or tissue properties of cancellous bone. Therefore, the inconsistent correlation of DXA measures with bone strength *in vitro* and *in situ* [1,5,24,26,28], or even with skeletal fracture occurrence [8], is not surprising. Determining which aspects of bone structure or material properties that DXA correlates with to what extent it correlates may explain its limited ability to predict fracture.

To quantify fan-beam magnification, various aluminum rod phantoms were scanned with DXA at incremental heights above the scanning table, which corresponded to different locations within the X-ray beam [6]. Both projected area and mineral content decreased 1.6-1.8% per centimeter above the table for round rods positioned longitudinally along the table similar to a lumbar spine or forearm scan.

For the height range examined, total variations of 7-8% in projected area and mineral content and 2% in mineral density were observed, and errors of this magnitude are problematic for clinical studies, particularly in pediatric subjects or others whose soft tissue thickness may change their location within the X-ray beam of a DXA scan.

Clinical bone status was evaluated with DXA for both male and female human cadaver spines. Thoracolumbar segments were scanned in the anterior-posterior direction and analyzed for areal bone mineral density (aBMD) and T-score, which relates a subject's aBMD to what it should be at peak bone mass. T-score is the clinical measure used to categorize a subject as having normal, osteopenic, or osteoporotic bone and thus is the bone status metric for this study [20]. Unfortunately, most laboratory techniques that have sufficient resolution to assess cancellous structure and material properties require an invasive bone biopsy and substantial radiation exposure and usually can only accommodate a small specimen. Therefore, a full-depth cylindrical core of cancellous bone (diameter = 8.25 mm) was drilled from the center of the T12 and L2 vertebral bodies of each spine for laboratory characterization.

Cancellous cores were scanned using micro-computed tomography (microCT) to assess microarchitecture and tissue mineral content and were compressed to failure to assess apparent material properties. Cancellous bone mass, architecture, and compressive material properties did not correlate with age or sex. Some of these measures somewhat correlated with T-score (i.e., bone status) but primarily for women. For women, DXA T-score correlated 50-80% with bone volume fraction and apparent density and 55-90% with apparent elastic modulus and strength at T12 and L2. Besides L2 principal mean intercept length for women, DXA did not relate to bone architecture measures for either sex. Therefore, DXA generally does not correlate with cancellous bone architecture for men or women and more accurately predicts bone mineral mass and material properties in the thoracolumbar spine for women than for men.

Compared to DXA, microCT bone volume fraction and apparent density were generally not better indicators of trabecular architecture or material properties in women or men, although BV/TV correlated 55-60% with mean direct trabecular separation for women. Similar to DXA, BV/TV and apparent density correlated 35-80% with apparent stiffness and strength for women but not for men. Tissue density, however, was a good indicator of trabecular architecture, at least in the thoracic spine. At T12, tissue density correlated 60-80% with measures of trabecular structure and orientation for men and 55% with primary trabecular orientation and degree of anisotropy for women, as well as 45% with ultimate strain in men. Given that T12 is a common site for fracture [9,17], especially in men, microCT tissue density may provide more information about cancellous bone strength in the thoracic spine not accounted for by DXA T-score and thus may improve the assessment of fracture risk in men.

Voxel-based finite element (FE) models can noninvasively probe the effects of architecture and tissue heterogeneity on structural behavior for a virtual biopsy of cancellous bone [2,16]. For models of human vertebral cancellous bone, specimen-specific tissue moduli that varied linearly with apparent density greatly improved the prediction of apparent stiffness as compared with a universal homogeneous modulus of 20 GPa. The regression slope for predicted versus measured apparent stiffness increased from 0.36 in universal homogeneous models to 0.78 in specimen-specific models, and the explanatory power also increased from 29% to 42%, respectively. The 95% confidence interval for the regression slope of specimen-specific models overlapped with 1.0 and thus was not significantly different from the unity slope. Interestingly, apparent stiffness was predicted equally well by all specimen-specific models, whether using a heterogeneous distribution of tissue moduli or a single homogeneous tissue modulus for all elements in a given model. Therefore, the overall mechanical behavior for vertebral cancellous bone seems to be driven more by the mean tissue modulus than by its distribution.

On average, FE models with universal homogeneous material properties overpredicted experimentally measured apparent stiffness by 38%, and specimen-specific models underpredicted it by 20%. The actual tissue modulus distributions, computed directly from microCT mineral distributions, were consistently lower than the assumed universal homogeneous modulus of 20 GPa. Therefore, the specimen-specific models, which are based on the true material distributions, provide conservative estimates of apparent stiffness and should assess the mechanical behavior of cancellous bone more accurately than the universal homogeneous models.

On average, the bone tissue modulus varied up to 33%, but the distributions of minimum principal strain were only slightly different in universal homogeneous and specimen-specific models. Although a more distinct distribution of tissue strains was expected, perhaps they also depend more on the mean tissue modulus than on its spatial distribution, or perhaps the meshes of our models were too coarse to capture realistic deformation modes [16]. In the future, a different heterogeneous material model that can more closely match the experimentally observed behavior will be examined [4,12,15,19,22,29]. A preliminary look at heterogeneous models with material properties that vary nonlinearly with apparent density showed that these models improved apparent stiffness predictions and thus may also more accurately assess tissue strains. Regardless, the nature of observed differences in tissue strains, especially stratified by sex and clinical bone status, needs to be quantified.

In conclusion, our work showed that DXA provides a more accurate prediction of bone mass, apparent stiffness, and strength in the thoracolumbar spine for women than for men. While DXA T-score did not correlate with cancellous bone architecture for either men or women, microCT tissue density correlated with some measures of trabecular structure, orientation, and anisotropy for both men and women. These findings suggest that microCT may beneficially supplement fracture risk assessment by DXA in women but may replace the DXA assessment altogether for men. The virtual biopsy technique examined in this work provided good predictions of apparent level behavior for vertebral cancellous bone, but a more representative material model must be developed so that the effect of inter- and intra-specimen material variations on tissue behavior can be investigated further.

The primary strength of our work was the examination of age-matched vertebral cancellous bone for a large group (n = 21) of both male and female cadavers that spanned a wide range of ages (56-92 years), clinical bone diagnosis (T-score = -5.2 to 0.2), bone volume fraction (7-20%), and trabecular architecture (mean trabecular thickness = 0.083-0.148 mm and separation = 1.07-1.63 mm). Despite the interspecimen variations in bone mass, architecture, and apparent material properties, none of these metrics differed significantly by age, sex, or the age-sex interaction. Therefore, we were able to examine more fundamental relationships among bone mass, architecture, and material properties using a variety of measurement techniques. A single set of cancellous bone cores were assessed using microCT, finite element modeling, and mechanical testing, so direct comparisons could be made between FE predicted and experimentally measured results, and these laboratory results were related back to the clinical DXA measurements taken in the same subjects. Individual FE models were based on microCT scans, which provided an accurate specimen-specific depiction of variations in both architecture and material properties throughout the volume of interest, and thus required few geometric or material assumptions.

The primary limitation of this work was that it only characterized cancellous bone material properties at the apparent level and did not examine local variations in tissue composition. Factors such as mineral:matrix ratio, carbonate:phosphate ratio, mineral crystallinity, and collagen maturity may also contribute to the quality of cancellous bone and may help explain some of the variability in bone material stiffness and strength not explained by bone mass, trabecular architecture, or apparent material properties. Tissue composition is currently being characterized for the cadaver specimens in this study using Fourier-transform infrared (FTIR) spectroscopy. In the future, we plan to relate the FTIR composition measures, especially those related to the inorganic components of the microstructure, to outcome measures from DXA, microCT, and mechanical testing. Furthermore, compositional properties and variation obtained from techniques such as Raman spectroscopy, second harmonic generation microscopy, and nanoindentation could be incorporated in architecture-based finite element models to more accurately simulate cancellous bone behavior.

Discussion and Future Directions

While recent advances in high-resolution tomographic and magnetic resonance (MR) techniques have improved the resolution of *in vivo* imaging, most cannot resolve cancellous bone structure at the level of a single trabecula. Although most often performed at peripheral sites like the wrist and heel, high-resolution magnetic resonance imaging was recently used to evaluate trabecular structure in the proximal femur [23]. However, the resolution with this technique, which is on the order of the trabecular thickness, remains insufficient to assess trabecular structure any better than histological techniques. If the resolution of MR imaging can be adequately improved to eliminate partial volume effects, trabecular structure and apparent density could be measured non-invasively in the elderly or other populations at high risk for developing skeletal fragility fractures. Architecture-based finite element models could factor bone tissue heterogeneity into the assessment to help devise preventive strategies and treatments to avoid fracture. While these *in vivo* techniques are still being developed, they may provide an appealing alternative to the low-resolution, two-dimensional DXA scan.

Osteoporosis assessment from T-score alone is rather limited. Categories of normal, osteopenic, and osteoporotic bone have somewhat arbitrary cutoff values that were selected by the World Health Organization (WHO) to classify those at risk for osteoporotic fracture. The categories were intended for epidemiologic studies and not for evaluating patients individually. Other factors such as rate of bone turnover, loading conditions, factor of risk, or whole bone strength indices may relate better to architecture and/or tissue heterogeneity than T-score alone [27,30]. Factor of risk, which is the ratio of skeletal load to failure load, is a non-invasive assessment of skeletal integrity and was recently correlated with spine, hip, and wrist fractures with clear age and sex differences [3,30]. For all three sites, the ratios of skeletal load to bone strength increased with age but more so in women than in men. This pattern of increasing factor of risk parallels the proportionately larger rise in fracture incidence observed in aging women and thus may help identify the mechanisms contributing to bone strength and fracture risk not captured by DXA.

For our architecture- and material-based FE models, the prediction of apparent stiffness was sensitive to tissue material properties. Therapies for osteoporosis have been shown to affect the tissue mineral properties. Bisphosphonates, for example, inhibit osteoclast activity [10] and thus tend to increase mineral content, as well as mineral crystal size [11,18,31]. The effects of therapy-induced changes in tissue properties on the structural performance of cancellous bone need to be characterized. High-resolution FE models derived from microCT scans cannot currently be developed for *in vivo* tissue and require an invasive biopsy procedure. Recently, apparent-level FE models were developed from *in vivo* quantitative computed tomography (QCT) scans and have been used to examine the biomechanical effects of osteoporosis therapies noninvasively [21]. These apparent-level voxel models, with element sizes on the order of 1 mm, have been shown to predict vertebral compressive strength better than bone mineral density from QCT and thus may greatly improve the clinical assessment of fracture risk [7].

Based on the results of our work and of other studies mentioned herein, trabecular architecture and tissue properties play an important role in the structural behavior of bone, at least for vertebral cancellous bone. Cancellous bone mass, structure, and mechanical properties can vary substantially across anatomic site and even across individuals [14,25,32]. Therefore, other sites and perhaps other populations need to be examined. Furthermore, the assessment of tissue geometry and material at the trabecular level may improve our ability to predict the mechanical behavior of cancellous bone and further explore the mechanisms behind bone fragility.

References

1. Bjarnason K, Hassager C, Svendsen OL, Stang H, and Christiansen C (1996) Anteroposterior and lateral spinal DXA for the assessment of vertebral body strength: comparison with hip and forearm measurement. *Osteoporos Int* 6(1):37-42.
2. Bourne BC and van der Meulen MC (2004) Finite element models predict cancellous apparent modulus when tissue modulus is scaled from specimen CT-attenuation. *J Biomech* 37(5):613-21.
3. Bouxsein ML, Melton LJ, 3rd, Riggs BL, Muller J, Atkinson EJ, Oberg AL, Robb RA, Camp JJ, Rouleau PA, McCollough CH, and Khosla S (2006) Age- and sex-specific differences in the factor of risk for vertebral fracture: a population-based study using QCT. *J Bone Miner Res* 21(9):1475-82.
4. Carter DR and Hayes WC (1977) The compressive behavior of bone as a two-phase porous structure. *J Bone Joint Surg Am* 59-A:954-962.
5. Cheng XG, Nicholson PH, Boonen S, Lowet G, Brys P, Aerssens J, van der Perre G, and Dequeker J (1997) Prediction of vertebral strength in vitro by spinal bone densitometry and calcaneal ultrasound. *J Bone Miner Res* 12(10):1721-8.
6. Cole JH, Scerpella TA, and van der Meulen MC (2005) Fan-beam densitometry of the growing skeleton: are we measuring what we think we are? *J Clin Densitom* 8(1):57-64.
7. Crawford RP, Cann CE, and Keaveny TM (2003) Finite element models predict in vitro vertebral body compressive strength better than quantitative computed tomography. *Bone* 33(4):744-50.
8. Cummings SR, Karpf DB, Harris F, Genant HK, Ensrud K, LaCroix AZ, and Black DM (2002) Improvement in spine bone density and reduction in risk of

vertebral fractures during treatment with antiresorptive drugs. *Am J Med* 112(4):281-9.

9. Evans SF and Davie MW (2000) Vertebral fractures and bone mineral density in idiopathic, secondary and corticosteroid associated osteoporosis in men. *Ann Rheum Dis* 59(4):269-75.
10. Fleisch HA (1997) Bisphosphonates: preclinical aspects and use in osteoporosis. *Ann Med* 29(1):55-62.
11. Fratzl P, Schreiber S, Roschger P, Lafage MH, Rodan G, and Klaushofer K (1996) Effects of sodium fluoride and alendronate on the bone mineral in minipigs: a small-angle X-ray scattering and backscattered electron imaging study. *J Bone Miner Res* 11(2):248-53.
12. Goulet RW, Goldstein SA, Ciarelli MJ, Kuhn JL, Brown MB, and Feldkamp LA (1994) The relationship between the structural and orthogonal compressive properties of trabecular bone. *J Biomech* 27(4):375-89.
13. Griffiths MR, Noakes KA, and Pocock NA (1997) Correcting the magnification error of fan beam densitometers. *J Bone Miner Res* 12(1):119-23.
14. Hildebrand T, Laib A, Müller R, Dequeker J, and Rüegsegger P (1999) Direct three-dimensional morphometric analysis of human cancellous bone: microstructural data from spine, femur, iliac crest, and calcaneus. *J Bone Miner Res* 14(7):1167-74.
15. Hodgskinson R and Currey JD (1992) Young's modulus, density and material properties in cancellous bone over a large density range. *J Mater Sci Mater Med* 3(377-381)
16. Homminga J, Huiskes R, van Rietbergen B, Rüegsegger P, and Weinans H (2001) Introduction and evaluation of a gray-value voxel conversion technique. *J Biomech* 34(4):513-7.

17. Johansson C, Mellstrom D, Rosengren K, and Rundgren A (1994) A community-based population study of vertebral fractures in 85-year-old men and women. *Age Ageing* 23(5):388-92.

18. Kaastad TS, Reikeras O, Madsen JE, Narum S, Stromme JH, Obrant KJ, and Nordsletten L (1997) Effects of clodronate on cortical and trabecular bone in ovariectomized rats on a low calcium diet. *Calcif Tissue Int* 61(2):158-64.

19. Kabel J, Odgaard A, van Rietbergen B, and Huiskes R (1999) Connectivity and the elastic properties of cancellous bone. *Bone* 24(2):115-120.

20. Kanis JA, Melton LJ, 3rd, Christiansen C, Johnston CC, and Khaltaev N (1994) The diagnosis of osteoporosis. *J Bone Miner Res* 9(8):1137-41.

21. Keaveny TM, Donley DW, Hoffmann PF, Mitlak BH, Glass EV, and San Martin JA (2007) Effects of teriparatide and alendronate on vertebral strength as assessed by finite element modeling of QCT scans in women with osteoporosis. *Journal of bone and mineral research* 22(1):149-57.

22. Keller TS (1994) Predicting the compressive mechanical behavior of bone. *J Biomech* 27(9):1159-68.

23. Krug R, Banerjee S, Han ET, Newitt DC, Link TM, and Majumdar S (2005) Feasibility of in vivo structural analysis of high-resolution magnetic resonance images of the proximal femur. *Osteoporos Int* 16(11):1307-14.

24. Lochmüller EM, Eckstein F, Kaiser D, Zeller JB, Landgraf J, Putz R, and Steldinger R (1998) Prediction of vertebral failure loads from spinal and femoral dual-energy X-ray absorptiometry, and calcaneal ultrasound: an in situ analysis with intact soft tissues. *Bone* 23(5):417-24.

25. Morgan EF and Keaveny TM (2001) Dependence of yield strain of human trabecular bone on anatomic site. *J Biomech* 34(5):569-77.

26. Moro M, Hecker AT, Bouxsein ML, and Myers ER (1995) Failure load of thoracic vertebrae correlates with lumbar bone mineral density measured by DXA. *Calcif Tissue Int* 56(3):206-9.
27. Myers ER and Wilson SE (1997) Biomechanics of osteoporosis and vertebral fracture. *Spine* 22(24):25S-31S.
28. Myers ER, Yano KA, Moro M, Silva MJ, and Hayes WC (1996) Lumbar bone mineral density predicts thoracolumbar failure load in compression and flexion. *Trans Orthop Res Soc* 21:645.
29. Rice JC, Cowin SC, and Bowman JA (1988) On the dependence of the elasticity and strength of cancellous bone on apparent density. *J Biomech* 21(2):155-68.
30. Riggs BL, Melton LJ, 3rd, Robb RA, Camp JJ, Atkinson EJ, Oberg AL, Rouleau PA, McCollough CH, Khosla S, and Bouxsein ML (2006) Population-based analysis of the relationship of whole bone strength indices and fall-related loads to age- and sex-specific patterns of hip and wrist fractures. *J Bone Miner Res* 21(2):315-23.
31. Roschger P, Fratzl P, Klaushofer K, and Rodan G (1997) Mineralization of cancellous bone after alendronate and sodium fluoride treatment: a quantitative backscattered electron imaging study on minipig ribs. *Bone* 20(5):393-7.
32. Rüegsegger P (2001) Imaging of bone structure. In: Cowin SC, Ed. Bone Mechanics Handbook. CRC Press: Boca Raton. pp. 9-1-9-24.

APPENDIX A: DATA

List of Abbreviations and Symbols

aBMD	areal bone mineral density
AP	anterior-posterior
Aniso##	Ratio of eigenvalues corresponding to principal material directions
BMC	bone mineral content
BV/TV	bone volume fraction
COR	center of rotation
COV	coefficient of variation = SD / mean
DA	degree of anisotropy = 1 – MIL3/MIL1
DOF	degrees of freedom
DXA	dual-energy X-ray absorptiometry
E	elastic modulus
ε_u	ultimate strain
ε_Y	yield strain
elems	elements
GL	gage length
Hetero	heterogeneous (linear modulus-density relationship)
Homo	homogeneous
HU	Hounsfield Units
MIL#	mean intercept length in principal direction #
microCT	micro-computed tomography
σ_u	ultimate stress
σ_Y	yield stress
SMI	structure model index
SS	specimen-specific
Tb.Th*	mean direct trabecular thickness (mean listed)
Tb.Sp*	mean direct trabecular separation (mean listed)
TMC	tissue mineral content
TMD	tissue mineral density (same as tisBMD)
VOI	volume of interest
Vol	volume
WA-BMD	width-adjusted bone mineral density from lateral DXA scans

Subject Identification Key

Subject ID	Spine ID	Core ID T12	Core ID L2	Sex	Age (yr)	T-score (L1-L4)	Bone Status
56601009	1	C3	C2	Male	64	-2.9	Osteoporosis
57400992	3	C4	C6	Female	61	-3.2	Osteoporosis
56601150	6	C7	C8	Female	87	-3.8	Osteoporosis
57100905	5	C9	C10	Female	87	-3.5	Osteoporosis
56601148	8	C11	C12	Female	61	-1.9	Osteopenia
51000686	9	C13	C14	Male	71	-1.6	Osteopenia
OH04020204	13	C15	C16	Female	92	-2.6	Osteoporosis
57401177	11	C17	C18	Male	63	-1.8	Osteopenia
56601390	12	C20	C21	Female	74	-0.8	Normal
56601076	10	C22	C23	Male	79	-1.2	Osteopenia
56601015	14	C24	C25	Female	58	-1.5	Osteopenia
56601394	16	C26	C27	Male	77	-0.8	Normal
56801530	15	C28	C29	Male	63	-2.2	Osteopenia
7753	17	C30T	C30L	Female	73	0.5	Normal
7912	21	C31T	C31L	Female	79	-5.2	Osteoporosis
7741	20	C32T	C32L	Male	69	-2.3	Osteopenia
8092	19	C33T	C33L	Male	65	-1.2	Osteopenia
8219	22	C34T	C34L	Male	67	-1.7	Osteopenia
7885	23	C35T	C35L	Male	56	0.2	Normal
7880	18	C36T	C36L	Female	68	-3.9	Osteoporosis
6062234	24	C37T	C37L	Female	65	-4.4	Osteoporosis

Notes:

- Three spines were exluded from the study and are not listed here
- Spine ID was assigned based on the chronology of DXA scans
- Core ID was assigned based on the chronology of microCT scans

Demographic Data

Note: All subjects were Caucasian

Subject ID	Sex	Age (yr)	Height (in)	Weight (lb)	Cause of Death
56601009	Male	64	---	---	Myocardial infarction
57400992	Female	61	66	100	Lung cancer
56601150	Female	87	64	130	Respiratory failure
57100905	Female	87	58	95	Coronary heart failure
56601148	Female	61	63	110	Intracranial bleeding
51000686	Male	71	68	160	Glioblastoma
OH04020204	Female	92	---	---	Pneumonia
57401177	Male	63	73	170	Lung cancer
56601390	Female	74	67	166	Myocardial infarction
56601076	Male	79	72	160	Stroke
56601015	Female	58	---	---	Throat cancer
56601394	Male	77	71	152	Myocardial infarction
56801530	Male	63	63	218	Myocardial infarction
7753	Female	73	---	---	Cardiorespiratory arrest
7912	Female	79	---	---	Respiratory failure
7741	Male	69	---	---	Lung cancer
8092	Male	65	---	---	Respiratory failure, pancreatic cancer
8219	Male	67	---	---	Lung cancer
7885	Male	56	---	---	Cardiorespiratory arrest
7880	Female	68	---	---	Respiratory failure
6062234	Female	65	65	160	Acute respiratory failure

Clinical DXA Scans – Hospital for Special Surgery

Hologic QDR 4500A Delphi, S/N 45758
Paired AP/Lateral lumbar spine scans in fast array mode

Spine ID = 56601009

Levels L1-L4
AP Scan (A11190313)

Levels	Area (cm^2)	BMC (g)	aBMD (g/cm^2)	T-score
L1	12.73	9.00	0.707	-2.7
L2	14.56	11.72	0.805	-2.6
L3	15.15	11.58	0.764	-3.1
L4	17.91	14.25	0.796	-3.2
L1-L4	60.34	46.54	0.771	-2.9

Lateral scan (A11190314)

Levels	Area (cm^2)	BMC (g)	aBMD (g/cm^2)	WA-BMD (g/cm^3)	T-score
L2	9.96	5.76	0.578	0.178	
L3	11.12	6.85	0.616	0.183	
L4	11.63	8.48	0.730	0.188	
L2-L4	32.71	21.09	0.645	0.184	

Levels T11-L2
AP Scan (A11190316)

Levels		Area	BMC	aBMD	T-score	
Actual	Analyzed	(cm^2)	(g)	(g/cm^2)	Analyzed	Actual
T11	L1	11.84	7.34	0.620	-3.5	---
T12	L2	12.33	7.28	0.591	-4.6	---
L1	L3	13.48	9.26	0.687	-3.8	-2.9
L2	L4	14.03	11.35	0.809	-3.1	-2.6
T11-L2	L1-L4	51.67	35.24	0.682	-3.7	---

Lateral scan (A11190317)

Levels		Area	BMC	aBMD	WA-BMD	T-score	
Actual	Analyzed	(cm^2)	(g)	(g/cm^2)	(g/cm^3)	Analyzed	Actual
T12	L2	9.27	4.71	0.508	0.164		---
L1	L3	8.97	4.27	0.476	0.154		---
L2	L4	9.67	5.77	0.597	0.180		
T11-L2	L1-L4	27.90	14.75	0.529	0.167		---

Spine ID = 57400992 contained levels T11-L2 only

Levels T11-L2

AP Scan (A1119031C)

Levels		Area	BMC	aBMD	T-score	
Actual	Analyzed	(cm^2)	(g)	(g/cm^2)	Analyzed	Actual
T11	L1	9.05	4.86	0.538	-3.5	---
T12	L2	10.23	5.16	0.504	-4.8	---
L1	L3	11.81	6.75	0.571	-4.7	-3.2
L2	L4	12.81	8.64	0.675	-4.0	-3.2
T11-L2	L1-L4	43.89	25.41	0.579	-4.3	---

Lateral scan (A1119031D)

Levels		Area	BMC	aBMD	WA-BMD	T-score	
Actual	Analyzed	(cm^2)	(g)	(g/cm^2)	(g/cm^3)	Analyzed	Actual
T12	L2	7.62	2.28	0.299	0.113	-5.5	---
L1	L3	8.32	2.87	0.345	0.131	-5.7	---
L2	L4	8.80	3.60	0.409	0.148	-4.5	-4.4
T11-L2	L1-L4	24.74	8.75	0.354	0.132	-5.6	---

Spine ID = 56601150

Levels L1-L4

AP Scan (A11190321)

Levels	Area (cm^2)	BMC (g)	aBMD (g/cm^2)	T-score
L1	13.17	8.29	0.629	-2.7
L2	12.15	7.13	0.587	-4.0
L3	12.48	7.95	0.637	-4.1
L4	16.17	10.64	0.658	-4.2
L1-L4	53.96	34.00	0.630	-3.8

Lateral scan (A11190322)

Levels	Area (cm^2)	BMC (g)	aBMD (g/cm^2)	WA-BMD (g/cm^3)	T-score
L2	9.76	4.77	0.488	0.139	-3.6
L3	10.99	4.87	0.443	0.123	-4.6
L4	10.99	6.12	0.557	0.137	-3.0
L2-L4	31.74	15.76	0.497	0.133	-3.9

Levels T11-L2

AP Scan (A11200304)

Levels		Area	BMC	aBMD	T-score	
Actual	Analyzed	(cm^2)	(g)	(g/cm^2)	Analyzed	Actual
T11	L1	12.06	4.69	0.389	-4.9	---
T12	L2	12.89	5.51	0.428	-5.5	---
L1	L3	12.48	7.70	0.617	-4.2	-2.8
L2	L4	12.51	7.30	0.584	-4.8	-4.0
T11-L2	L1-L4	49.93	25.21	0.505	-4.9	---

Lateral scan (A11200305)

Levels		Area	BMC	aBMD	WA-BMD	T-score	
Actual	Analyzed	(cm^2)	(g)	(g/cm^2)	(g/cm^3)	Analyzed	Actual
T12	L2	8.56	2.06	0.241	0.077	-6.1	---
L1	L3	9.29	4.21	0.453	0.135	-4.5	---
L2	L4	11.56	5.41	0.468	0.125	-3.9	-3.8
T11-L2	L1-L4	29.40	11.69	0.397	0.117	-5.0	---

Spine ID = 57100905

Levels L1-L4

AP Scan (A1119031V)

Levels	Area (cm^2)	BMC (g)	aBMD (g/cm^2)	T-score
L1	9.25	4.43	0.479	-4.1
L2	10.59	6.30	0.595	-3.9
L3	11.52	8.37	0.727	-3.2
L4	12.40	9.85	0.794	-2.9
L1-L4	43.75	28.95	0.662	-3.5

Lateral scan (A1119031W)

Levels	Area (cm^2)	BMC (g)	aBMD (g/cm^2)	WA-BMD (g/cm^3)	T-score
L2	8.10	2.29	0.282	0.106	-5.7
L3	8.35	3.81	0.456	0.152	-4.5
L4	10.26	5.11	0.498	0.150	-3.6
L2-L4	26.71	11.21	0.420	0.140	-4.8

Levels T11-L2

AP Scan (A1119031T)

Levels		Area	BMC	aBMD	T-score	
Actual	Analyzed	(cm^2)	(g)	(g/cm^2)	Analyzed	Actual
T11	L1	8.22	3.87	0.470	-4.1	---
T12	L2	9.59	4.39	0.458	-5.2	---
L1	L3	11.36	5.01	0.441	-5.8	-4.4
L2	L4	11.57	6.55	0.566	-5.0	-4.2
T11-L2	L1-L4	40.73	19.81	0.486	-5.1	---

Lateral scan (A1119031U)

Levels		Area	BMC	aBMD	WA-BMD	T-score	
Actual	Analyzed	(cm^2)	(g)	(g/cm^2)	(g/cm^3)	Analyzed	Actual
T12	L2	5.77	2.04	0.353	0.123	-5.0	---
L1	L3	6.45	1.97	0.305	0.103	-6.2	---
L2	L4	7.41	2.50	0.337	0.116	-5.3	-5.1
T11-L2	L1-L4	19.63	6.50	0.331	0.114	-5.8	---

Spine ID = 56601148

Levels L1-L4

AP Scan (A0713041G)

Levels	Area (cm^2)	BMC (g)	aBMD (g/cm^2)	T-score
L1	12.25	8.95	0.731	-1.8
L2	14.02	12.14	0.866	-1.5
L3	14.48	13.02	0.899	-1.7
L4	15.72	12.89	0.820	-2.7
L1-L4	56.46	47.00	0.833	-1.9

Lateral scan (A0713041H)

Levels	Area (cm^2)	BMC (g)	aBMD (g/cm^2)	WA-BMD (g/cm^3)	T-score
L2	8.70	4.34	0.499	0.168	-3.5
L3	8.95	4.86	0.543	0.159	-3.5
L4	9.63	6.55	0.680	0.167	-1.8
L2-L4	27.28	15.75	0.577	0.164	-2.9

Levels T11-L2

AP Scan (A0713041I)

Levels		Area	BMC	aBMD	T-score	
Actual	Analyzed	(cm^2)	(g)	(g/cm^2)	Analyzed	Actual
T11	L1	9.64	6.55	0.680	-2.2	---
T12	L2	11.78	8.13	0.690	-3.1	---
L1	L3	12.43	9.00	0.724	-3.3	-1.8
L2	L4	14.26	12.27	0.861	-2.3	-1.5
T11-L2	L1-L4	48.10	35.94	0.747	-2.7	---

Lateral scan (A0713041J)

Levels		Area	BMC	aBMD	WA-BMD	T-score	
Actual	Analyzed	(cm^2)	(g)	(g/cm^2)	(g/cm^3)	Analyzed	Actual
T12	L2	7.31	4.00	0.547	0.167	-3.1	---
L1	L3	8.01	4.43	0.553	0.183	-3.4	---
L2	L4	9.36	5.65	0.604	0.190	-2.6	-2.5
T11-L2	L1-L4	24.69	14.08	0.570	0.181	-3.0	---

Spine ID = 51000686

Levels L1-L4

AP Scan (A0713041O)

Levels	Area (cm^2)	BMC (g)	aBMD (g/cm^2)	T-score
L1	14.63	12.21	0.835	-1.6
L2	16.42	13.13	0.800	-2.7
L3	18.36	16.54	0.901	-1.8
L4	17.70	19.31	1.091	-0.5
L1-L4	67.10	61.19	0.912	-1.6

Lateral scan (A0713041P)

Levels	Area (cm^2)	BMC (g)	aBMD (g/cm^2)	WA-BMD (g/cm^3)	T-score
L2	9.71	5.50	0.566	0.155	
L3	11.03	7.08	0.642	0.171	
L4	12.35	9.97	0.807	0.193	
L2-L4	33.09	22.55	0.682	0.177	

Levels T11-L2

AP Scan (A0713041Q)

Levels		Area (cm^2)	BMC (g)	aBMD (g/cm^2)	T-score	
Actual	Analyzed				Analyzed	Actual
T11	L1	12.80	10.86	0.849	-1.4	---
T12	L2	14.91	12.61	0.846	-2.3	---
L1	L3	15.68	12.93	0.825	-2.5	-1.7
L2	L4	17.47	16.11	0.922	-2.0	-1.6
T11-L2	L1-L4	60.85	52.50	0.863	-2.1	---

Lateral scan (A0713041R)

Levels		Area (cm^2)	BMC (g)	aBMD (g/cm^2)	WA-BMD (g/cm^3)	T-score	
Actual	Analyzed					Analyzed	Actual
T12	L2	9.65	5.95	0.617	0.181		---
L1	L3	10.14	5.91	0.583	0.167		---
L2	L4	11.85	8.14	0.687	0.182		
T11-L2	L1-L4	31.64	20.00	0.632	0.177		---

Spine ID = OH04020204

Levels L1-L4
AP Scan (A07140405)

Levels	Area (cm^2)	BMC (g)	aBMD (g/cm^2)	T-score
L1	11.08	7.80	0.705	-2.0
L2	11.42	8.69	0.761	-2.4
L3	12.99	10.65	0.820	-2.4
L4	15.30	11.33	0.740	-3.4
L1-L4	50.78	38.48	0.758	-2.6

Lateral scan (A07140406)

Levels	Area (cm^2)	BMC (g)	aBMD (g/cm^2)	WA-BMD (g/cm^3)	T-score
L2	8.02	3.69	0.460	0.160	-3.9
L3	9.85	4.89	0.496	0.157	-4.0
L4	9.65	4.60	0.477	0.140	-3.8
L2-L4	27.52	13.18	0.479	0.152	-4.1

Levels T11-L2
AP Scan (A07140407)

Levels		Area	BMC	aBMD	T-score	
Actual	Analyzed	(cm^2)	(g)	(g/cm^2)	Analyzed	Actual
T11	L1	9.48	5.79	0.611	-2.9	---
T12	L2	10.93	6.73	0.616	-3.7	---
L1	L3	11.13	7.76	0.698	-3.5	-2.1
L2	L4	11.69	8.90	0.761	-3.2	-2.4
T11-L2	L1-L4	43.22	29.18	0.675	-3.4	---

Lateral scan (A07140408)

Levels		Area	BMC	aBMD	WA-BMD	T-score	
Actual	Analyzed	(cm^2)	(g)	(g/cm^2)	(g/cm^3)	Analyzed	Actual
T12	L2	7.68	3.55	0.462	0.163	-3.9	---
L1	L3	8.72	4.17	0.478	0.165	-4.2	---
L2	L4	9.60	5.07	0.528	0.180	-3.3	-3.2
T11-L2	L1-L4	26.00	12.78	0.492	0.170	-3.9	---

Spine ID = 57401177

Levels L1-L4

AP Scan (A07130420)

Levels	Area (cm^2)	BMC (g)	aBMD (g/cm^2)	T-score
L1	16.93	14.01	0.828	-1.6
L2	16.93	15.49	0.915	-1.6
L3	17.07	16.20	0.949	-1.4
L4	16.38	14.71	0.898	-2.2
L1-L4	67.30	60.41	0.898	-1.8

Lateral scan (A07130421)

Levels	Area (cm^2)	BMC (g)	aBMD (g/cm^2)	WA-BMD (g/cm^3)	T-score
L2	11.36	7.01	0.617	0.168	
L3	11.79	8.28	0.702	0.190	
L4	11.76	9.98	0.849	0.246	
L2-L4	34.91	25.27	0.724	0.201	

Levels T11-L2

AP Scan (A07130422)

Levels		Area	BMC	aBMD	T-score	
Actual	Analyzed	(cm^2)	(g)	(g/cm^2)	Analyzed	Actual
T11	L1	15.55	12.71	0.818	-1.7	---
T12	L2	14.42	9.97	0.692	-3.7	---
L1	L3	16.86	13.83	0.820	-2.6	-1.7
L2	L4	17.31	15.84	0.915	-2.1	-1.6
T11-L2	L1-L4	64.13	52.35	0.816	-2.5	---

Lateral scan (A07130423)

Levels		Area	BMC	aBMD	WA-BMD	T-score	
Actual	Analyzed	(cm^2)	(g)	(g/cm^2)	(g/cm^3)	Analyzed	Actual
T12	L2	11.43	7.54	0.660	0.182		---
L1	L3	12.98	8.64	0.666	0.177		---
L2	L4	13.08	9.89	0.756	0.202		
T11-L2	L1-L4	37.50	26.07	0.695	0.187		---

Spine ID = 56601390

Levels L1-L4
AP Scan (A07130420)

Levels	Area (cm^2)	BMC (g)	aBMD (g/cm^2)	T-score
L1	12.11	11.48	0.949	0.2
L2	12.13	13.96	1.151	1.1
L3	12.77	11.21	0.878	-1.9
L4	17.59	15.85	0.901	-2.0
L1-L4	54.59	52.50	0.962	-0.8

Lateral scan (A07130421)

Levels	Area (cm^2)	BMC (g)	aBMD (g/cm^2)	WA-BMD (g/cm^3)	T-score
L2	7.83	6.30	0.804	0.230	-0.5
L3	10.44	5.26	0.504	0.137	-3.9
L4	8.60	5.92	0.689	0.161	-1.7
L2-L4	26.87	17.48	0.650	0.169	-2.0

Levels T11-L2
AP Scan (A07130422)

Levels		Area	BMC	aBMD	T-score	
Actual	Analyzed	(cm^2)	(g)	(g/cm^2)	Analyzed	Actual
T11	L1	11.34	6.41	0.565	-3.3	---
T12	L2	13.01	7.37	0.566	-4.2	---
L1	L3	12.09	11.06	0.915	-1.5	-0.1
L2	L4	12.55	14.40	1.148	0.3	1.1
T11-L2	L1-L4	48.98	39.24	0.801	-2.2	---

Lateral scan (A07130423)

Levels		Area	BMC	aBMD	WA-BMD	T-score	
Actual	Analyzed	(cm^2)	(g)	(g/cm^2)	(g/cm^3)	Analyzed	Actual
T12	L2	8.54	4.22	0.494	0.151	-3.6	---
L1	L3	9.34	7.38	0.790	0.243	-0.7	---
L2	L4	9.09	7.69	0.846	0.234	-0.1	-0.1
T11-L2	L1-L4	26.98	19.29	0.715	0.212	-1.2	---

Spine ID = 56601076

Levels L1-L4

AP Scan (A0713041S)

Levels	Area (cm^2)	BMC (g)	aBMD (g/cm^2)	T-score
L1	13.93	13.59	0.976	-0.3
L2	15.53	14.69	0.946	-1.3
L3	16.98	16.62	0.979	-1.1
L4	19.57	18.07	0.923	-2.0
L1-L4	66.00	62.97	0.954	-1.2

Lateral scan (A0713041T)

Levels	Area (cm^2)	BMC (g)	aBMD (g/cm^2)	WA-BMD (g/cm^3)	T-score
L2	11.93	7.65	0.641	0.180	
L3	12.05	8.44	0.700	0.206	
L4	13.04	9.34	0.716	0.179	
L2-L4	37.01	25.43	0.687	0.188	

Levels T11-L2

AP Scan (A0713041U)

Levels		Area	BMC	aBMD	T-score	
Actual	Analyzed	(cm^2)	(g)	(g/cm^2)	Analyzed	Actual
T11	L1	12.70	13.51	1.064	0.5	---
T12	L2	14.60	14.12	0.967	-1.2	---
L1	L3	15.28	14.60	0.956	-1.3	-0.5
L2	L4	16.85	16.59	0.985	-1.5	-1.0
T11-L2	L1-L4	59.42	58.83	0.990	-0.9	---

Lateral scan (A0713041V)

Levels		Area	BMC	aBMD	WA-BMD	T-score	
Actual	Analyzed	(cm^2)	(g)	(g/cm^2)	(g/cm^3)	Analyzed	Actual
T12	L2	12.16	7.93	0.652	0.189		---
L1	L3	12.77	8.72	0.683	0.195		---
L2	L4	13.33	10.08	0.756	0.213		
T11-L2	L1-L4	38.26	26.74	0.699	0.200		---

Spine ID = 56601015

Levels L1-L4
AP Scan (A08180418)

Levels	Area (cm^2)	BMC (g)	aBMD (g/cm^2)	T-score
L1	11.76	9.11	0.775	-1.4
L2	14.03	11.74	0.837	-1.7
L3	15.06	12.56	0.834	-2.3
L4	14.98	15.85	1.058	-0.5
L1-L4	55.82	49.26	0.883	-1.5

Lateral scan (A08180419)

Levels	Area (cm^2)	BMC (g)	aBMD (g/cm^2)	WA-BMD (g/cm^3)	T-score
L2	8.07	4.12	0.510	0.163	-3.4
L3	8.66	4.20	0.485	0.145	-4.2
L4	9.13	6.99	0.765	0.203	-0.9
L2-L4	25.86	15.31	0.592	0.174	-2.7

Levels T11-L2
AP Scan (A0818041B)

Levels		Area	BMC	aBMD	T-score	
Actual	Analyzed	(cm^2)	(g)	(g/cm^2)	Analyzed	Actual
T11	L1	10.59	8.09	0.764	-1.5	---
T12	L2	12.00	8.61	0.717	-2.8	---
L1	L3	12.32	9.26	0.752	-3.0	-1.6
L2	L4	13.79	11.60	0.841	-2.5	-1.7
T11-L2	L1-L4	48.69	37.56	0.771	-2.5	---

Lateral scan (A0818041C)

Levels		Area	BMC	aBMD	WA-BMD	T-score	
Actual	Analyzed	(cm^2)	(g)	(g/cm^2)	(g/cm^3)	Analyzed	Actual
T12	L2	8.43	4.06	0.481	0.165	-3.7	---
L1	L3	8.30	4.28	0.516	0.177	-3.8	---
L2	L4	9.06	4.65	0.513	0.162	-3.5	-3.4
T11-L2	L1-L4	25.79	12.99	0.503	0.168	-3.8	---

Spine ID = 56601394

Levels L1-L4

AP Scan (A0818041I)

Levels	Area (cm^2)	BMC (g)	aBMD (g/cm^2)	T-score
L1	14.43	12.96	0.898	-1.0
L2	17.18	17.74	1.033	-0.6
L3	17.40	18.06	1.038	-0.6
L4	19.35	19.85	1.026	-1.1
L1-L4	68.35	68.62	1.004	-0.8

Lateral scan (A0818041J)

Levels	Area (cm^2)	BMC (g)	aBMD (g/cm^2)	WA-BMD (g/cm^3)	T-score
L2	15.84	11.48	0.724	0.184	
L3	13.43	11.70	0.871	0.206	
L4	16.51	12.56	0.761	0.177	
L2-L4	45.79	35.73	0.780	0.188	

Levels T11-L2

AP Scan (A0818041K)

Levels		Area (cm^2)	BMC (g)	aBMD (g/cm^2)	T-score	
Actual	Analyzed				Analyzed	Actual
T11	L1	12.68	10.18	0.803	-1.9	---
T12	L2	16.03	12.50	0.780	-2.9	---
L1	L3	14.80	13.34	0.901	-1.8	-1.0
L2	L4	17.16	18.01	1.050	-0.9	-0.4
T11-L2	L1-L4	60.66	54.03	0.891	-1.8	---

Lateral scan (A0818041L)

Levels		Area (cm^2)	BMC (g)	aBMD (g/cm^2)	WA-BMD (g/cm^3)	T-score	
Actual	Analyzed					Analyzed	Actual
T12	L2	12.51	7.14	0.571	0.165		---
L1	L3	14.63	9.80	0.670	0.192		---
L2	L4	14.00	13.01	0.930	0.223		
T11-L2	L1-L4	41.14	29.96	0.728	0.197		---

Spine ID = 56801530

Levels L1-L4

AP Scan (A0818041D)

Levels	Area (cm^2)	BMC (g)	aBMD (g/cm^2)	T-score
L1	16.06	13.18	0.821	-1.7
L2	17.32	15.02	0.867	-2.1
L3	18.04	15.89	0.881	-2.0
L4	20.38	17.17	0.843	-2.7
L1-L4	71.78	61.25	0.853	-2.2

Lateral scan (A0818041E)

Levels	Area (cm^2)	BMC (g)	aBMD (g/cm^2)	WA-BMD (g/cm^3)	T-score
L2	13.33	8.55	0.642	0.185	
L3	13.38	10.03	0.750	0.208	
L4	13.91	11.13	0.800	0.207	
L2-L4	40.61	29.71	0.732	0.200	

Levels T11-L2

AP Scan (A0818041F)

Levels		Area	BMC	aBMD	T-score	
Actual	Analyzed	(cm^2)	(g)	(g/cm^2)	Analyzed	Actual
T11	L1	13.60	10.49	0.771	-2.2	---
T12	L2	15.49	10.78	0.696	-3.6	---
L1	L3	16.79	13.39	0.798	-2.8	-1.9
L2	L4	17.06	14.94	0.876	-2.4	-2.0
T11-L2	L1-L4	62.93	49.59	0.788	-2.8	---

Lateral scan (A0818041G)

Levels		Area	BMC	aBMD	WA-BMD	T-score	
Actual	Analyzed	(cm^2)	(g)	(g/cm^2)	(g/cm^3)	Analyzed	Actual
T12	L2	10.87	5.78	0.532	0.154		---
L1	L3	11.95	6.84	0.573	0.166		---
L2	L4	12.02	9.44	0.786	0.225		
T11-L2	L1-L4	34.83	22.06	0.633	0.183		---

Clinical DXA Scans – Institute for Human Performance

Hologic QDR 4500W S/N 47730W
AP lumbar spine scans in fast array mode

Spine ID = 7753

Levels L1-L4
AP Scan (C09060605)

Levels	Area (cm^2)	BMC (g)	aBMD (g/cm^2)	T-score
L1	13.36	13.14	0.984	0.5
L2	13.54	14.56	1.076	0.4
L3	14.27	16.87	1.182	0.9
L4	16.32	18.89	1.157	0.4
L1-L4	57.48	63.46	1.104	0.5

Levels T11-L2
AP Scan (C09060606)

Levels		Area	BMC	aBMD	T-score	
Actual	Analyzed	(cm^2)	(g)	(g/cm^2)	Analyzed	Actual
T11	L1	10.03	9.89	0.986	0.6	---
T12	L2	11.87	10.82	0.912	-1.1	---
L1	L3	13.33	13.11	0.983	-0.9	0.5
L2	L4	13.62	14.69	1.079	-0.3	0.4
T11-L2	L1-L4	48.85	48.52	0.993	-0.5	---

Spine ID = 7912

Levels L1-L4
AP Scan (C09080604)

Levels	Area (cm^2)	BMC (g)	aBMD (g/cm^2)	T-score
L1	6.96	3.43	0.493	-3.9
L2	5.40	2.35	0.435	-5.4
L3	6.15	2.92	0.475	-5.5
L4	7.21	3.46	0.480	-5.8
L1-L4	25.73	12.17	0.473	-5.2

Levels T11-L2
AP Scan (C09080605)

Levels		Area	BMC	aBMD	T-score	
Actual	Analyzed	(cm^2)	(g)	(g/cm^2)	Analyzed	Actual
T11	L1	7.70	3.69	0.479	-4.1	---
T12	L2	6.00	2.88	0.480	-5.0	---
L1	L3	6.85	3.29	0.480	-5.5	-4.0
L2	L4	5.53	2.41	0.436	-6.2	-5.4
T11-L2	L1-L4	26.08	12.27	0.471	-5.2	---

Spine ID = 7741

Levels L1-L4
AP Scan (C0906060H)

Levels	Area (cm^2)	BMC (g)	aBMD (g/cm^2)	T-score
L1	14.95	10.56	0.707	-2.7
L2	16.38	13.10	0.800	-2.7
L3	16.66	15.03	0.903	-1.8
L4	19.86	18.14	0.913	-2.1
L1-L4	67.85	56.84	0.838	-2.3

Levels T11-L2
AP Scan (C0906060I)

Levels		Area	BMC	aBMD	T-score	
Actual	Analyzed	(cm^2)	(g)	(g/cm^2)	Analyzed	Actual
T11	L1	11.98	10.30	0.860	-1.4	---
T12	L2	14.40	11.75	0.816	-2.5	---
L1	L3	15.10	10.59	0.702	-3.7	-2.8
L2	L4	16.67	13.33	0.800	-3.1	-2.7
T11-L2	L1-L4	58.14	45.98	0.791	-2.7	---

Spine ID = 8092

Levels L1-L4
AP Scan (C0906060D)

Levels	Area (cm^2)	BMC (g)	aBMD (g/cm^2)	T-score
L1	15.34	13.16	0.858	-1.4
L2	16.57	16.31	0.984	-1.0
L3	18.24	16.95	0.930	-1.6
L4	16.81	18.16	1.080	-0.6
L1-L4	66.96	64.58	0.964	-1.2

Levels T11-L2
AP Scan (C0906060E)

Levels		Area	BMC	aBMD	T-score	
Actual	Analyzed	(cm^2)	(g)	(g/cm^2)	Analyzed	Actual
T11	L1	11.93	9.61	0.806	-1.8	---
T12	L2	14.07	11.38	0.809	-2.6	---
L1	L3	15.92	13.40	0.842	-2.4	-1.5
L2	L4	16.06	15.83	0.986	-1.5	-1.0
T11-L2	L1-L4	57.98	50.22	0.866	-2.0	---

Spine ID = 8219

Levels L1-L4
AP Scan (C09080608)

Levels	Area (cm^2)	BMC (g)	aBMD (g/cm^2)	T-score
L1	17.27	13.97	0.809	-1.8
L2	16.07	14.17	0.882	-1.9
L3	17.68	16.41	0.928	-1.6
L4	21.44	20.95	0.977	-1.5
L1-L4	72.46	65.49	0.904	-1.7

Levels T11-L2
AP Scan (C09080609)

Levels		Area	BMC	aBMD	T-score	
Actual	Analyzed	(cm^2)	(g)	(g/cm^2)	Analyzed	Actual
T11	L1	13.38	12.32	0.921	-0.8	---
T12	L2	14.40	11.47	0.797	-2.7	---
L1	L3	16.94	13.76	0.812	-2.6	-1.8
L2	L4	16.23	14.32	0.882	-2.4	-1.9
T11-L2	L1-L4	60.95	51.88	0.851	-2.2	---

Spine ID = 7885

Levels L1-L4
AP Scan (C0908060C)

Levels	Area (cm^2)	BMC (g)	aBMD (g/cm^2)	T-score
L1	17.81	21.70	1.218	1.9
L2	18.38	19.41	1.056	-0.4
L3	20.00	22.66	1.133	0.3
L4	23.64	24.73	1.046	-0.9
L1-L4	79.84	88.51	1.109	0.2

Levels T11-L2
AP Scan (C0908060D)

Levels		Area	BMC	aBMD	T-score	
Actual	Analyzed	(cm^2)	(g)	(g/cm^2)	Analyzed	Actual
T11	L1	14.78	20.59	1.393	3.5	---
T12	L2	16.83	17.83	1.060	-0.3	---
L1	L3	17.84	21.89	1.227	1.1	2.0
L2	L4	18.22	19.47	1.069	-0.7	-0.2
T11-L2	L1-L4	67.68	79.79	1.179	0.8	---

Spine ID = 7880

Levels L1-L4
AP Scan (C09060609)

Levels	Area (cm^2)	BMC (g)	aBMD (g/cm^2)	T-score
L1	12.21	7.25	0.593	-3.0
L2	13.26	8.40	0.634	-3.6
L3	14.32	8.60	0.601	-4.4
L4	14.77	9.44	0.639	-4.3
L1-L4	54.57	33.69	0.617	-3.9

Levels T11-L2
AP Scan (C0906060A)

Levels		Area	BMC	aBMD	T-score	
Actual	Analyzed	(cm^2)	(g)	(g/cm^2)	Analyzed	Actual
T11	L1	8.94	5.29	0.592	-3.0	---
T12	L2	10.92	5.84	0.535	-4.5	---
L1	L3	12.25	7.26	0.592	-4.5	-3.0
L2	L4	12.64	7.95	0.629	-4.4	-3.6
T11-L2	L1-L4	44.75	26.34	0.589	-4.2	---

Spine ID = 6062234

Levels L1-L4

AP Scan (A0929060B)

Levels	Area (cm^2)	BMC (g)	aBMD (g/cm^2)	T-score
L1	10.35	5.59	0.540	-3.5
L2	12.72	7.06	0.555	-4.3
L3	12.45	6.77	0.544	-4.9
L4	11.56	7.25	0.627	-4.4
L1-L4	47.09	26.67	0.566	-4.4

Lateral scan (A0929060C)

Levels	Area (cm^2)	BMC (g)	aBMD (g/cm^2)	WA-BMD (g/cm^3)	T-score
L2	7.78	3.09	0.396		-4.5
L3	8.44	3.46	0.410		-5.0
L4	9.05	3.82	0.422		-4.4
L2-L4	25.27	10.37	0.410		-4.9

Levels T11-L2

AP Scan (A09290607)

Levels		Area	BMC	aBMD	T-score	
Actual	Analyzed	(cm^2)	(g)	(g/cm^2)	Analyzed	Actual
T11	L1	9.86	5.41	0.549	-3.4	---
T12	L2	10.31	5.02	0.487	-4.9	---
L1	L3	9.72	5.32	0.547	-4.9	-3.4
L2	L4	11.15	6.42	0.576	-4.9	-4.1
T11-L2	L1-L4	41.04	54.03	0.540	-4.6	---

Lateral scan (A09290608)

Levels		Area	BMC	aBMD	WA-BMD	T-score	
Actual	Analyzed	(cm^2)	(g)	(g/cm^2)	(g/cm^3)	Analyzed	Actual
T12	L2	8.31	3.47	0.418		-4.3	---
L1	L3	6.96	2.82	0.406		-5.1	---
L2	L4	8.40	3.72	0.443		-4.2	-4.1
T11-L2	L1-L4	23.68	10.02	0.423		-4.7	---

MicroCT Reconstruction and Analysis Parameters

Resolution: 0.011605 mm C02-C10; 0.011616 mm C11-C29; 0.016970 mm C30-C37

Core	COR	Calibration (HU)			Mid-Region VOI (~8mm)		Threshold	
ID		Air	Water	Bone	Origin	Size	HU	g/cc
C02	1150	1.40	4.38	4955	(727,763,935)	(780,850,695)	1875	1.057
C03	650	1.36	4.54	4620	(243,172,928)	(830,830,700)	1547	1.050
C04	648	1.49	5.23	3435	(216,157,891)	(805,855,700)	981	1.043
C06	650	1.59	5.51	3247	(277,274,946)	(810,810,700)	966	1.045
C07	650	1.63	5.71	3105	(250,188,886)	(805,805,700)	921	1.044
C08	650	1.57	5.50	3264	(219,177,866)	(850,830,700)	1043	1.048
C09	650	1.53	5.52	3225	(202,232,935)	(790,820,700)	945	1.044
C10	650	1.57	5.57	3236	(116,187,916)	(995,930,700)	981	1.045
C11	648.5	1.66	5.63	3197	(177,219,941)	(825,845,695)	1078	1.051
C12	648.5	1.70	5.80	2996	(170,245,852)	(915,820,700)	917	1.046
C13	648.5	1.64	5.11	3899	(211,298,930)	(795,805,695)	1357	1.052
C14	648	1.74	5.88	3007	(196,158,905)	(890,900,695)	1819	1.091
C15	647	1.66	5.74	3042	(191,193,911)	(840,860,700)	1005	1.050
C16	647	1.80	5.90	3018	(223,150,906)	(880,860,700)	944	1.047
C17	647	1.63	5.50	3308	(180,243,919)	(830,810,700)	1073	1.049
C18	647	1.76	5.73	3185	(293,255,930)	(835,840,700)	1060	1.050
C20	647	1.55	5.37	3450	(150,267,900)	(815,805,695)	1159	1.050
C21	648.5	1.70	5.79	3063	(194,190,887)	(930,925,695)	1005	1.049
C22	648.5	1.47	5.25	3587	(170,162,926)	(840,875,700)	1343	1.056
C23	647	1.71	5.74	3150	(170,326,920)	(810,795,695)	1141	1.054
C24	647	1.63	5.58	3285	(182,187,891)	(835,805,700)	1181	1.054
C25	647	1.74	5.91	3010	(218,291,932)	(875,840,700)	1080	1.054
C26	647	1.81	5.63	3416	(333,236,970)	(825,830,700)	1169	1.051
C27	647	1.74	5.77	3202	(307,286,1017)	(825,870,695)	1060	1.050
C28	647	1.70	5.71	3229	(267,139,978)	(850,890,695)	1158	1.054
C29	647	1.78	5.86	3196	(314,185,1000)	(820,925,695)	1156	1.054
C30T	1137	1.95	5.83	3847	(621,531,761)	(600,555,485)	1045	1.041
C30L	1137	1.95	5.83	3847	(1181,906,681)	(635,610,480)	1113	1.043
C31T	1138	1.99	5.91	3774	(486,1041,976)	(630,580,485)	1034	1.041
C31L	1138	1.99	5.91	3774	(1241,1021,921)	(550,620,500)	981	1.039
C32T	1138	2.10	5.90	3787	(1126,1116,986)	(575,590,480)	1157	1.046
C32L	1138	2.10	5.90	3787	(706,511,901)	(640,620,505)	1038	1.041
C33T	1138	2.20	5.74	4305	(1256,926,856)	(630,585,485)	1169	1.041
C33L	1138	2.20	5.74	4305	(596,541,796)	(595,550,505)	1269	1.044
C34T	1138	1.87	5.67	3946	(676,466,791)	(590,580,505)	1185	1.045
C34L	1137	1.87	5.67	3946	(901,1136,711)	(595,630,505)	1257	1.048
C35T	1138	1.96	5.74	3905	(1207,852,848)	(530,555,485)	1282	1.049
C35L	1138	1.96	5.74	3905	(481,771.711)	(560,600,505)	1221	1.047
C36T	1138	2.07	5.66	4354	(636,1201,801)	(585,590,505)	1054	1.036
C36L	1138	2.07	5.66	4354	(1096,581,781)	(615,610,505)	1155	1.040
C37T	1138	1.95	5.90	3891	(661,561,811)	(625,560,505)	1136	1.044
C37L	1138	1.95	5.90	3891	(771,1246,701)	(560,580,500)	1129	1.044

MicroCT Mass and Architecture Measurements

Core ID		BV/TV		TMC (g)		TMD (g/cc)	
T12	L2	T12	L2	T12	L2	T12	L2
C3	C2	9.22	11.21	0.0247	0.0333	0.6707	0.7434
C4	C6	9.49	8.26	0.0242	0.0226	0.6385	0.6856
C7	C8	8.30	6.91	0.0213	0.0188	0.6412	0.6819
C9	C10	8.12	10.38	0.0212	0.0285	0.6525	0.6863
C11	C12	9.44	10.04	0.0278	0.0274	0.7387	0.6844
C13	C14	9.76	12.39	0.0285	0.0578	0.7308	1.1669
C15	C16	10.00	9.99	0.0285	0.0280	0.7133	0.7020
C17	C18	10.33	11.30	0.0280	0.0317	0.6782	0.7020
C20	C21	9.15	12.07	0.0260	0.0337	0.7112	0.6979
C22	C23	15.79	14.23	0.0470	0.0421	0.7450	0.7413
C24	C25	13.29	11.86	0.0387	0.0366	0.7286	0.7730
C26	C27	10.56	11.18	0.0302	0.0323	0.7158	0.7224
C28	C29	9.50	10.56	0.0291	0.0322	0.7670	0.7625
C30T	C30L	19.32	20.41	0.0449	0.0492	0.5820	0.6038
C31T	C31L	8.03	7.25	0.0200	0.0168	0.6216	0.5810
C32T	C32L	15.25	11.79	0.0368	0.0269	0.6047	0.5717
C33T	C33L	12.63	13.24	0.0275	0.0305	0.5448	0.5761
C34T	C34L	10.86	13.01	0.0254	0.0314	0.5857	0.6041
C35T	C35L	14.75	13.82	0.0355	0.0331	0.6028	0.5994
C36T	C36L	9.71	11.23	0.0208	0.0260	0.5375	0.5799
C37T	C37L	11.07	11.07	0.0255	0.0251	0.5757	0.5677

Core ID		Tb.Th* (mm)		Tb.Sp* (mm)		SMI	
T12	L2	T12	L2	T12	L2	T12	L2
C3	C2	0.0994	0.1349	1.4187	1.6301	2.01	1.85
C4	C6	0.0953	0.1014	1.3099	1.4793	2.10	2.24
C7	C8	0.1016	0.0991	1.5664	1.5851	2.14	2.43
C9	C10	0.0917	0.0952	1.4586	1.3730	2.14	1.69
C11	C12	0.1178	0.1203	1.3467	1.5001	2.32	2.17
C13	C14	0.1219	0.1187	1.4356	1.3880	2.10	1.69
C15	C16	0.0882	0.0903	1.3993	1.3900	1.64	1.68
C17	C18	0.1206	0.1196	1.4424	1.2837	2.20	2.03
C20	C21	0.1056	0.1142	1.4704	1.4132	2.03	1.68
C22	C23	0.1313	0.1299	1.4036	1.4283	1.43	1.64
C24	C25	0.1206	0.1216	1.3202	1.3484	2.01	2.20
C26	C27	0.1045	0.1173	1.4101	1.3448	2.16	2.23
C28	C29	0.1479	0.1309	1.5907	1.4523	2.27	1.94
C30T	C30L	0.1063	0.1097	1.0641	1.0750	1.67	1.73
C31T	C31L	0.1247	0.1130	1.5327	1.3658	2.27	2.74
C32T	C32L	0.1047	0.0909	1.1069	1.1050	1.78	2.00
C33T	C33L	0.0925	0.0994	1.1558	1.1233	1.88	1.85

MicroCT Anisotropy Measurements

Core ID		MIL1 (mm)		MIL2 (mm)		MIL3 (mm)		DA	
T12	L2	T12	L2	T12	L2	T12	L2	T12	L2
C3	C2	0.204	0.264	0.154	0.189	0.133	0.169	0.350	0.358
C4	C6	0.189	0.215	0.138	0.180	0.124	0.144	0.344	0.330
C7	C8	0.227	0.184	0.160	0.151	0.132	0.136	0.421	0.261
C9	C10	0.186	0.202	0.144	0.159	0.138	0.151	0.258	0.252
C11	C12	0.226	0.242	0.180	0.181	0.163	0.159	0.279	0.342
C13	C14	0.227	0.219	0.167	0.180	0.155	0.150	0.318	0.315
C15	C16	0.204	0.205	0.131	0.160	0.125	0.137	0.387	0.330
C17	C18	0.198	0.226	0.183	0.176	0.179	0.152	0.098	0.326
C20	C21	0.226	0.225	0.152	0.175	0.139	0.154	0.384	0.314
C22	C23	0.245	0.221	0.211	0.205	0.187	0.172	0.238	0.225
C24	C25	0.251	0.230	0.197	0.205	0.161	0.184	0.360	0.198
C26	C27	0.215	0.194	0.162	0.187	0.149	0.155	0.306	0.204
C28	C29	0.241	0.253	0.209	0.199	0.198	0.180	0.179	0.290
C30T	C30L	0.202	0.211	0.168	0.179	0.163	0.168	0.193	0.204
C31T	C31L	0.220	0.193	0.173	0.166	0.165	0.154	0.248	0.202
C32T	C32L	0.179	0.180	0.149	0.148	0.148	0.137	0.169	0.237
C33T	C33L	0.195	0.195	0.147	0.146	0.142	0.138	0.275	0.289
C34T	C34L	0.187	0.209	0.149	0.177	0.143	0.150	0.237	0.280
C35T	C35L	0.190	0.193	0.170	0.167	0.169	0.142	0.109	0.262
C36T	C36L	0.149	0.198	0.133	0.167	0.127	0.162	0.153	0.184
C37T	C37L	0.185	0.194	0.159	0.172	0.151	0.164	0.184	0.154

Core ID		Aniso13		Aniso12		Aniso23	
T12	L2	T12	L2	T12	L2	T12	L2
C3	C2	1.54	1.56	1.32	1.39	1.16	1.12
C4	C6	1.52	1.49	1.37	1.19	1.11	1.25
C7	C8	1.73	1.35	1.42	1.22	1.21	1.11
C9	C10	1.35	1.34	1.29	1.28	1.04	1.05
C11	C12	1.39	1.52	1.26	1.33	1.10	1.14
C13	C14	1.47	1.46	1.36	1.22	1.08	1.19
C15	C16	1.63	1.49	1.55	1.28	1.05	1.17
C17	C18	1.11	1.48	1.08	1.28	1.03	1.16
C20	C21	1.62	1.46	1.49	1.29	1.09	1.13
C22	C23	1.31	1.29	1.16	1.08	1.13	1.20
C24	C25	1.56	1.25	1.28	1.12	1.22	1.11
C26	C27	1.44	1.26	1.32	1.04	1.09	1.21
C28	C29	1.22	1.41	1.15	1.27	1.06	1.11
C30T	C30L	1.24	1.26	1.20	1.18	1.03	1.07
C31T	C31L	1.33	1.25	1.27	1.16	1.05	1.08
C32T	C32L	1.20	1.31	1.20	1.21	1.01	1.08
C33T	C33L	1.38	1.41	1.33	1.33	1.03	1.06
C34T	C34L	1.31	1.39	1.26	1.18	1.04	1.18
C35T	C35L	1.12	1.36	1.11	1.16	1.01	1.17
C36T	C36L	1.18	1.23	1.12	1.19	1.05	1.03
C37T	C37L	1.23	1.18	1.16	1.12	1.05	1.05

Endcapping Vertebral Trabecular Cores

Core ID	Subject ID	Level	Mass (g)		Length (mm)	
			Pre Jet	Post Jet	Core	Exposed
C02	56601009	L2	0.657	0.631	25.49	11.77
C03	56601009	T12	0.623	0.659	24.50	13.78
C04	57400992	T12	0.841	0.750	22.12	11.78
C06	57400992	L2	0.953	0.831	25.23	12.48
C07	56601150	T12	0.787	0.614	22.65	12.10
C08	56601150	L2	0.768	0.618	23.66	11.25
C09	57100905	T12	0.542	0.571	23.58	11.55
C10	57100905	L2	0.858	0.726	24.39	12.49
C11	56601148	T12	0.783	0.701	21.14	11.39
C12	56601148	L2	0.860	0.764	22.44	12.20
C13	51000686	T12	1.222	0.989	23.47	13.73
C14	51000686	L2	1.205	1.094	24.19	11.98
C15	OH04020204	T12	0.858	0.903	23.27	12.83
C16	OH04020204	L2	0.872	0.788	23.52	11.61
C17	57401177	T12	1.018	0.794	26.24	12.42
C18	57401177	L2	1.150	0.847	26.99	13.15
C20	56601390	T12	0.934	0.632	23.78	12.08
C21	56601390	L2	1.102	1.161	23.62	12.56
C22	56601076	T12	1.124	0.784	25.69	12.65
C23	56601076	L2	0.961	0.736	24.68	11.57
C24	56601015	T12	0.996	0.886	25.08	12.72
C25	56601015	L2	1.088	0.917	24.68	12.67
C26	56601394	T12	0.694	0.695	27.48	12.71
C27	56601394	L2	0.740	0.842	28.32	12.12
C28	56801530	T12	0.962	0.844	25.87	12.81
C29	56801530	L2	1.043	0.977	27.05	12.64
C30T	7753	T12	0.863	0.920	21.79	12.27
C30L	7753	L2	1.199	0.892	24.87	12.90
C31T	7912	L2	0.531	0.396	22.42	10.07
C31L	7912	T12	0.733	0.360	20.12	8.48
C32T	7741	L2	0.850	0.685	26.39	12.46
C32L	7741	T12	0.853	0.560	21.82	10.00
C33T	8092	T12	1.094	0.909	21.75	10.39
C33L	8092	L2	1.227	0.950	23.50	11.30
C34T	8219	T12	1.199	0.807	23.81	10.69
C34L	8219	L2	1.324	0.992	26.59	12.87
C35T	7885	T12	0.890	0.480	20.51	7.91
C35L	7885	L2	1.167	0.830	24.11	10.48
C36T	7880	L2	0.740	0.479	23.80	9.76
C36L	7880	T12	0.750	0.448	21.87	10.69
C37T	6062234	T12	0.890	0.577	18.70	9.09
C37L	6062234	L2	1.033	0.685	21.14	10.63

Mechanical Testing Parameters for Trabecular Cores

Core ID	Test Order	Diameter (mm)	Effective GL (mm)	Displacement (mm)		Strain rate (mm/min)
				Preload	Load	
C02	27	8.18	18.63	0.0186	0.5588	5.588
C03	4	8.15	19.14	0.0191	0.5741	5.741
C04	16	8.16	16.95	0.0169	0.5084	5.084
C06	26	8.11	18.85	0.0189	0.5656	5.656
C07	10	8.04	17.37	0.0174	0.5212	5.212
C08	12	8.10	17.45	0.0175	0.5236	5.236
C09	1	8.12	17.56	0.0176	0.5269	5.269
C10	25	8.21	18.44	0.0184	0.5531	5.531
C11	11	8.14	16.26	0.0163	0.4879	4.879
C12	13	8.21	17.32	0.0173	0.5195	5.195
C13	5	8.17	18.60	0.0186	0.5580	5.580
C14	6	8.19	18.09	0.0181	0.5426	5.426
C15	3	8.17	18.05	0.0180	0.5414	5.414
C16	17	8.19	17.56	0.0176	0.5269	5.269
C17	2	8.19	19.33	0.0193	0.5799	5.799
C18	15	8.17	20.07	0.0201	0.6020	6.020
C20	24	8.15	17.93	0.0179	0.5378	5.378
C21	23	8.19	18.09	0.0181	0.5427	5.427
C22	18	8.17	19.17	0.0192	0.5751	5.751
C23	20	8.18	18.12	0.0181	0.5437	5.437
C24	21	8.17	18.90	0.0189	0.5669	5.669
C25	19	8.19	18.67	0.0187	0.5602	5.602
C26	14	8.13	20.10	0.0201	0.6029	6.029
C27	22	8.15	20.22	0.0202	0.6065	6.065
C28	9	8.18	19.34	0.0193	0.5802	5.802
C29	8	8.23	19.84	0.0198	0.5953	5.953
C30T	28	8.20	17.03	0.0170	0.5109	5.109
C30L	38	8.19	18.89	0.0189	0.5666	5.666
C31T	39	8.15	16.24	0.0162	0.4872	4.872
C31L	33	8.11	14.30	0.0143	0.4289	4.289
C32T	29	8.13	19.42	0.0194	0.5827	5.827
C32L	31	8.10	15.91	0.0159	0.4773	4.773
C33T	40	8.17	16.07	0.0161	0.4821	4.821
C33L	32	8.17	17.40	0.0174	0.5219	5.219
C34T	41	8.15	17.25	0.0173	0.5176	5.176
C34L	36	8.20	19.73	0.0197	0.5920	5.920
C35T	35	8.14	14.21	0.0142	0.4263	4.263
C35L	43	8.18	17.30	0.0173	0.5189	5.189
C36T	42	8.09	16.78	0.0168	0.5034	5.034
C36L	30	7.89	16.28	0.0163	0.4884	4.884
C37T	34	8.16	13.89	0.0139	0.4167	4.167
C37L	37	8.19	15.88	0.0159	0.4765	4.765

Mechanical Testing Apparent Material Properties

Core ID	Subject ID	Level	E (MPa)	σ_Y (MPa)	σ_u (MPa)	ε_Y (%)	ε_Y (%)
C02	56601009	L2	604.2	2.466	2.511	0.6080	0.7074
C03	56601009	T12	282.2	1.030	1.062	0.5650	0.7380
C04	57400992	T12	454.7	1.865	1.986	0.6100	0.9040
C06	57400992	L2	447.9	1.631	1.632	0.5640	0.5566
C07	56601150	T12	365.9	1.297	1.350	0.5550	0.6784
C08	56601150	L2	404.8	1.572	1.591	0.5880	0.6326
C09	57100905	T12	116.9	0.808	1.057	0.8910	1.8465
C10	57100905	L2	428.8	1.403	1.402	0.5270	0.5296
C11	56601148	T12	595.5	2.806	2.903	0.6710	0.8214
C12	56601148	L2	588.3	2.191	2.195	0.5720	0.5502
C13	51000686	T12	555.5	2.201	2.269	0.5960	0.7595
C14	51000686	L2	662.0	2.626	2.763	0.5970	0.7876
C15	OH04020204	T12	376.1	1.820	2.132	0.6840	1.3606
C16	OH04020204	L2	469.5	2.011	2.093	0.6280	0.8593
C17	57401177	T12	391.4	1.644	1.741	0.6200	0.8497
C18	57401177	L2	551.6	2.130	2.142	0.5860	0.6341
C20	56601390	T12	508.7	2.024	2.142	0.5980	0.8332
C21	56601390	L2	843.8	3.227	3.472	0.5820	0.9828
C22	56601076	T12	626.7	2.754	2.920	0.6390	0.8981
C23	56601076	L2	484.7	1.565	1.585	0.5230	0.5836
C24	56601015	T12	929.5	3.107	3.224	0.5340	0.7042
C25	56601015	L2	727.3	3.108	3.189	0.6270	0.7521
C26	56601394	T12	624.1	2.447	2.474	0.5920	0.6876
C27	56601394	L2	342.0	1.265	1.268	0.5700	0.5829
C28	56801530	T12	699.4	3.006	3.270	0.6300	0.9753
C29	56801530	L2	766.5	3.211	3.820	0.6190	1.1967
C30T	7753	T12	952.9	3.871	4.394	0.6060	1.0588
C30L	7753	L2	808.0	3.350	3.680	0.6150	1.0155
C31T	7912	T12	423.4	1.558	1.645	0.5680	0.8066
C31L	7912	L2	195.7	0.745	0.862	0.5810	1.0141
C32T	7741	T12	324.7	0.912	0.937	0.4810	0.5786
C32L	7741	L2	351.8	1.080	1.095	0.5070	0.5852
C33T	8092	T12	580.8	2.203	2.265	0.5790	0.7090
C33L	8092	L2	547.3	1.892	1.980	0.5460	0.7517
C34T	8219	T12	707.1	2.752	2.865	0.5890	0.7508
C34L	8219	L2	482.0	1.677	1.786	0.5480	0.8021
C35T	7885	T12	826.7	2.674	2.678	0.5230	0.5431
C35L	7885	L2	595.4	2.240	2.490	0.5760	1.0232
C36T	7880	T12	112.5	0.370	0.418	0.5290	0.8775
C36L	7880	L2	167.9	0.507	0.654	0.5020	1.2737
C37T	6062234	T12	331.6	1.125	1.143	0.5390	0.5774
C37L	6062234	L2	289.9	0.885	0.906	0.5050	0.6285

MicroCT Tissue Mineral Distribution and Computed Tissue Modulus

Core ID	Tissue Mineral Density (HU/Bone HU)					
	Mean	Median	Min	Max	SD	COV %
C02	0.6516	0.6648	0.3784	1.0286	0.1483	22.8
C06	0.5835	0.5821	0.2975	1.0316	0.1717	29.4
C08	0.5816	0.5822	0.3196	0.9939	0.1554	26.7
C10	0.5762	0.5776	0.3032	1.0321	0.1598	27.7
C12	0.6020	0.5983	0.3061	1.1092	0.1780	29.6
C14	0.5961	0.5976	0.3003	1.0898	0.1729	29.0
C16	0.5928	0.5887	0.3128	1.1047	0.1681	28.4
C18	0.6082	0.6134	0.3328	1.0100	0.1574	25.9
C21	0.6042	0.6068	0.3281	1.0484	0.1598	26.5
C23	0.6481	0.6637	0.3622	1.0150	0.1542	23.8
C25	0.6652	0.6851	0.3588	1.0283	0.1644	24.7
C27	0.6172	0.6248	0.3310	1.0440	0.1630	26.4
C29	0.6624	0.6820	0.3617	1.0452	0.1584	23.9
C30L	0.5244	0.5169	0.2893	1.8288	0.1497	28.6
C31L	0.5137	0.4982	0.2599	1.0288	0.1670	32.5
C32L	0.4970	0.4770	0.2741	1.0293	0.1506	30.3
C33L	0.5075	0.4993	0.2948	0.9575	0.1339	26.4
C34L	0.5308	0.5289	0.3186	0.9663	0.1282	24.2
C35L	0.5211	0.5221	0.3127	0.9439	0.1236	23.7
C36L	0.5088	0.5058	0.2653	1.0058	0.1491	29.3
C37L	0.5023	0.4996	0.2902	0.9114	0.1297	25.8
	Heterogeneous Tissue Modulus (MPa)					
C02	13038	13303	7581	20572	2965	22.7
C06	11678	11647	5965	20632	3435	29.4
C08	11639	11651	6405	19877	3108	26.7
C10	11532	11559	6078	20641	3195	27.7
C12	12047	11968	6138	22183	3561	29.6
C14	11931	11959	6022	21796	3458	29.0
C16	11864	11783	6272	22093	3363	28.3
C18	12172	12277	6670	20200	3147	25.9
C21	12092	12137	6577	20968	3196	26.4
C23	12968	13276	7258	20299	3084	23.8
C25	13311	13710	7190	20566	3289	24.7
C27	12351	12510	6635	20880	3260	26.4
C29	13255	13645	7248	20904	3168	23.9
C30L	10496	10343	5802	36576	2994	28.5
C31L	10282	9966	5214	20575	3341	32.5
C32L	9948	9545	5497	20585	3013	30.3
C33L	10158	9991	5909	19150	2679	26.4
C34L	10622	10581	6384	19325	2563	24.1
C35L	10427	10445	6266	18879	2472	23.7
C36L	10183	10119	5320	20116	2983	29.3
C37L	10052	10002	5816	18227	2593	25.8

Finite Element Model Descriptions for L2 Specimens

Core ID	Materials	Elements	Nodes	DOF	CSA (mm)		Connected Regions	
					x-size	y-size	Groups	Vol (%)
C02	936	142467	262333	786999	8.2343	8.2343	399	98.8
C06	955	103260	212201	636603	8.2343	8.1662	719	97.4
C08	954	85821	182167	546501	8.2343	8.1662	516	96.9
C10	962	134069	273573	820719	8.1662	8.1662	442	99.0
C12	964	124966	243166	729498	8.2343	8.2343	287	99.3
C14	897	72191	165393	496179	8.1662	8.0982	1413	91.7
C16	943	127492	264645	793935	8.2343	8.2343	632	98.5
C18	966	141829	280783	842349	8.1662	8.1662	360	99.3
C21	954	153262	296798	890394	8.2343	8.1662	458	99.2
C23	981	179398	331641	994923	8.2343	8.2343	490	98.7
C25	983	149338	292403	877209	8.2343	8.2343	602	98.4
C27	968	140995	280784	842352	8.2343	8.2343	925	97.9
C29	960	132479	245772	737316	8.2343	8.2343	454	97.9
C30L	868	250557	461802	1385406	8.1662	8.1662	745	99.3
C31L	949	86376	175304	525912	8.1662	8.1662	597	96.7
C32L	889	142570	294363	883089	8.1662	8.1662	1021	97.3
C33L	948	162213	316555	949665	8.1662	8.1662	986	98.1
C34L	945	160561	311258	933774	8.1662	8.1662	590	99.1
C35L	917	178298	336849	1010547	8.1662	8.1662	598	98.8
C36L	891	133407	249878	749634	8.1662	8.1662	571	98.4
C37L	924	134222	265404	796212	8.1662	8.1662	648	98.1

FE Assigned Tissue Modulus and Predicted Apparent Modulus

Element size = 0.068 mm
Applied strain = -0.25%

Core	Tissue Modulus (GPa)			Apparent Modulus (GPa)		
ID	Homo	Hetero	SSHomo	Homo	Hetero	SSHomo
C02	20	13.0	13.0	0.8386	0.5505	0.5467
C06	20	11.7	11.7	0.4535	0.2667	0.2648
C08	20	11.6	11.6	0.3235	0.1904	0.1882
C10	20	11.5	11.5	0.5458	0.3179	0.3147
C12	20	12.0	12.0	0.6185	0.3819	0.3726
C14	20	11.9	11.9	0.1262	0.0937	0.0950
C16	20	11.9	11.9	0.5619	0.3376	0.3333
C18	20	12.2	12.2	0.6315	0.3812	0.3843
C21	20	12.1	12.1	0.7896	0.4829	0.4774
C23	20	13.0	13.0	0.6536	0.4139	0.4238
C25	20	13.3	13.3	0.5766	0.3863	0.3838
C27	20	12.4	12.4	0.3809	0.2283	0.2352
C29	20	13.3	13.3	0.7439	0.5084	0.4930
C30L	20	10.5	10.5	1.5023	0.7931	0.7890
C31L	20	10.3	10.3	0.2996	0.1567	0.1540
C32L	20	9.9	9.9	0.5515	0.2705	0.2743
C33L	20	10.2	10.2	0.8076	0.4094	0.4102
C34L	20	10.6	10.6	0.8234	0.4478	0.4373
C35L	20	10.4	10.4	0.8673	0.4541	0.4522
C36L	20	10.2	10.2	0.6072	0.3096	0.3092
C37L	20	10.1	10.1	0.3732	0.1818	0.1876
		(mean)	(mean)			

FE Minimum Principal Strains: Homogeneous Models

Analyzed over the middle 5mm of the 7mm core subsection modeled
Element size = 0.068 mm
Applied strain = -0.25%

Core	Analyzed	Minimum Principal Strain (microstrain)						Post-yield	
ID	Elements	Mean	Median	Min	Max	SD	COV %	#	%
C02	94978	-1083	-1003	-6359	0	726	-67.0	3	0.005
C06	68839	-799	-646	-7557	0	682	-85.3	32	0.034
C08	57214	-771	-564	-7314	7	697	-90.4	17	0.016
C10	89380	-803	-609	-7999	0	686	-85.5	33	0.031
C12	83311	-958	-816	-6842	21	724	-75.6	16	0.016
C14	48128	-404	-235	-5790	27	492	-121.8	7	0.007
C16	84995	-860	-706	-8998	2	667	-77.6	12	0.007
C18	94552	-840	-661	-6708	11	688	-81.9	46	0.038
C21	102175	-1030	-901	-7096	0	758	-73.6	5	0.009
C23	119599	-733	-537	-8573	1	658	-89.8	0	0.000
C25	99559	-879	-648	-8016	0	770	-87.6	9	0.011
C27	93996	-486	-321	-5762	0	490	-100.8	7	0.008
C29	88320	-1072	-938	-6401	0	811	-75.7	1	0.001
C30L	167040	-1086	-955	-8219	0	776	-71.5	2	0.002
C31L	57583	-742	-492	-6340	63	737	-99.3	4	0.004
C32L	95047	-758	-561	-6651	0	688	-90.7	1	0.001
C33L	108142	-888	-762	-7687	0	686	-77.3	7	0.008
C34L	107040	-1015	-869	-10520	0	753	-74.2	18	0.018
C35L	118865	-939	-804	-8736	0	706	-75.2	13	0.019
C36L	88938	-899	-683	-6831	1	767	-85.3	10	0.008
C37L	89481	-538	-340	-6786	83	558	-103.7	40	0.045

FE Minimum Principal Strains: Homogeneous Models

Analyzed over the middle 5mm of the 7mm core subsection modeled
Element size = 0.068 mm
Applied strain = -0.25%

Core	Low (< 500)		Middle (500-1000)		High (> 1500)	
ID	# elems	% elems	# elems	% elems	# elems	% elems
C02	23930	25.20	46417	48.87	24631	25.93
C06	28625	41.58	30695	44.59	9519	13.83
C08	26326	46.01	22618	39.53	8270	14.45
C10	38636	43.23	37142	41.56	13602	15.22
C12	27208	32.66	38985	46.79	17118	20.55
C14	57075	63.78	11171	23.21	8306	9.28
C16	31016	36.49	40853	48.07	13126	15.44
C18	37862	40.04	41777	44.18	14913	15.77
C21	30531	29.88	47019	46.02	24625	24.10
C23	56624	47.34	48985	40.96	13990	11.70
C25	41097	41.28	39984	40.16	18478	18.56
C27	60400	64.26	29432	31.31	4164	4.43
C29	27445	31.07	36106	40.88	24769	28.04
C30L	57075	63.78	75780	45.37	8306	9.28
C31L	29051	50.45	19921	34.60	8611	14.95
C32L	44094	46.39	37766	39.73	13187	13.87
C33L	38009	35.15	51698	47.81	18435	17.05
C34L	33524	31.32	47694	44.56	25822	24.12
C35L	40457	34.04	54235	45.63	24173	20.34
C36L	35715	40.16	35493	39.91	17730	19.94
C37L	55758	62.31	27522	30.76	6201	6.93

FE Minimum Principal Strains: Heterogeneous Models

Analyzed over the middle 5mm of the 7mm core subsection modeled
Element size = 0.068 mm
Applied strain = -0.25%

Core	Analyzed	Minimum Principal Strain (microstrain)						Post-yield	
ID	Elements	Mean	Median	Min	Max	SD	COV %	#	%
C02	94978	-1067	-969	-6024	0	731	-68.5	8	0.014
C06	68839	-797	-631	-7398	0	691	-86.7	46	0.048
C08	57214	-768	-557	-6403	21	704	-91.6	17	0.016
C10	89380	-807	-605	-8632	0	698	-86.4	52	0.048
C12	83311	-955	-805	-6024	4	724	-75.8	15	0.015
C14	48128	-402	-232	-6111	5	498	-123.9	10	0.011
C16	84995	-860	-700	-7507	0	674	-78.3	6	0.004
C18	94552	-837	-647	-6908	0	696	-83.1	59	0.049
C21	102175	-1022	-875	-8030	0	768	-75.1	4	0.007
C23	119599	-722	-515	-7978	2	671	-93.0	2	0.004
C25	99559	-878	-639	-8128	13	778	-88.6	6	0.007
C27	93996	-470	-304	-6492	0	489	-104.0	20	0.022
C29	88320	-1078	-932	-7416	0	820	-76.0	4	0.004
C30L	167040	-1074	-918	-9962	0	796	-74.2	0	0.000
C31L	57583	-732	-475	-7137	0	747	-102.0	10	0.011
C32L	95047	-750	-536	-8172	0	705	-94.0	3	0.003
C33L	108142	-873	-732	-9726	0	700	-80.2	6	0.007
C34L	107040	-1014	-870	-10257	0	749	-73.9	23	0.023
C35L	118865	-936	-791	-8357	0	712	-76.0	17	0.025
C36L	88938	-895	-661	-7181	0	782	-87.4	12	0.010
C37L	89481	-526	-324	-7169	59	559	-106.3	62	0.070

FE Minimum Principal Strains: Heterogeneous Models

Analyzed over the middle 5mm of the 7mm core subsection modeled
Element size = 0.068 mm
Applied strain = -0.25%

Core	Low (< 500)		Middle (500-1000)		High (> 1500)	
ID	# elems	% elems	# elems	% elems	# elems	% elems
C02	24326	25.61	47365	49.87	23287	24.52
C06	28847	41.91	30356	44.10	9636	14.00
C08	26573	46.44	22442	39.22	8199	14.33
C10	38828	43.44	36783	41.15	13769	15.41
C12	27183	32.63	39257	47.12	16871	20.25
C14	57075	63.78	10979	22.81	8306	9.28
C16	31142	36.64	40673	47.85	13180	15.51
C18	38543	40.76	41019	43.38	14990	15.85
C21	30856	30.20	47457	46.45	23862	23.35
C23	58552	48.96	47152	39.43	13895	11.62
C25	41462	41.65	39774	39.95	18323	18.40
C27	62283	66.26	27634	29.40	4079	4.34
C29	27379	31.00	36027	40.79	24914	28.21
C30L	57075	63.78	76377	45.72	8306	9.28
C31L	29659	51.51	19577	34.00	8347	14.50
C32L	45400	47.77	36700	38.61	12947	13.62
C33L	39532	36.56	50977	47.14	17633	16.31
C34L	33318	31.13	48130	44.96	25592	23.91
C35L	40985	34.48	53761	45.23	24119	20.29
C36L	36476	41.01	34918	39.26	17544	19.73
C37L	57075	63.78	26295	29.39	6111	6.83

APPENDIX B: Mechanical Testing Data Plots

Load-Displacement and Stress-Strain Plots

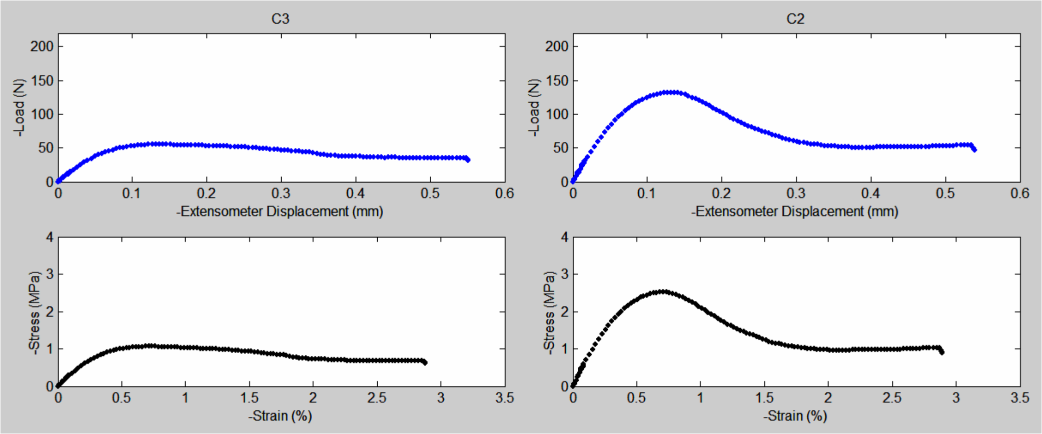

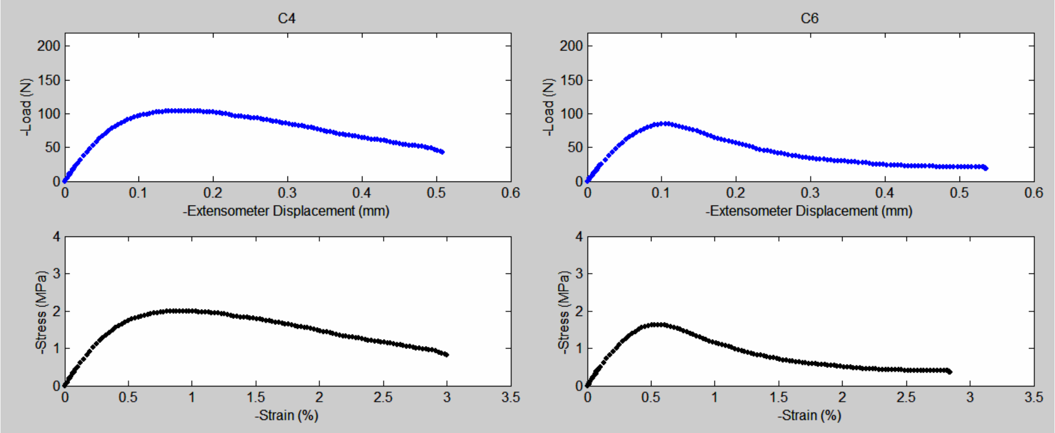

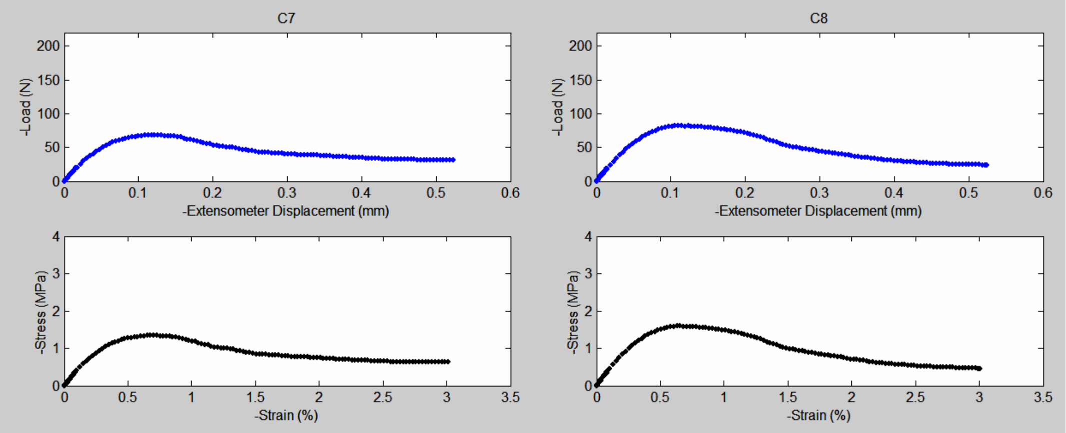

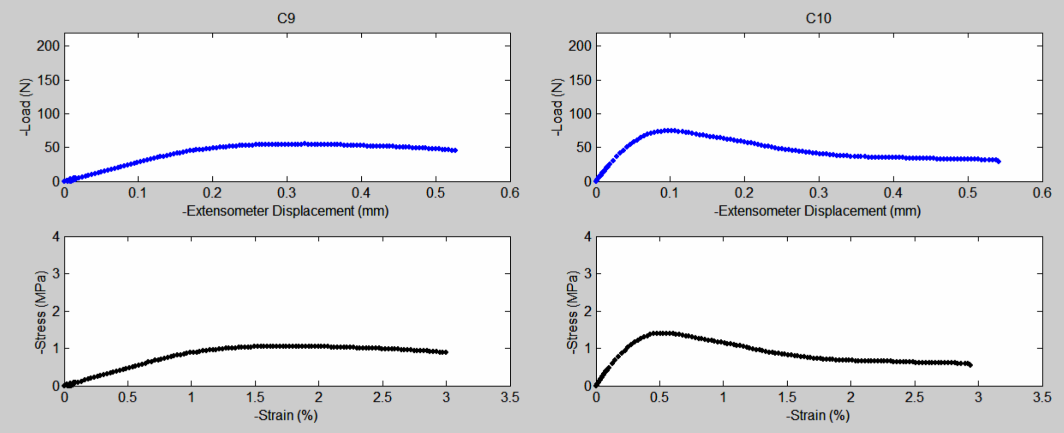
C9
C10
-Load (N)
0
50
100
150
200
0
0.1
0.2
0.3
0.4
0.5
0.6
-Extensometer Displacement (mm)
-Stress (MPa)
0
1
2
3
4
0
0.5
1
1.5
2
2.5
3
3.5
-Strain (%)

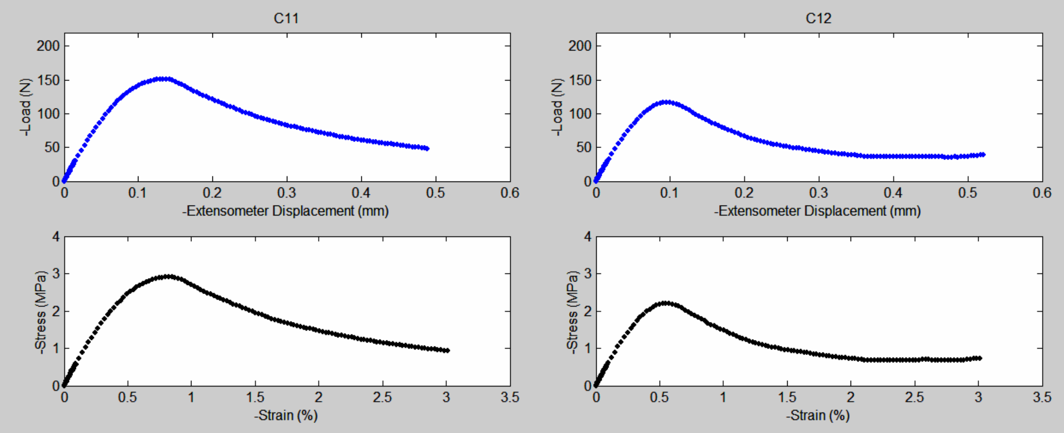
C11
C12
-Load (N)
0
50
100
150
200
0
0.1
0.2
0.3
0.4
0.5
0.6
-Extensometer Displacement (mm)
-Stress (MPa)
0
1
2
3
4
0
0.5
1
1.5
2
2.5
3
3.5
-Strain (%)

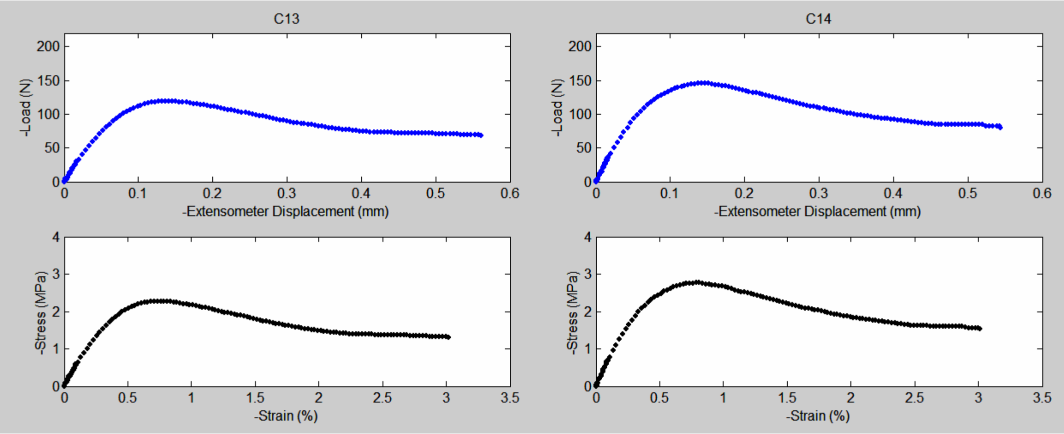
C13
C14
-Load (N)
0
50
100
150
200
0
0.1
0.2
0.3
0.4
0.5
0.6
-Extensometer Displacement (mm)
-Stress (MPa)
0
1
2
3
4
0
0.5
1
1.5
2
2.5
3
3.5
-Strain (%)

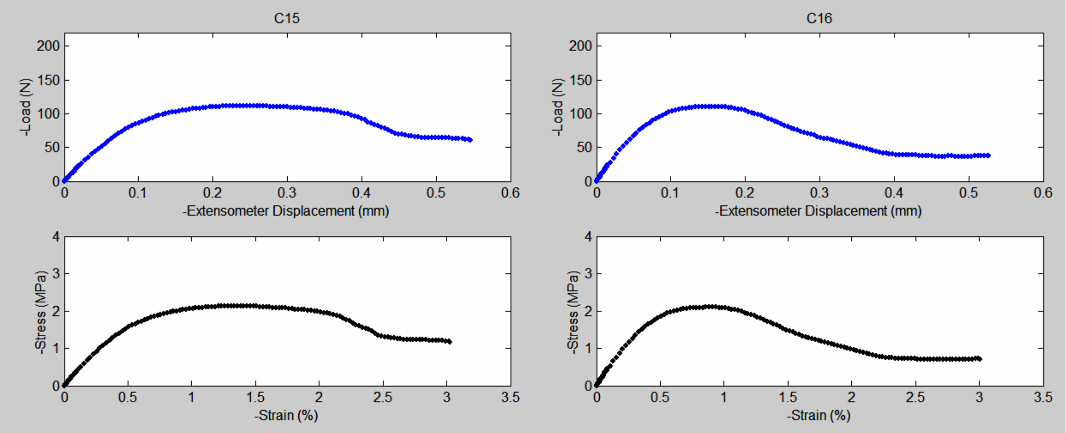
C15
-Load (N)
0
50
100
150
200
0
0.1
0.2
0.3
0.4
0.5
0.6
-Extensometer Displacement (mm)
-Stress (MPa)
0
1
2
3
4
0
0.5
1
1.5
2
2.5
3
3.5
-Strain (%)
C16
-Load (N)
-Extensometer Displacement (mm)
-Stress (MPa)
-Strain (%)

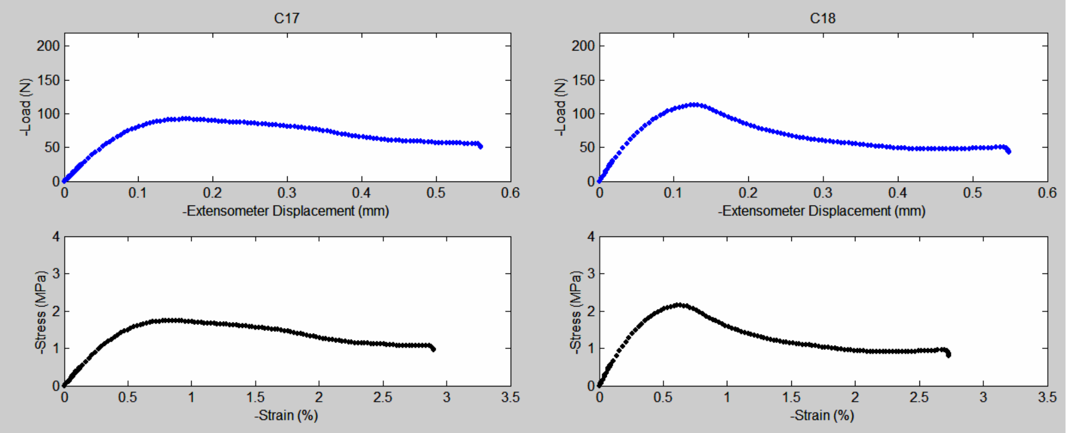
C17
-Load (N)
0
50
100
150
200
0
0.1
0.2
0.3
0.4
0.5
0.6
-Extensometer Displacement (mm)
-Stress (MPa)
0
1
2
3
4
0
0.5
1
1.5
2
2.5
3
3.5
-Strain (%)
C18
-Load (N)
-Extensometer Displacement (mm)
-Stress (MPa)
-Strain (%)

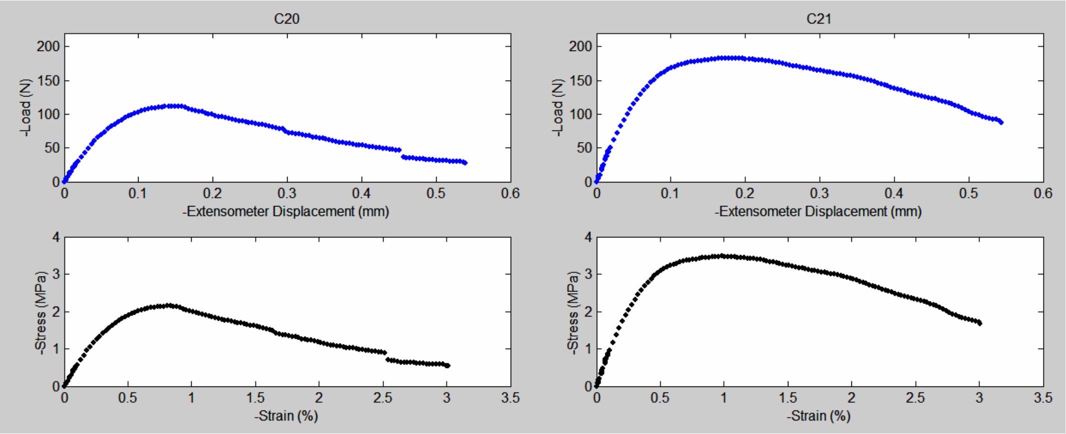
C20
-Load (N)
0
50
100
150
200
0
0.1
0.2
0.3
0.4
0.5
0.6
-Extensometer Displacement (mm)
-Stress (MPa)
0
1
2
3
4
0
0.5
1
1.5
2
2.5
3
3.5
-Strain (%)
C21
-Load (N)
-Extensometer Displacement (mm)
-Stress (MPa)
-Strain (%)

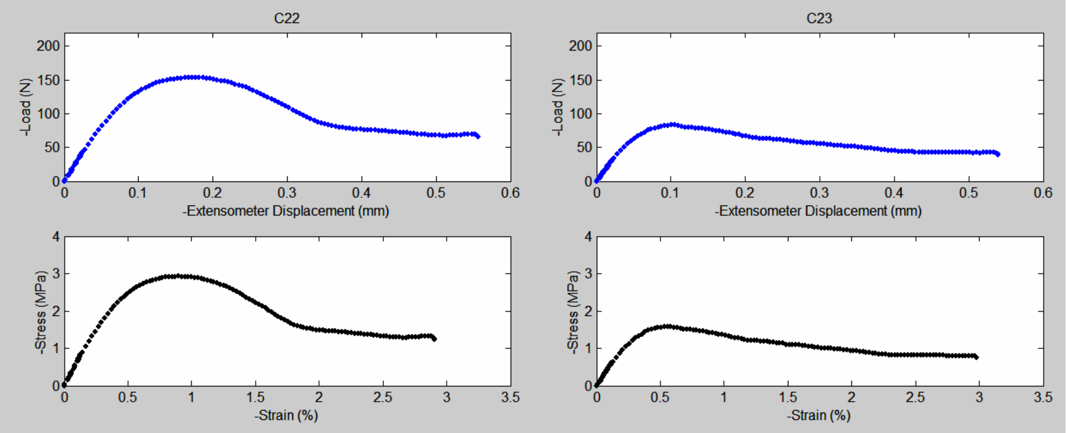
C22
C23
-Load (N)
0
50
100
150
200
0
0.1
0.2
0.3
0.4
0.5
0.6
-Extensometer Displacement (mm)
-Stress (MPa)
0
1
2
3
4
0
0.5
1
1.5
2
2.5
3
3.5
-Strain (%)

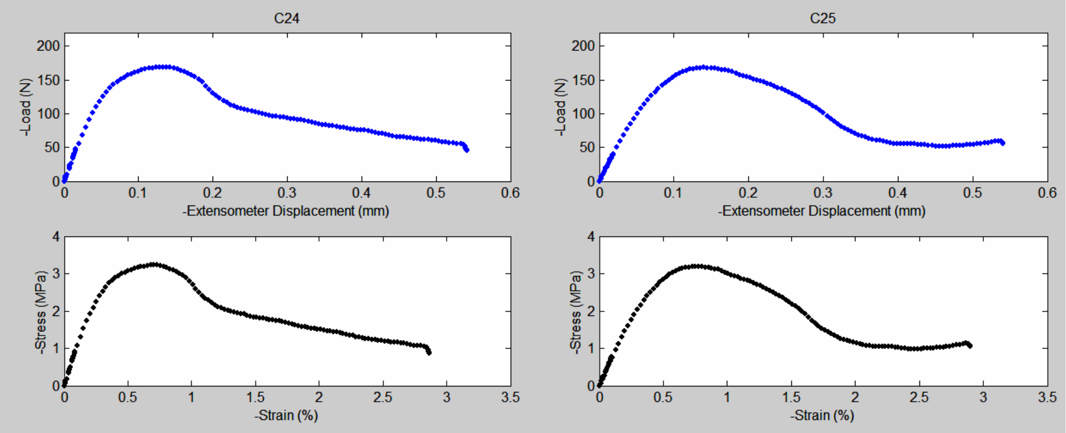
C24
C25
-Load (N)
0
50
100
150
200
0
0.1
0.2
0.3
0.4
0.5
0.6
-Extensometer Displacement (mm)
-Stress (MPa)
0
1
2
3
4
0
0.5
1
1.5
2
2.5
3
3.5
-Strain (%)

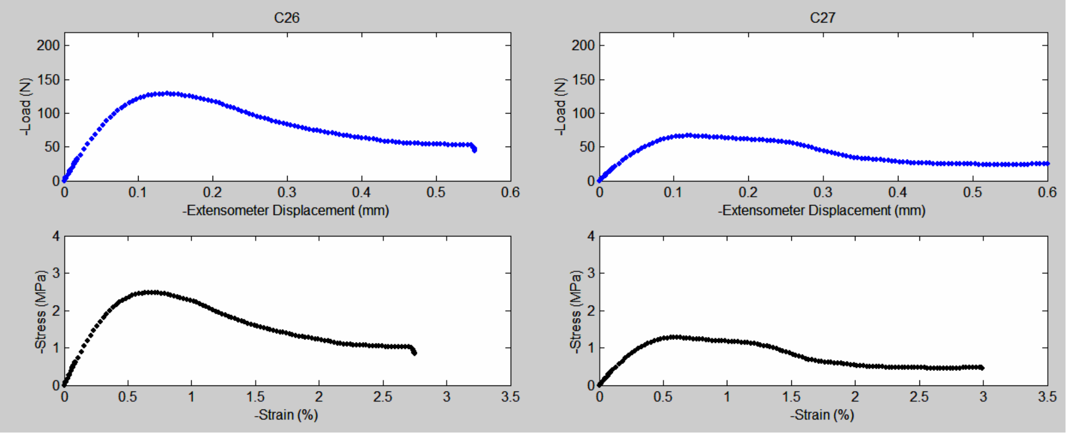
C26
C27
-Load (N)
0
50
100
150
200
0
0.1
0.2
0.3
0.4
0.5
0.6
-Extensometer Displacement (mm)
-Stress (MPa)
0
1
2
3
4
0
0.5
1
1.5
2
2.5
3
3.5
-Strain (%)

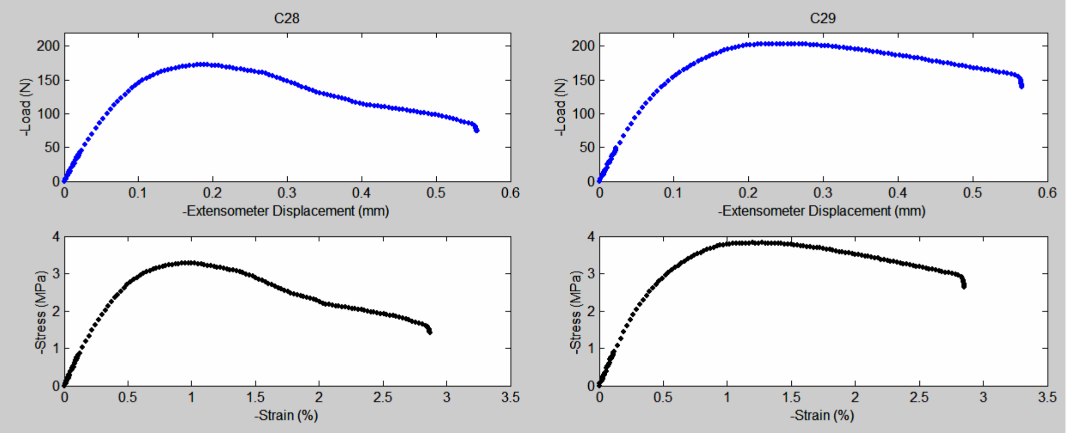
C28
C29
-Load (N)
0
50
100
150
200
0
0.1
0.2
0.3
0.4
0.5
0.6
-Extensometer Displacement (mm)
-Stress (MPa)
0
1
2
3
4
0
0.5
1
1.5
2
2.5
3
3.5
-Strain (%)

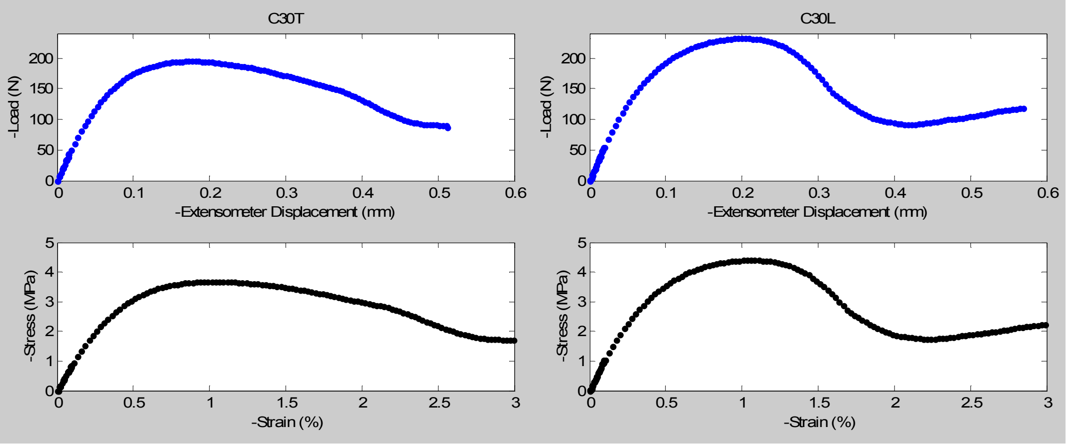
C30T
C30L
-Load (N)
0
50
100
150
200
0
0.1
0.2
0.3
0.4
0.5
0.6
-Extensometer Displacement (mm)
-Stress (MPa)
0
1
2
3
4
5
0
0.5
1
1.5
2
2.5
3
-Strain (%)

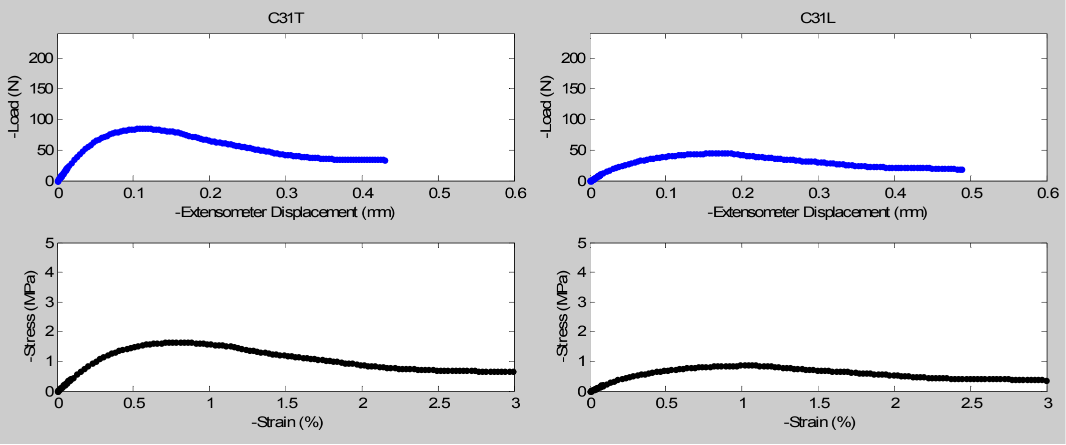
C31T
C31L
-Load (N)
0
50
100
150
200
0
0.1
0.2
0.3
0.4
0.5
0.6
-Extensometer Displacement (mm)
-Stress (MPa)
0
1
2
3
4
5
0
0.5
1
1.5
2
2.5
3
-Strain (%)

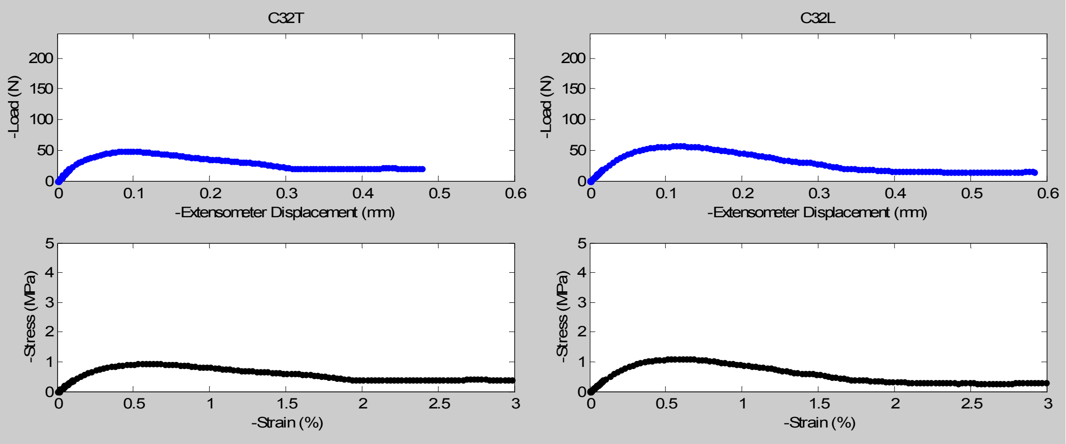
C32T
C32L
-Load (N)
0
50
100
150
200
-Extensometer Displacement (mm)
0
0.1
0.2
0.3
0.4
0.5
0.6
-Stress (MPa)
0
1
2
3
4
5
-Strain (%)
0
0.5
1
1.5
2
2.5
3

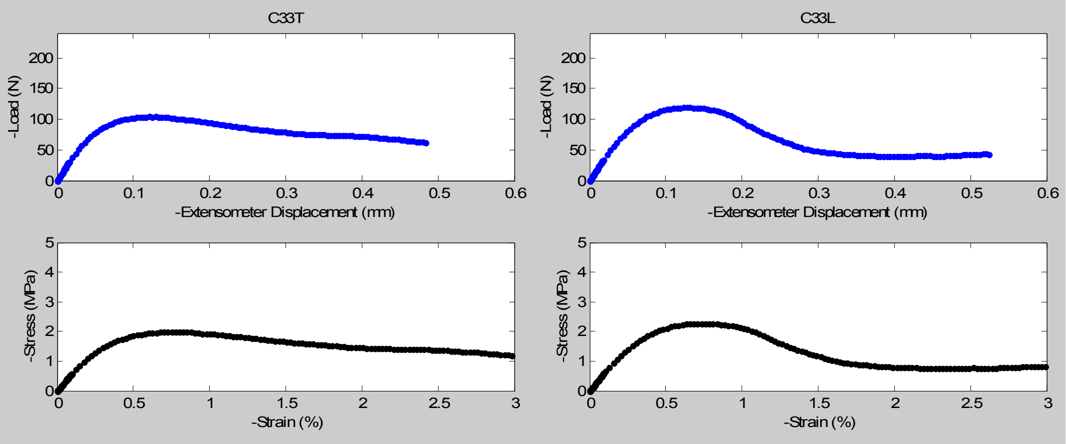
C33T
C33L
-Load (N)
0
50
100
150
200
-Extensometer Displacement (mm)
0
0.1
0.2
0.3
0.4
0.5
0.6
-Stress (MPa)
0
1
2
3
4
5
-Strain (%)
0
0.5
1
1.5
2
2.5
3

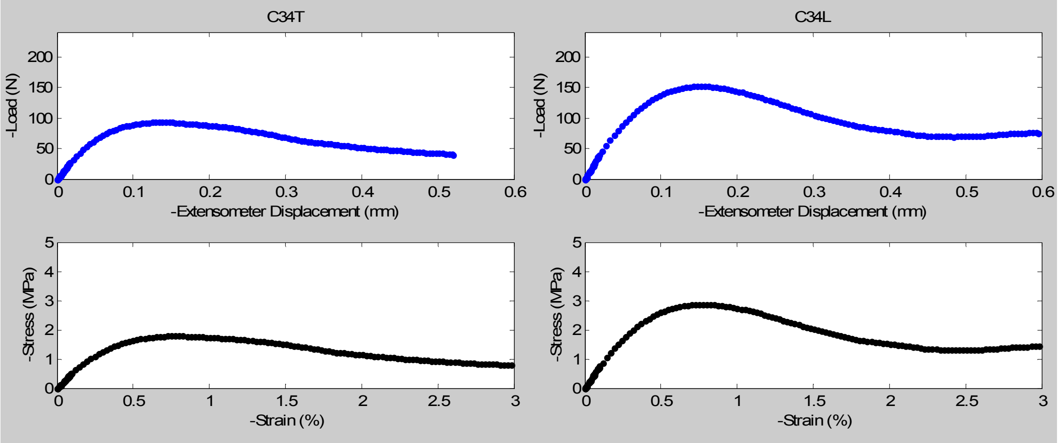
C34T
C34L
-Load (N)
0
50
100
150
200
-Extensometer Displacement (mm)
0
0.1
0.2
0.3
0.4
0.5
0.6
-Stress (MPa)
0
1
2
3
4
5
-Strain (%)
0
0.5
1
1.5
2
2.5
3

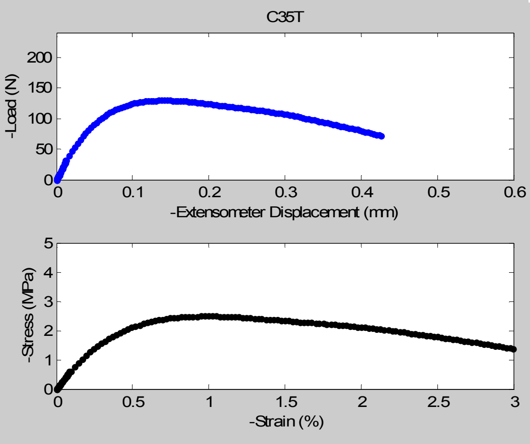
C35T
-Load (N)
0
50
100
150
200
0
0.1
0.2
0.3
0.4
0.5
0.6
-Extensometer Displacement (mm)
-Stress (MPa)
0
1
2
3
4
5
0
0.5
1
1.5
2
2.5
3
-Strain (%)

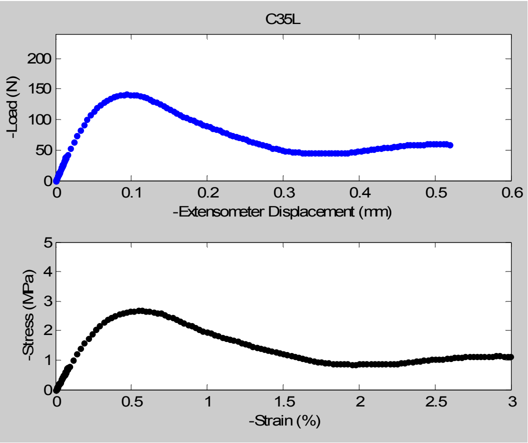
C35L
-Load (N)
0
50
100
150
200
0
0.1
0.2
0.3
0.4
0.5
0.6
-Extensometer Displacement (mm)
-Stress (MPa)
0
1
2
3
4
5
0
0.5
1
1.5
2
2.5
3
-Strain (%)

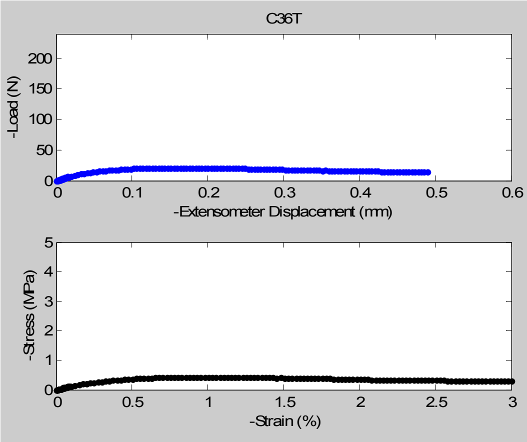
C36T
-Load (N)
0
50
100
150
200
0
0.1
0.2
0.3
0.4
0.5
0.6
-Extensometer Displacement (mm)
-Stress (MPa)
0
1
2
3
4
5
0
0.5
1
1.5
2
2.5
3
-Strain (%)

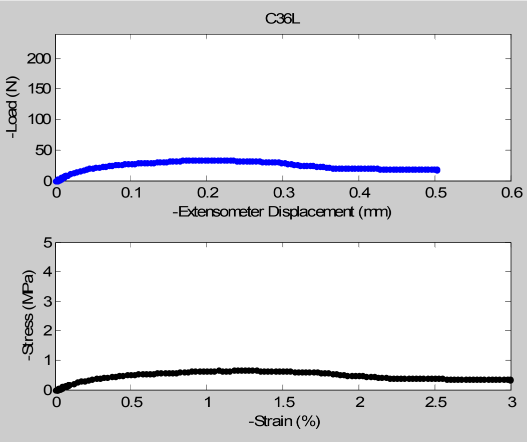
C36L
-Load (N)
0
50
100
150
200
0
0.1
0.2
0.3
0.4
0.5
0.6
-Extensometer Displacement (mm)
-Stress (MPa)
0
1
2
3
4
5
0
0.5
1
1.5
2
2.5
3
-Strain (%)

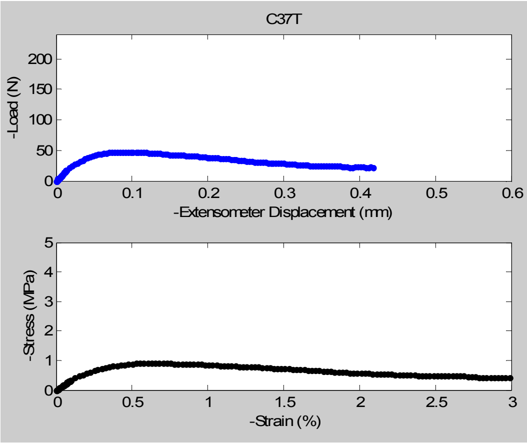
C37T
-Load (N)
0
50
100
150
200
0
0.1
0.2
0.3
0.4
0.5
0.6
-Extensometer Displacement (mm)
-Stress (MPa)
0
1
2
3
4
5
0
0.5
1
1.5
2
2.5
3
-Strain (%)

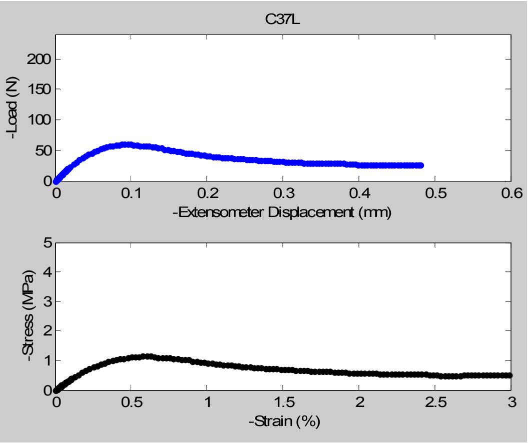
C37L
-Load (N)
0
50
100
150
200
0
0.1
0.2
0.3
0.4
0.5
0.6
-Extensometer Displacement (mm)
-Stress (MPa)
0
1
2
3
4
5
0
0.5
1
1.5
2
2.5
3
-Strain (%)